HU ISSN 2063-6792

MATERIALS SCIENCE AND ENGINEERING

A Publication of the University of Miskolc

Volume 41, Number 1

Miskolc University Press
2016

CONTENTS

Materials Science and Engineering, Volume 41, No. 1 (2016) pp. 5–12.

THE EFFECTS OF GRAIN REFINEMENT IN AL-SI ALLOYS

MÁRK ALEXA[1]–RICHÁRD TÓTH[2]–MÓNIKA TOKÁR[3]–
TAMÁS MENDE[4]

The mechanical properties of castings can be influenced by grain refinement which means the addition of a master alloy to refine the grains of the α-solid-solution. The experiments showcased in the article included the alteration of the titanium concentration of AlSi9CuFe0.5 alloy by the addition of AlTi5B1 master alloy. Thermal analysis, measurements of secondary dendrite arm spacing and grain size distribution were used to determine the effectiveness of grain refinement. The experiments demonstrated how the extent of grain refinement depends on the titanium concentration.
Keywords: aluminium alloys, grain refinement, AlTi5B1, mechanical properties

Introduction

The crystallisation of the Al-Si hypoeutectic in the casting die starts with the formation and growth of the nuclei of the aluminium solid solution. The nuclei continuously grow until reaching the eutectic temperature. The solidification ends with the crystallisation of the eutectic structure. The number and degree of fineness of the grains in the solid solution highly effect the mechanical properties: the finer the granular structure is, the better the mechanical properties are. The grain size can be decreased by accelerating the nucleation in the crystallisation process. Thus, the structure must be composed of more and smaller crystals. In order to achieve such structure, the so-called inoculation, a grain refinement is applied [1].

Apart from wrought alloys grain refinement has several benefits in cast alloys like improved mechanical properties that are uniform throughout the casting, distribution of second phase and microporosity on a fine scale, better feeding to eliminate shrinkage porosity, improved ability to achieve a uniform anodized surface, better strength and fatigue life [2, 3].

The size and distribution of grains and their secondary dendrite arm spacing (SDAS), which is highly influenced by the cooling rate, are parameters to be tightly controlled [4]. The grain size of aluminium castings is usually between 0.1 and 10 mm. Castings have fine structure if the average diameter of the grains are less than 1 mm. Due to overheating, long holding time or slow solidification rate, the structure of aluminium alloys become coarsened. In consequence, the mechanical properties are deteriorated. The aim of grain refinement is to eliminate the above-mentioned issues by adding an additive to the molten

[1] University of Miskolc, Institute of Foundry
Miskolc-Egyetemváros 3515, Hungary
alexamark@gmail.com
[2] University of Miskolc, Institute of Foundry
Miskolc-Egyetemváros 3515, Hungary
richard19930928@yahoo.com
[3] University of Miskolc, Institute of Foundry
Miskolc-Egyetemváros 3515, Hungary
monika.tokar@uni-miskolc.hu
[4] University of Miskolc, Institute of Physical Metallurgy, Metal Forming and Nanotechnology
Miskolc-Egyetemváros 3515, Hungary
tamas.mende@uni-miskolc.hu

metal to increase the amount of nuclei [5]. Elements which react with aluminium in a peritectic reaction during the solidification are the most sufficient grain refiners. Thus, titanium is one of the most commonly used grain refiner. Grain refinement should always occur after degassing and cleaning (slag removal) on 730–750 °C, depending on the composition of the alloy [5]. Figure 1 shows examples of solidifications with and without grain refinement.

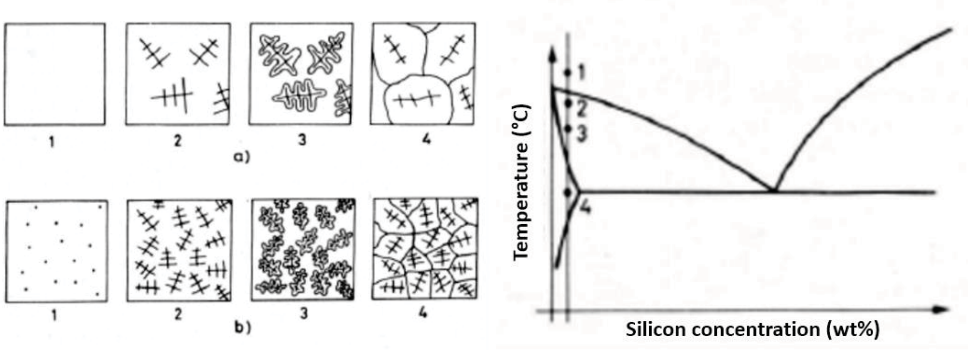

Figure 1
Solidification a) without grain refiner and b) with grain refiner [6]

1. Experimental part

A block of AlSi9CuFe0.5 low iron content alloy was examined in lab. 2819 g alloy was melted on 775±5 °C in air atmosphere in the smelting furnace shown in Figure 2.

As rotary degassing (nitrogen) treatment could not be performed under laboratory conditions, degassing pill (GASEX) was mixed with the melt. Test bars for density index test were prepared during the different stages of the experiment. The values of the density index were below the 3.3% limit value in each case.

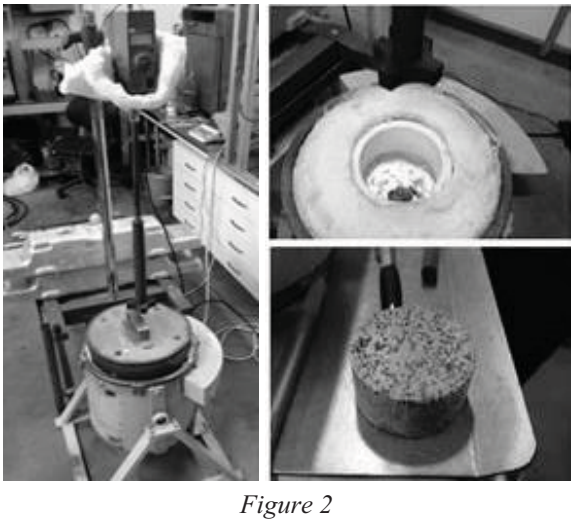

Figure 2
The smelting-holding furnace used for the experiments

AlTi5B1 master alloy was used as grain refiner. Thermal analyses and chill tests were carried out at each steps of the experiment. The experimental parameters are shown in Table 1.

Table 1
Experimental parameters

The temperature of melting and alloying	775±5°C
Casting temperature	765±5°C
Preheating temperature of the crucible	250 °C
Holding time after the addition of the master alloy	15 min

During the experiments the titanium concentration was significantly increased from 0,08–0,2 wt% Ti in three steps:

1. 0,08–0,10 Wt% Ti
2. 0,1–0,13 wt% Ti
3. 0,13–0,2 wt% Ti.

The holding time in case of each sample was 15 minutes. The titanium concentrations were chosen based on the typical titanium concentrations used in real industrial settings. The illustration of the process can be seen in Figure 3.

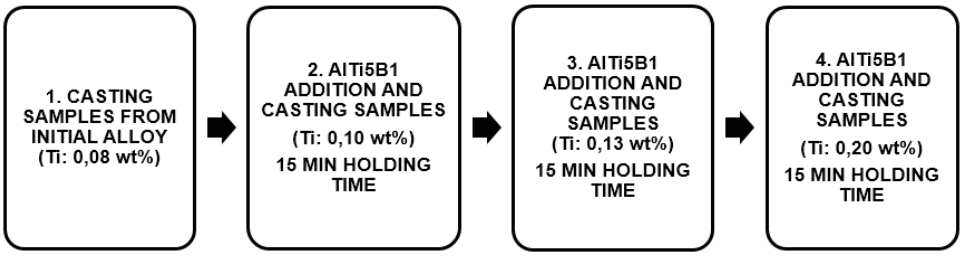

Figure 3
The steps of the experimental process

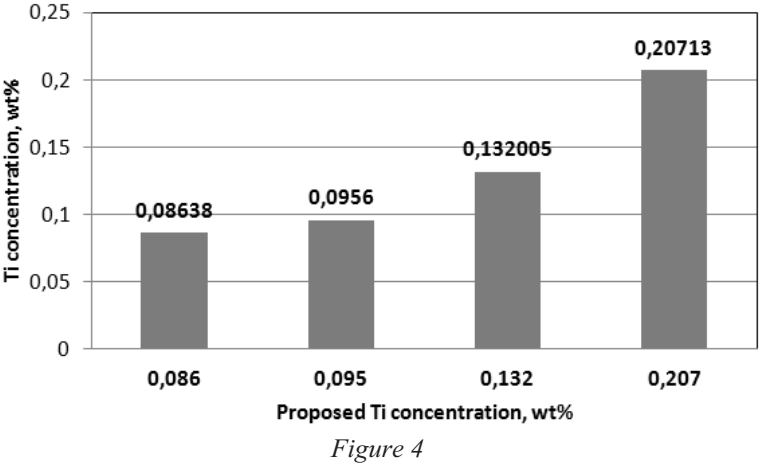

Figure 4
The titanium concentration of various alloying processes

The quantity of the melt was monitored during the experiments to be able to adjust the titanium content as precisely as possible. The mass of the test bars and the removed slag were continuously measured to monitor the decrease of the weight to calculate the quantity of the remaining melt. The various titanium concentrations after the additions can be seen in Figure 4. The detected Ti concentration was quite equal to the expected amount. Optical Emission Spectrometry (OES) technique was used to determine the chemical compositions of the alloys.

2. Results and discussion

2.1. Thermal analysis

Two methods were used to determine the extent of grain refinement from the cooling curves predefined during the thermal analysis: using the KF16 method and based on the T_{Lmax} (liquidus maximum temperature).

The determination of the KF16 value is based on liquidus temperature changes in a given time. To be more precise, the temperature difference between two points of the cooling curve is determined: T_{R1}, the temperature at 2K/s cooling speed and T2, the temperature 16 seconds later (Figure 5) [7].

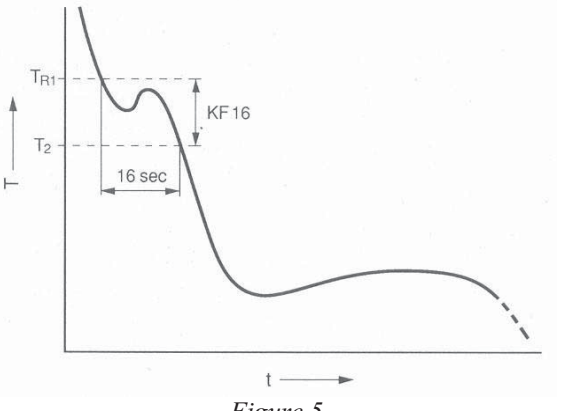

Figure 5
Evaluation based on the temperature difference of the liquidus transition [7]

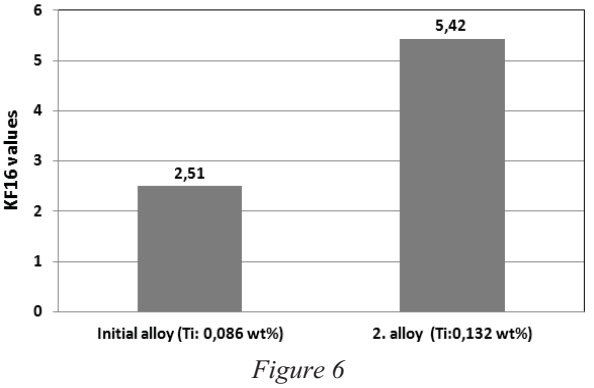

Figure 6
KF16 values

Because of some technical difficulties of the thermal analysis instrument, the KF16 values could be calculated in case of only two samples as the cooling curves could not be properly recorded during the liquidus transition in any other cases. These are shown in Figure 6.

Even though only two KF16 values could be calculated based on our cooling curves, an approximate maximum liquidus temperature could be determined. As a result, the correspondence between the titanium content various cooling curves could be observed (Figure 7). The results clearly indicate that the maximum liquidus temperature increases as the time required for nucleus development was reduced.

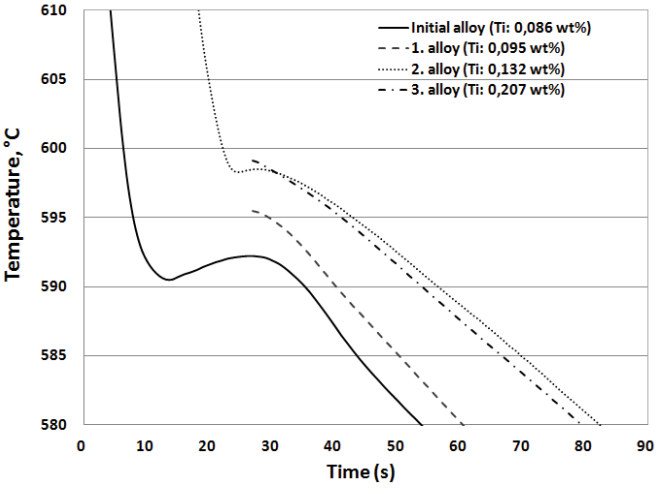

Figure 7
Cooling curves during solidification

2.2. The determination of secondary dendrite arm spacing

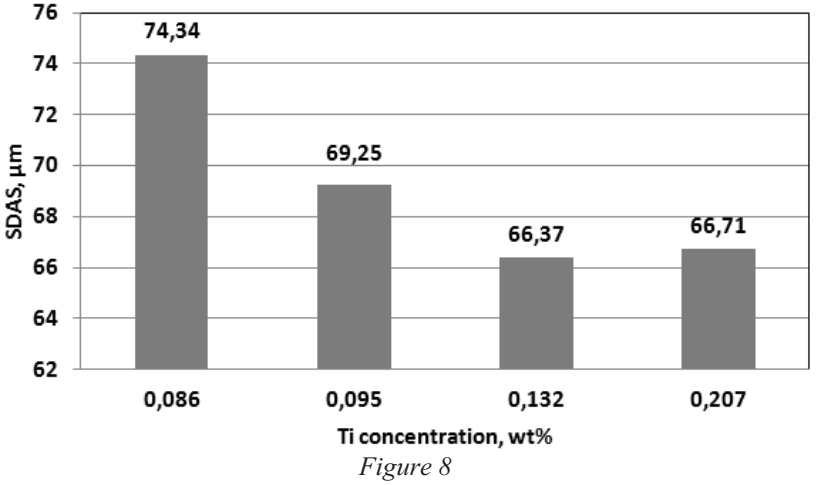

Figure 8
Secondary dendrite arm spacing values based on the titanium content

Microsections were prepared from the test bars. The test bars were etched in 0.5% HF for 15 seconds. Secondary dendrite arm spacing (SDAS) was measured with the help of an optical light microscope. Figure 8 shows the secondary dendrite arm spacing results in relation to the Ti content.

As the concentration of the Ti is increased, the secondary dendrite arm spacing values decrease by approximately 10% by volume. The increased number of the nuclei and the decreased size of the grains refines not only the primary but the secondary dendrite arms as well. However, the extent of this refinement is minor compared to grain size refinement.

2.3. The determination of the number of grains

Barker [8] etching was carried out to examine the grain structure with a Struers LectroPol-5 instrument. The parameters of the etching are summarised in Table 2.

Table 2
The parameters of the instrument used for Barker etching

Al Barker etching	
Electrolyte:	5 g tetrafluoroboric acid; 200 ml distilled water
Masking:	5 cm^2 mask
Voltage:	25 V
Flow:	20 Flow rate
Time:	60 s
Cleaning:	Distilled water→Alcohol→Drying

The samples were examined with an optical microscope (N = 25x). The approximate number of particles were determined on the surface of the samples with the help of their different colours. Five micrographs of each sample have been made and calculations carried out based on them (Figure 9).

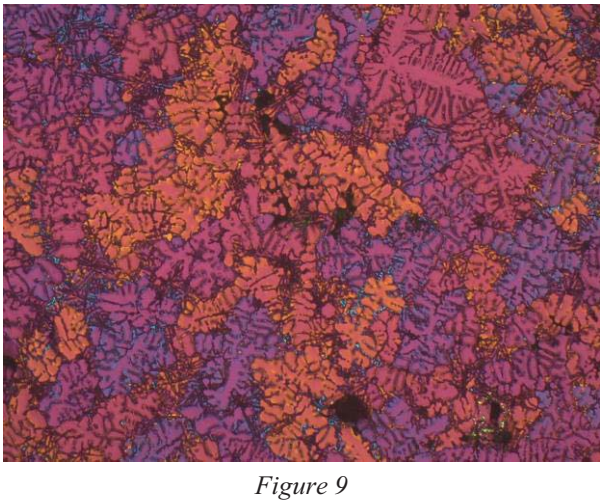

Figure 9
Optical microscope micrograph of a Barker-etched microstructure

Figure 10 illustrates that the increased Ti content resulted in higher number of particles. According to Figure 8 and 10, increasing the Ti concentration is the reason for the decrease of the secondary dendrite arm spacing and the increase of the average number of particles. The decreasing grain size, which also means an increasing number of particles, is much higher by volume than the decrease of secondary dendrite arm spacing. While the value of SDAS decreases by hardly 10%, the number of particles is 40 times higher. In case of the initial (0,086 Ti wt%) and the first two alloys (0,095 Ti wt% and 0,132 Ti wt%), the number of particles is within the range of what can be observed in test bars with similar Ti concentration under operation conditions. However, column 4 represents a significantly higher number of particles.

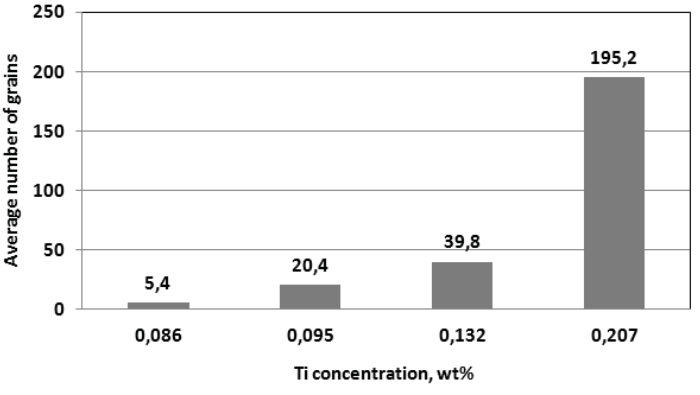

Figure 10
The average number of particles in case of different titanium contents

As Table 3 shows, the higher the titanium content was, the finer the structure became.

Table 3
The number of particles and SDAS under laboratory conditions

Samples	0,086 Ti [wt %]	0,095 Ti [wt %]	0,132 Ti [wt %]	0,207 Ti [wt %]
SDAS	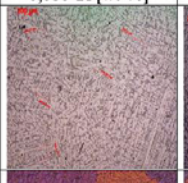	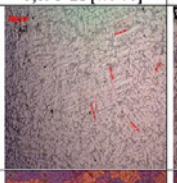	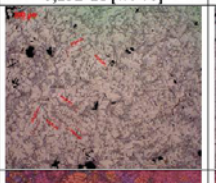	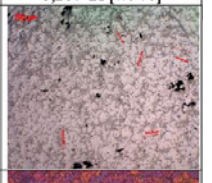
Grain refinement (Barker-etched structure)			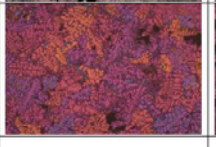	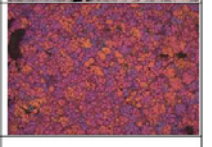
Average number of grains	5,40	20,40	39,80	195,20
SDAS [µm]	74,34	69,25	66,37	66,71
KF 16	2,51	-	-	5,42
Casting temperature (°C)	720	673	615	715
Volume of samples [g]	94,00	98,00	94,00	100,00

As it can be observed in Table 3, the temperature of the melt was different during each castings. The reason for this phenomena is the malfunction of the holding furnace.

Conclusion

The KF16 values of the base alloy and the alloy with 0.132 wt% Ti content seem to have an increasing tendency during the experiments. However, further investigation is required in case of these values.

As the increase in the maximum liquidus temperature can be observed depending on the concentration of the titanium during the thermal analysis, the fact that crystallisation can start at lower temperature when the Ti concentration is increased.

A direct correlation can be observed between the maximum liquidus temperature and the titanium concentration, as the maximum of the liquidus rises parallel with the increasing titanium concentration. Thus, the degree of supercooling for the crystallisation process to start is decreased.

The secondary dendrite arm spacing and the grain size correlate, as the smaller secondary dendrite arm spacing results in higher number of particles, thus, the grain size is decreased.

Increasing the titanium content resulted in achieving appropriate mechanical properties due to the fine grained structure of the casting.

Acknowledgement

The authors are grateful to Mária Ambrus for her advice.

References

[1] QUESTED, T. E: Understanding mechanisms of grain refinement of aluminium alloys by inoculation. *Materials and Science technology,* 20 (2004), 1357–1369.

[2] APELIAN, D.–SIGWORTH, G. K.–WHALER, K. R.: Assessment of grain refinement and modification of Al-Si foundry alloys by thermal analysis. *AFS Trans,* 92 (1984), 297–307.

[3] KASHYAP, K. T.–CHANDRASHEKAR, T: Effects and mehcanisms of grain refinement in aluminium alloys. *Bull. Mater. Sci.,* Vol. 24, No. 4, August 2001, 345–353.

[4] IBARRA, D. G.: *Control of Grain Refinement of Al-Si Alloys by Thermal Analysis.* National Library of Canada, 1999.

[5] JÓNÁS P.: *Könnyűfém öntészeti ismeretek.* Nemzeti Tankönyvkiadó, Budapest, 2011.

[6] BAKÓ K.–SÁNDOR J.–SZABÓ Zs.–SZIJ Z.: *Öntvények gyártástechnológiája.* Műszaki Könyvkiadó, Budapest, 1986.

[7] MENK, W.–SPEIDEL, M. O.–DÖPP, R.: Die thermische Analyse in der Praxis der Aluminiumgießerei. *Giesserei,* Bd. 79, Heft 4 (1992), 125–134.

[8] Centre technique des industries de la fonderie (France): *Metallographic atlas of cast aluminium alloys.* Éditions Techniques des Industries de la Fondrie, (1) 45.34.27.54, 1989.

Materials Science and Engineering, Volume 41, No. 1 (2016), pp. 13–22.

THE EXAMINATION OF THE EFFECTS OF STRONTIUM CONTENT

VIKTÓRIA BOROS[1]–GYÖRGY FEGYVERNEKI–JENŐ DÚL[2]–MÓNIKA TOKÁR[3]

During the experiments AlSi8Cu3 alloy was alloyed with strontium in different concentrations. The effect of strontium on the silicon in the eutectic structure was examined under operating conditions, in case of both higher (> 100 ppm) amount of strontium content than usual in operating conditions and lower (~100 ppm) amount of strontium content, which is not used in practice.
The extent of modification in the test bars casted with thermal analysis and on the final castings was determined with the help of cooling curves and by comparing them to images of reference standards. The reason of using these two methods was to determine the correlation between the levels of modifications determined by the temperature of supercooling, which can be calculated from the cooling curves, and the structure evaluation methods. The mechanical properties of castings which were casted in the given cooling conditions were also examined.
Keywords: aluminium alloys, modification, strontium, thermal analysis

Introduction

Al-Si based alloys are the most commonly used alloys in aluminium light metal foundries, especially in the automobile industry. Depending on the utilisation, the requirements are becoming stricter which are stating that the mechanical properties and the ductility should be around the same value within the casting. The structure of these alloys is influenced by a number of factors, such as the degree of the modification of the silicone in the eutectic structure, the dendrite arm spacing, the porosity and the intermetallic compounds. The mechanical properties can be improved by the optimisation of these parameters [1].

The aim of the modification of the melts of Al-Si alloys is to refine the silicon of the eutectic structure with the addition of a master alloy. Thus, the formation of coarse silicon crystals can be prevented. Sodium, strontium and sodium are the most common elements for the modification of silicon in the eutectic structure.

Aladár PACZ introduced the treatment of Al-Si melts using sodium in 1921 which became the standard modification method of the eutectic structure of Al-Si alloys [2, 3]. After the declaration of the patent, the tests to inquire information on the effects of the various elements on the morphology of the silicon precipitating from the eutectic structure of the aluminium-silicon alloy during the crystallisation. It has been proved that the favourable morphology of the precipitating silicon can be facilitated with not only sodium

[1] University of Miskolc, Institute of Foundry
Miskolc-Egyetemváros 3515, Hungary
borosviktoria1@gmail.com
[2] University of Miskolc, Institute of Foundry
Miskolc-Egyetemváros 3515, Hungary
[3] University of Miskolc, Institute of Foundry
Miskolc-Egyetemváros 3515, Hungary
monika.tokar@uni-miskolc.hu

but strontium as well, during a significantly longer time interval (more time for decay). Strontium decreases the diffusion rate of the silicon during the crystallisation of the eutectic structure. Al-Si alloys with hypo- and eutectic structures decrease the eutectic temperature of Al-Si alloy during crystallisation.

Beside strontium, antimony is also used as an inoculant but not as often because of its tendency to create toxic hybrids, it segregates in the secondary alloys during reprocessing and reacts with other elements to create intermetallic compounds.

The morphology of the eutectic silicon is lamellar in the non-modified and spheroidal in the modified Al-Si alloys. If lamellar silicon is precipitated during the crystallisation of the alloy, contraction cavities might develop due to the coagulation of the lamellar silicon. In order to assure the appropriate mechanical properties, the silicon of the eutectic structure should not be lamellar. In case of the modified eutectic structure, the silicon in the structure becomes fine and spheroidal, increasing the tensile strength, elongation and formability. Another parameter influencing the fineness of silicon grains is the cooling rate. However, fully modified structure can only be achieved by increasing the cooling rate and adding further inoculants. The appropriate amount of these so-called inoculants are added to the proper alloys in order to modify the structure [4].

Figure 1 illustrates the morphology of the lamellar non-modified and modified fine-grained Si.

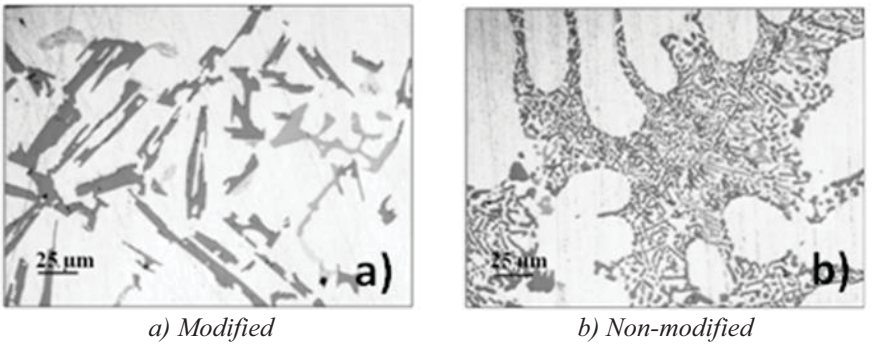

a) Modified *b) Non-modified*

Figure 1
The morphology of the silicon precipitated during the crystallisation of the eutectic structure of the Al-Si alloy [5]

1. Experiments

High purity AlSi8Cu3 (DIN 226.10) alloy was examined during the experiments; the results of the chemical analysis can be seen in Table 1. AlSr10 (pure aluminium wire with 10 wt% Sr) master alloy was used to change the strontium concentration of the melt.

Table 1
The chemical composition of the experimental AlSi8Cu3

Element	Si	Cu	Mg	Ti	Sb	Fe	Mn	Pb	Sn	Ni	Zn
wt %	9.06	2.45	0.31	0.11	0.0011	0.49	0.45	0.03	0.0009	0.03	0.54

The experiments were carried out under operating conditions following the technological steps seen on Figure 2. First, the melt is poured from the smelting furnace into a ladle and then into a holding furnace. Approximately 200 kg melt can be found in the holding furnace ("residue melt") on which the new melt is poured. The next step is the addition of the master alloy (AlSr10), the amount of which is determined by a previous analysis of the composition to achieve the required strontium concentration. In order to increase the purity of the metal and support the homogeneous distribution of strontium, nitrogen degassing treatment was performed during strontium addition and the nitrogen degassing treatment of the melt is performed at the same time. Test bars were casted after the degassing treatment.

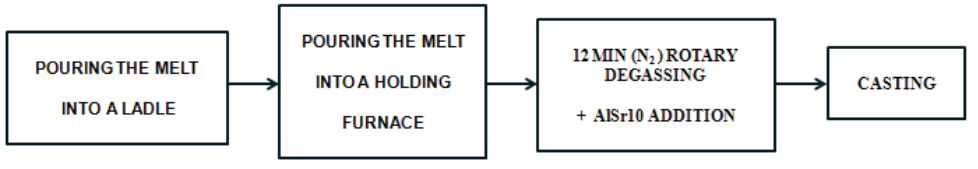

Figure 2
The technology of the operation process

The strontium concentration of the base melt was changed, as well as strontium master alloy was added during the rotary degassing treatment (Table 2). Table 2 contains information on the strontium concentration of the base melt and the strontium concentration modified during the degassing treatment.

Table 2
The values of the strontium concentration of the base melt and after the degassing treatment

Alloys	Sr concentration of the base melt	Sr concentration with AlSr10 master alloy addition during the rotary degassing treatment
Increased Sr concentration	168 ppm	40 ppm
Decreased Sr concentration	90 ppm	–
	106 ppm	–

Chill tests were carried out at each steps of the experiment in order to monitor the strontium concentration, along with thermal analyses and density index measurements.
The parameters of the experiments are summarised in Table 3.

Table 3
Experimental parameters

The temperature of melting	775±5°C
Casting and alloying temperature	755±5°C
The temperature of the crucible for thermal analysis and density index measurements	200±5°C

2. Results and discussion

2.1. Modification level of the eutectic structure

Reference standard images of the American Foundry Society

Based on the table qualifying the silicon modification of Al-Si alloys prepared by the American Foundry Society (AFS), which can be seen in Figure 3, the degree of modification can be easily determined by a simple comparison [6].

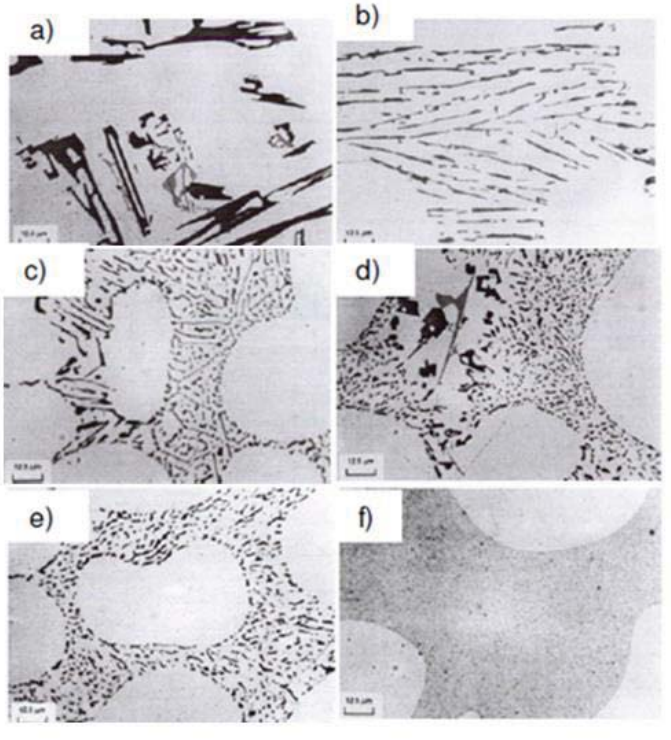

Figure 3
AFS table (A356-AlSi7Mg)
a) non-modified; b) lamellar, c) partly modified; d) non- lamellar; e) modified; f) over-modified [6]

After preparing microstructures from the test bars, 15 photos were taken of the non-etched microsections with 500x magnification using a Zeiss optical light microscope. These were compared to the images from the rating table of the AFS. The degree of modification was determined based on the examined images. Based on the average of the 15 degrees of modification of the images, the degree of modification of the test bars with the given strontium concentration could be obtained.

The degrees of modification and the strontium concentrations at each step of the experiments are shown in Table 4.

Table 4
The degrees of modification and the strontium concentrations

Alloying		After melting	Before degassing	After degassing	After casting – residue melt
Sr 168+40 ppm (*Increased Sr concentration*)	Degree of modification	Partly modified	Non-lamellar	Non-lamellar	Non-lamellar
	Sr (ppm)	106	108	107	106
Sr 94 ppm (*Decreased Sr concentration*)	Degree of modification	Lamellar	–	Partly modified	Non-lamellar
	Sr (ppm)	94	–	92	124
Sr 106 ppm (*Decreased Sr concentration*)	Degree of modification	Partly modified	Lamellar	Lamellar	Partly modified
	Sr (ppm)	168	183	202	202

If the strontium concentration decreased below 100 ppm, the originally lamellar structure became non-lamellar by the end of the experiments. Thus, a degree close to modification can be achieved, while the alloy with 106 ppm strontium content is already partly modified in the beginning of the process. This becomes non- lamellar by the end of the process. As the alloy with 168+40 ppm Sr content is lamellar both before and after the degassing treatment, this degree is not acceptable. By the end of the process, the degree becomes partly modified. When there is no extra strontium addition, a consistent lamellar structure is formed.

Thermal analysis

The cooling curves were determined with an MK type data collector. All the data were collected in a table in order to define the cooling curves depending on temperature and time.

The degree of modification is usually calculated based on the following relation from the ΔT supercooling value of the cooling curves [7]:

$$\Delta T_{E,G}^{Al-Si} = T_{E,G,non\ modified}^{Al-Si} - T_{E,G,modified}^{Al-Si} \tag{1}$$

where:

$\mathbf{T^{Al\text{-}Si}_{E,G,NON\text{-}MODIFIED}}$ – solidification temperature of the non-modified eutectic structure

$\mathbf{T^{Al\text{-}Si}_{E,G,MODIFIED}}$ – solidification temperature of the modified eutectic structure

$\mathbf{\Delta T^{Al\text{-}Si}_{E,G}}$ – degree of supercooling

The maximum value of the solidification temperature of the eutectic structure was determined in case of both non-modified ($T_{E,G}^{Al\text{-}Si}{}_{NON\text{-}MODIFIED}$) and modified ($T_{E,G}^{Al\text{-}Si}{}_{MODIFIED}$) AlSi8Cu3 alloys. The degree of supercooling was calculated from two temperatures ($\Delta T_{E,G}^{Al\text{-}Si}$) based on equation (1). The maximum value of the solidification temperature of the eutectic structure of the non-modified alloy with 5 ppm strontium content, casted under laboratory conditions, was used to calculate the value of the

supercooling (ΔT). The values of supercooling are calculated via equation (1) and illustrated in Figure 4. The various time intervals are also indicated at each data points.

Based on literature, the structure of eutectic silicon is considered non-modified when ΔT is below 9 °C and modified if the value is higher than that [7].

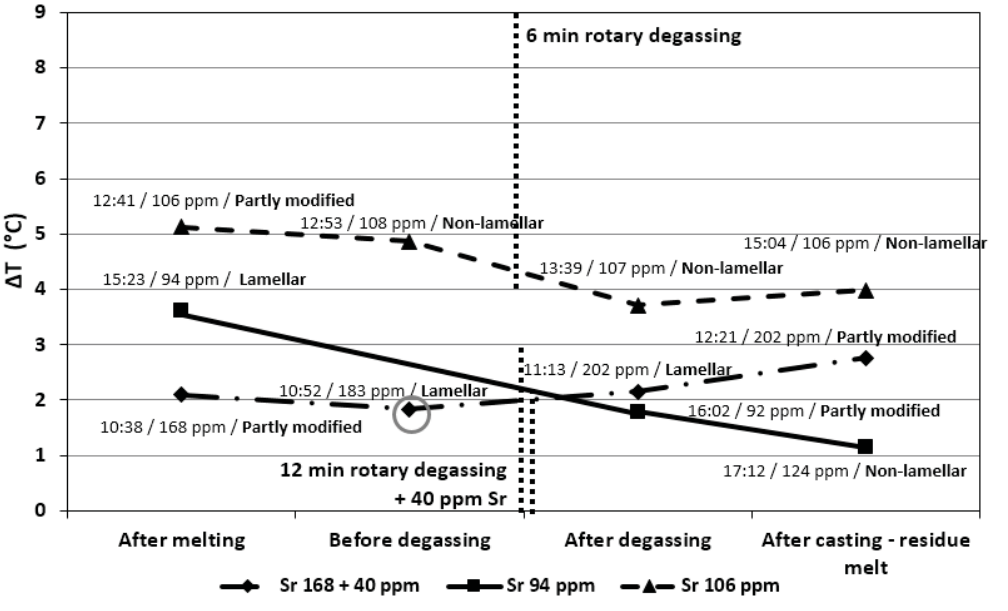

Figure 4
The ∆T supercooling values calculated from equation (1) with the strontium concentrations and degrees of modification

The results showed that the strontium concentration became higher in case of the alloy with 168 + 40 ppm strontium content before degassing treatment without strontium addition because of the 200 kg melt in the holding furnace, the strontium content of which is not determined. The strontium concentration of the melt before degassing and after pouring into the holding furnace was 183 ppm. Just like under operating conditions, 40 ppm strontium was added to the melt with 183 ppm strontium concentration. This only partly dissolved in the system as the strontium concentration was only 202 ppm after degassing. After degassing, the silicon of the eutectic structure is lamellar, so the effect of the added 40 ppm of strontium cannot be observed immediately. However, the supercooling value increases as time passes which means that the effect of strontium is delayed.

In case of melts with lower strontium content (94 ppm, 106 ppm), the supercooling temperature gradually decreases during the different experimental steps. Based on the supercooling values, the effect of the strontium in the melt cannot be observed.

Optical microscopic images of microsections used for thermal analyses, the degrees of modifications determined based on the images and the respective strontium concentrations are illustrated in Figure 5.

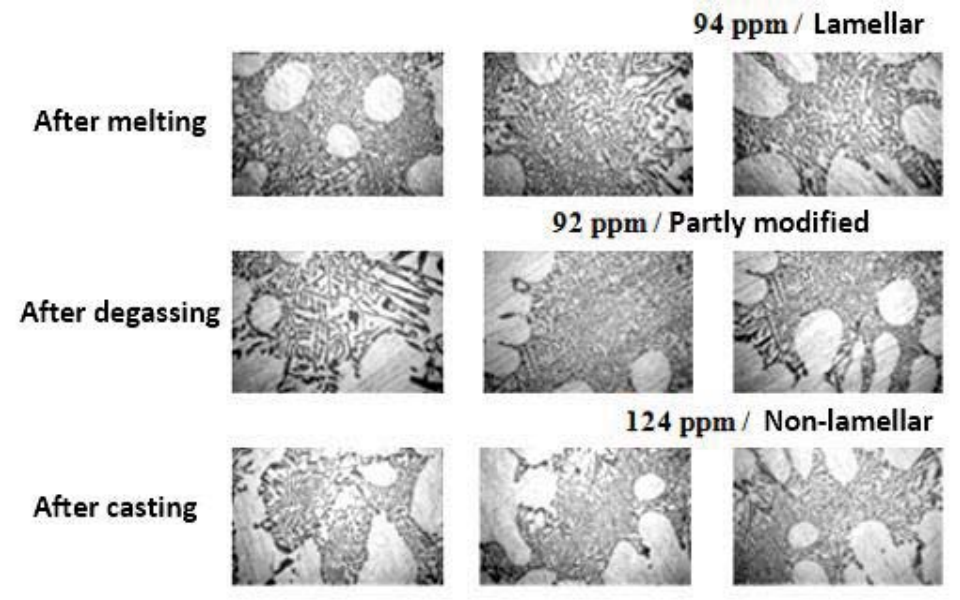
94 ppm / Lamellar
After melting
92 ppm / Partly modified
After degassing
124 ppm / Non-lamellar
After casting

a)

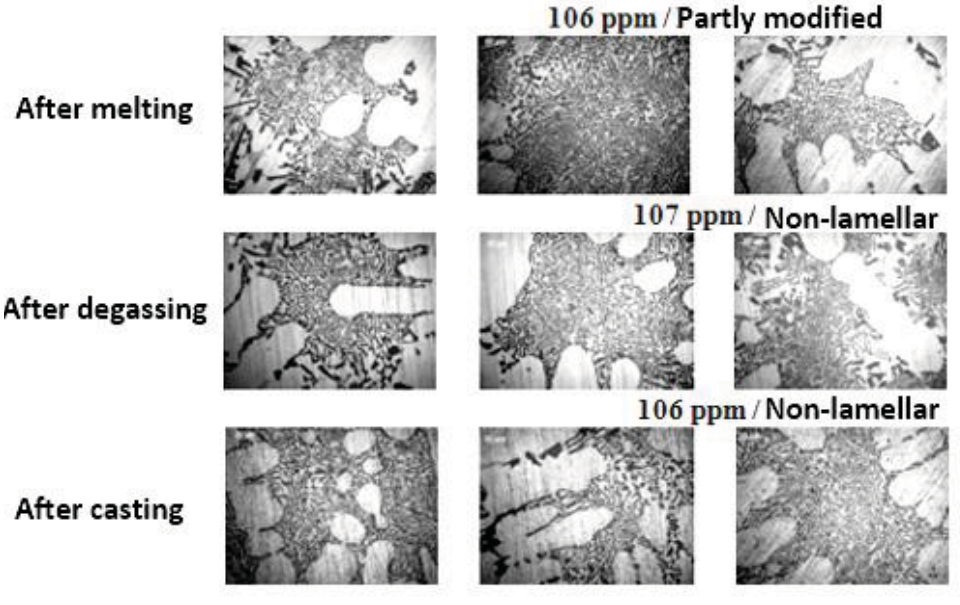
106 ppm / Partly modified
After melting
107 ppm / Non-lamellar
After degassing
106 ppm / Non-lamellar
After casting

b)

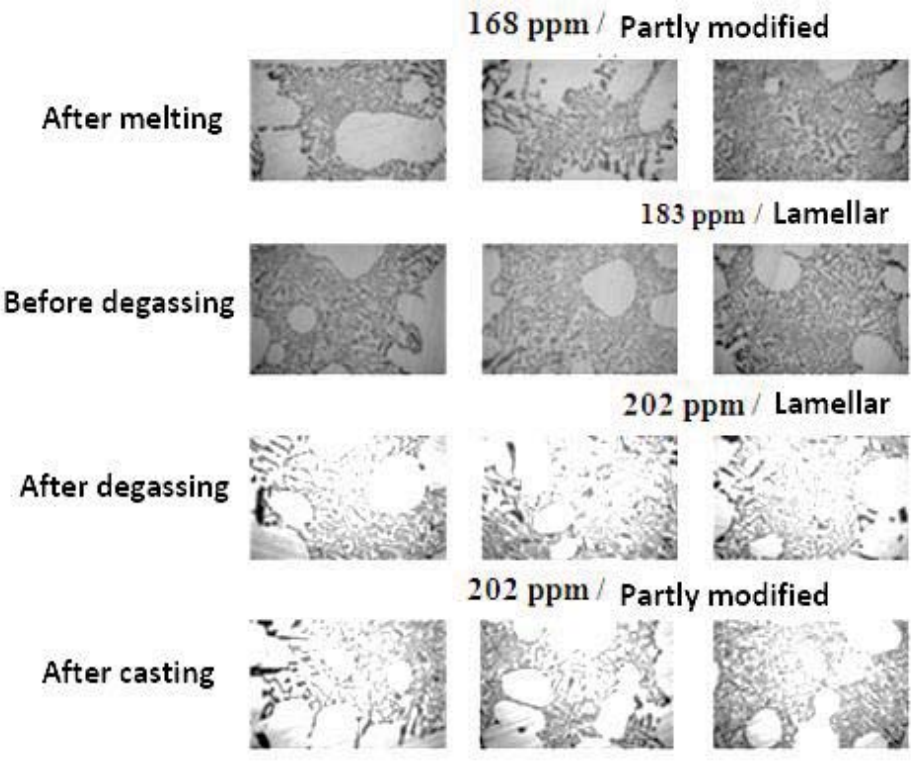

c)

Figure 5

The degrees of modifications determined with the help of standard images with respect to the Sr concentrations during the different technological steps

a) Sr 94 ppm; b) Sr 106 ppm; c) Sr 168 + 40 ppm

2.2. Mechanical properties

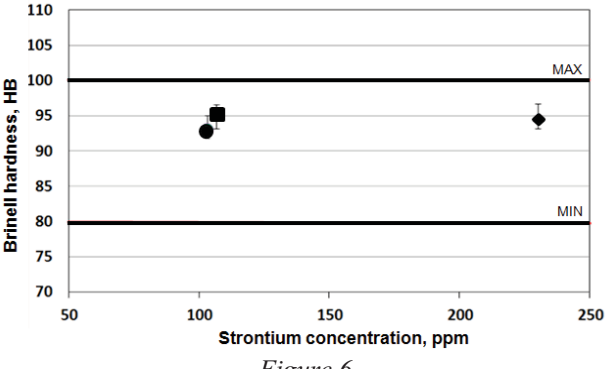

Figure 6

Correlation between the average Brinell hardness and the average strontium concentration

The examination of the mechanical properties of the castings prepared in the pre-defined cooling conditions was carried out.

Brinell hardness was measured using a Ø5 mm ball with 250 kp force applied. In Figure 6, the average of three measurements in case of all castings are illustrated, based on the strontium concentration.

As it can be observed in Figure 5, the values of Brinell hardness are between 80 and 100 HB, as it was expected.

The elongation and tensile strength values were also examined. 9 tensile test specimens were made out of five castings in case of each experiments, and the values are averaged.

Figures 7–8 show the average elongation (A) and tensile strength (R_m) values.

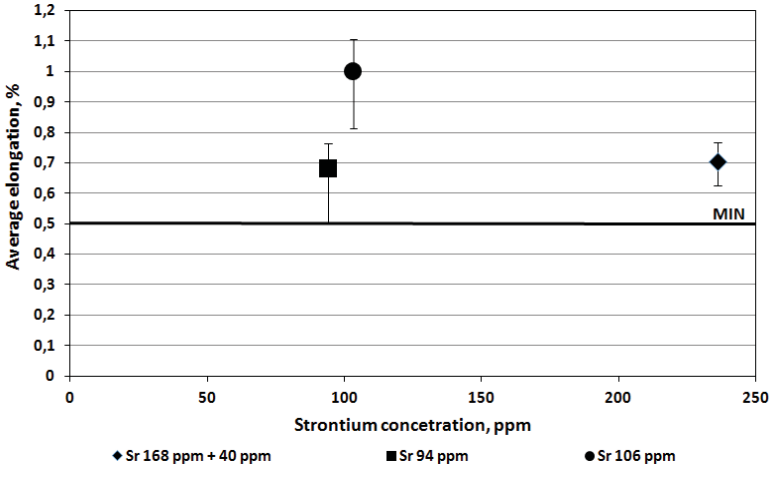

Figure 7
Correlation between average elongation and average strontium concentration

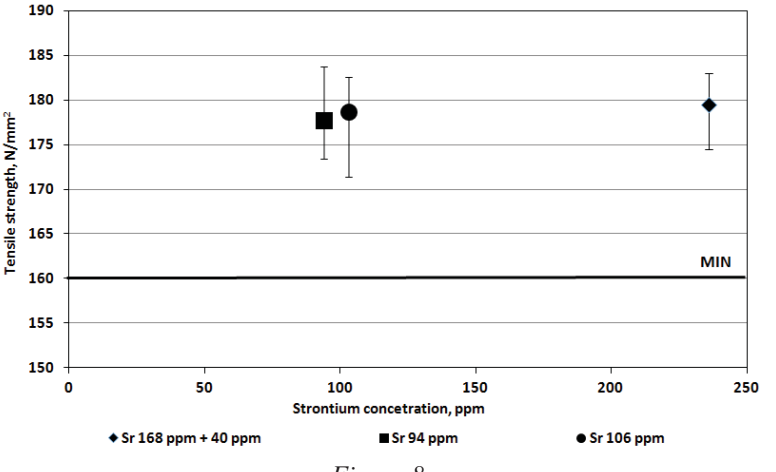

Figure 8
Correlation between average tensile strength and average strontium concentration

The highest value of elongation can be achieved if the strontium concentration is below 100 ppm. The same is true in case of the average yield limit but in case of the tests with 168 + 40 ppm and 106 ppm strontium concentrations, the values are above the minimum. There is no significant difference between the tensile strength values and those are always above the given minimum values.

Conclusion

The effects of variable strontium concentration was analysed in case of AlSi8Cu3 alloy. The examination of the structure determined that optimal modification levels can be achieved in every case examined.

Based on the examination of the mechanical properties, the required mechanical properties can be achieved via all the experiments included in this article despite the difference in certain parameters.

According to the results, starting out with low (~100 ppm) strontium concentration, based on the parameters of the actual experiment, is favourable.

Acknowledgement

The authors are grateful to Mária Ambrus for her advice.

References

[1] Li, L: *Paramétres métallurgiques contrólant l'évultaion microsturcturale dans les allieges de fonderie Al-Si-Mg et Al-Si Cu.* PhD Thesis. Université du Québec, 2004.
[2] Pacz, A.: *US Patent.* No. 1387900, 1921.
[3] Furlan, T. S.–Fuoco, R: Optimization of the Sr addition in permanent mold A356 alloys. *AFS Transactions*, Schaumburg, 2, 2008, 08–142.
[4] Nafisi, S.–Ghomashchi, R: Effects of modification during conventional and semi-solid metal processing of A356 Al-Si alloy. *Materials Science and Engineering A,* 415, 2006, 273–285.
[5] Tokár M.: *Az antimon és stroncium együttes módosító hatásának vizsgálata AlSi9Cu3 öntészeti ötvözet esetén, IV.* Kutatószemináriumi dolgozat. 2013.
[6] Asensio-Lozano, J.–Suarez-Pena, B: Effect of the addition and/or modifiers on the microstructure of die cast Al-12Si alloys. *Scripta Materialia*, 2006, 943–947.
[7] Djurdjevic, M.–Jiang, H.–Sokolowski, J.: On-line prediction of aluminum-silicon eutectic modification level using thermal analysis. *Materials Characterization,* 46, 2001, 31–38.

Materials Science and Engineering, Volume 41, No. 1 (2016) pp. 23–31.

THE EFFECT OF POWER SUPPLY RIPPLE ON DC WATER ELECTROLYSIS EFFICIENCY

ZSOLT DOBÓ[1]–ÁRPÁD BENCE PALOTÁS[2]–PÁL TÓTH[3]

It has been known that the efficiency of alkaline water electrolysis under DC conditions is dependent on the stability of the power supply. High output voltage fluctuation is typical mostly at thyristor-based power supplies - this effect is known as power supply ripple. As a result of continuously varying voltage levels the behaviour of the electrolysis may differ from DC conditions. The deviation from DC signals may lead to decreased cell efficiency – the magnitude of this effect was investigated in this paper. A novel experimental method was designed in order to obtain a complete experimental matrix. The experimental method was based on a fully automatic, programmable power supply and measurement system. The system was capable of carrying out thousands of measurements in a day without human supervision. Cell efficiency was recorded as a function of signal amplitude and frequency, while signal offset (the DC component) was kept at a constant 2.44 V. A total of 245 measurements were carried out that investigated an experimental matrix between 0.2 and 5 kHz frequency and between 0 and 443 mV amplitude. It was shown that cell efficiency was not significantly affected by signal frequency, while a significant efficiency loss (up to 4%) was measured as the amplitude of signal variation increased.

Keywords: water electrolysis, voltage fluctuation, cell efficiency

Introduction

Hydrogen is mostly produced from fossil resources, primarily from methane (natural gas) [1] due to cost-efficiency reasons. However, growing concerns about diminishing fossil fuel reserves and increasing gas prices drive attention to hydrogen production from water. The conventional electrolytic method for hydrogen production is alkaline water electrolysis. Net efficiency of 50 to 60% is common with current electrolytic hydrogen production methods [1, 2, 3], however the overall efficiency is much lower if the losses of electricity generation from primer or renewable fuels is also taken into consideration. In this case the overall efficiency rate would hardly reach 40% [4]. Because of the low overall efficiency, attention turned to enhancing the electrolytic process; i.e. by subjecting the cell to a gravity field [5], ultrasonic waves [6] or magnetic fields [7].

The conventional DC electrolysis of water involves generation of hydrogen gas at the cathode and oxygen gas at the anode. The electrode reactions are typically described as follows [8]:

$$\begin{aligned} \text{cathode:} \quad & 2H_2O + 2e^- \rightarrow H_2 + 2OH^- \\ & 2H^+ + 2e^- \rightarrow H_2 \\ \text{anode:} \quad & 2OH^- \rightarrow 0.5O_2 + H_2O + 2e^- \\ & H_2O \rightarrow 0.5O_2 + 2e^- + 2H^+ \end{aligned}$$

[1] University of Miskolc, Department of Combustion Technology and Thermal Energy
3515 Miskolc-Egyetemváros, Hungary
zsoltdobo@gmail.com

[2] University of Miskolc, Department of Combustion Technology and Thermal Energy
3515 Miskolc-Egyetemváros, Hungary
arpad.palotas@uni-miskolc.hu

[3] University of Miskolc, Department of Combustion Technology and Thermal Energy
3515 Miskolc-Egyetemváros, Hungary
toth.pal@uni-miskolc.hu

Gas formation can be induced by applying a potential difference between the cell electrodes. In theory, the thermodynamic decomposition voltage of water at 298 K and 1 atm is 1.23 V, however, due to reaction overpotentials and resistance losses (ohmic voltage drop), higher cell voltages should be applied [8]. Gas starts to form at a voltage level of 1.65–1.7 V and most industrial cells are operated from 1.8 to 2.6 V [4, 9].

In order to create a potential difference between the electrodes AC/DC or DC/DC power supplies are typically used. One of the main properties of power supplies is voltage ripple, meaning that the voltage level is not constant, but oscillates around a mean value. Reduced or eliminated voltage ripple is an important requirement, although it is difficult to achieve with high-power sources. In water electrolysis any deviation from perfectly uniform DC voltage might affect the electric power consumption, the intensity of gas production and the water splitting efficiency. Although several papers reported using impulse voltage or interrupted direct current [10–13], the available information about the effects of the applied voltage waveforms is still scarce [14, 15]. It has been suggested that efficiency loss may occur if the power supply used for DC electrolysis produces contaminated or unstable signals [16], but the magnitude of this effect has not been investigated so far. Since the feasibility of alkaline DC water electrolysis depends strongly on the achievable cell efficiency, the information regarding the effect of signal stability on efficiency may be valuable from economic points of view. In this paper, we investigate the effect of power supply ripple on cell efficiency. A novel experimental system was designed and built that allowed for the quick and automatic assessment of different signal waveforms that modelled the ripple of DC power supplies.

1. Materials and methods

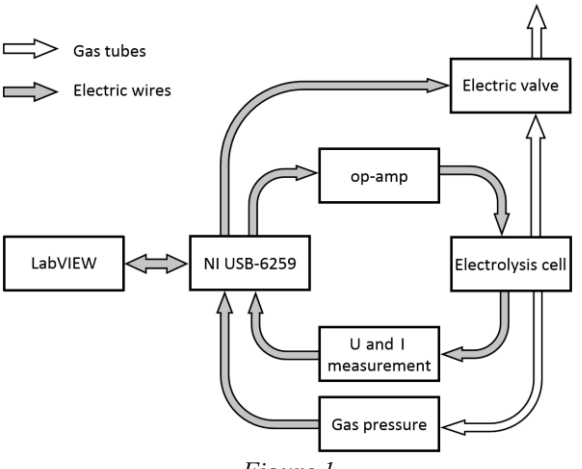

Figure 1
Schematic illustration of the experimental system

A schematic illustration of the measurement system is seen in Figure 1. The main component is the gas-tight cell powered by a special power supply containing a high current operational amplifier (op-amp) type OPA549 [17]. The op-amp is controlled by a dedicated National Instruments device (NI USB-6259) – its operation can be automated using a LabVIEW program. The device is responsible for measuring cell voltage, cell current and the pressure of the generated gas. The NI device can also control the electric valve connected to the top

of cell. This system can generate arbitrary waveforms with frequencies up to 50 kHz, currents up to 8 A and between voltages of −10 and 10 V. The power supply can be operated either in galvanostatic or potentiostatic mode, i.e., it is able to generate voltage or current waveforms, according to the operational amplifier topology [17].

The power supply is connected to the electrolytic cell shown in Figure 2. The cell is a gas-tight vessel with two electrodes attached to the lid. Next to the electrodes are the two gas outlets, a T-type Thermocouple (used as a sensor to measure electrolyte temperature) and the outlet pipes of the cooling cycle (mounted on the lid). Two 1.5 mm thick stainless steel electrodes (material: EN 1.4307) were placed in the cell, with a spacing of 40 mm. 500 ml of 30 wt% potassium hydroxide aqueous solution was used as the electrolyte. The temperature of the electrolyte was 25±0.5 °C.

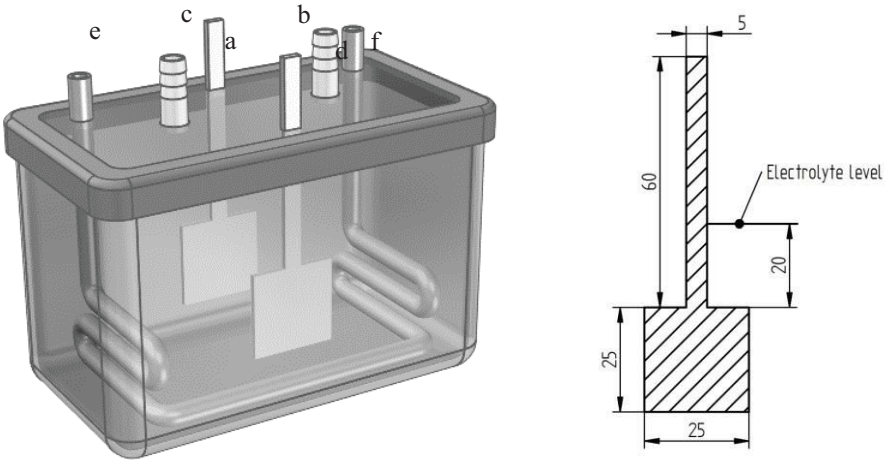

Figure 2
Left: Schematic illustration of the electrolytic cell, a) cathode, b) anode, c) to pressure sensor, d) to valve, e) cooling water inlet, f) cooling water outlet
Right: electrode dimensions and their position in the electrolyte (the units are in mm)

The gas bubbles formed at the electrode surfaces cause pressure increase in the cell. The rate of pressure increase is directly proportional to the flow rate of the gas produced. Pressure was measured using a pressure sensor type MPX5010DP (Freescale Semiconductor, Inc.), capable of measuring differential pressures up to 10 kPa at a sensitivity of 450 mV/kPa. The pressure sensor was calibrated by using an independent flow meter. While the pressure sensor was fixed at one of the gas outlets, the second gas outlet was connected to an electromagnetic valve. When the valve is open the pressure in the cell decreases to the ambient pressure and the H_2+O_2 gas mixture is released into the environment. The pressure increase in a single experiment is negligible; however, over a long series of experiments, pressure can build up in the cell, which may alter electrolysis conditions. The formed gas is therefore released through the valve after each experiment. The valve can be operated via the digital output terminal of the signal generator module.

The fully automated measurement system allows for carrying out a large number of water splitting experiments within a short timeframe, which facilitates the systematic exploration of frequency and amplitude effects on cell efficiency. The system is also remote-controlled, allowing for changes in experimental conditions and sampling through the internet.

Power supply ripple was modelled by applying sinusoidal waveforms between the electrodes with constant offset (DC component) and varying frequency and amplitude. Frequency was changed from 200 Hz to 5000 Hz in 100 Hz increments, while amplitude was varied from 0 mV to 440 mV in 110 mV increments. The experimental matrix therefore contained 245 cases, of which 49 were true DC cases. The offset value of the waveforms was 2436 mV ± 12 mV.

The duration of each measurement was 15 s. After completing a case, the magnetic valve was opened for 15 s and the cell was allowed to equilibrate for an additional 30 s.

Cell voltage, cell current and cell pressure were measured and recorded at a sampling rate of 50 kHz – this sampling frequency allowed for the bias-free measurement of waveform parameters. Data analysis was performed by custom software developed in C#. The custom software calculated gas flow rate and power consumption from the measured raw data. Flow rate was calculated based on the rate of linear pressure rise during an experiment, while power consumption was computed as:

$$P = \int U(t)I(t)dt \tag{1}$$

where P is power, U is the measured cell voltage and I is the measured cell current. The efficiency of water splitting (η) was calculated as the ratio of measured and theoretical gas flow rate using Faraday's law:

$$\eta = 100\mathrm{Q}\left[\frac{V_m P}{U^0 F}\left(\frac{1}{z_{H_2}} + \frac{1}{z_{O_2}}\right)\right]^{-1} \tag{2}$$

where Q is the measured gas flow rate (derived from pressure rise), V_m is the molar volume of ideal gases at standard conditions (24465 cm^3/mol), U^0 is the theoretical thermodynamic decomposition voltage of water (1.23 V), F is Faraday's number (96485 C/mol) and z is charge number (2 for H_2 and 4 for O_2). All flow rates were evaluated at standard state (25 °C, atmospheric pressure).

2. Results and discussion

Figure 3 shows the results of the 245 systematic experiments that were carried out by using the automatic system described in Section 1. It is seen that increasing the amplitude of voltage variation immediately resulted in decreasing efficiency. An increase in ripple magnitude from 0 to 443 mV resulted in an efficiency drop of about 4%. When expressed as relative magnitude, an amplitude of 443 mV corresponds to a root mean square (rms) variation of 13%, which may not be unreasonably high in an industrial setting (see Section 3.1 for details).

From Figure 3 it is also seen that the obtained efficiency values were not significantly affected by the frequency of the model waveforms, at least in the studied 0.2–5 kHz range. Figure 4 therefore shows cell efficiency along with other cell parameters as values averaged over the frequency range, in order to better show the effect of increasing signal amplitude. As seen, efficiency dropped about 4% as amplitude was increased. Cell current and gas flow rate increased very slightly with increasing amplitude – an increase of about 3% was

measured. Electric power intake, on the other hand, increased from 4.4 to 4.9 W as amplitude was increased from 0 to 443 mV, which is a relative change of about 11%. This shows, that the decrease of efficiency was mainly caused by the significantly increased power intake.

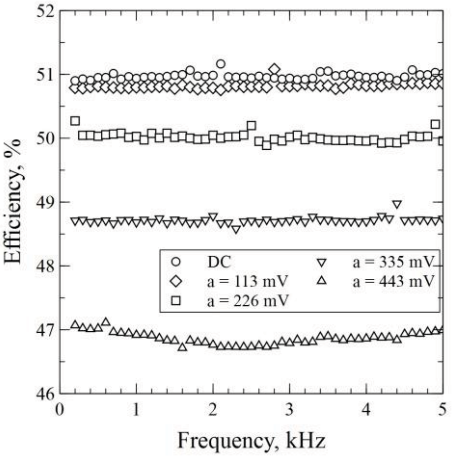

Figure 3

Efficiency as a function of the frequency and amplitude of the AC component of the model waveform. A total of 5 different amplitude setting were tested, of which the first corresponded to the true DC case (a = 0). Efficiency was reduced from about 51% to 47% as the magnitude of voltage ripple increased from 0 to 443 mV

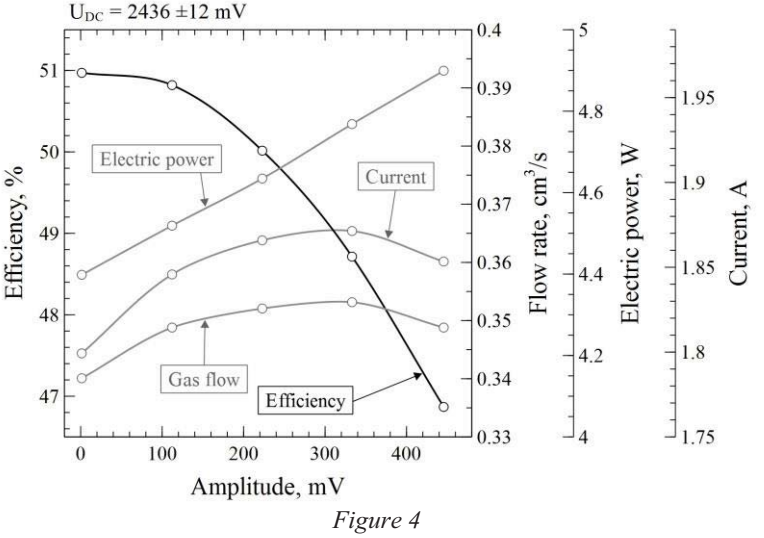

Figure 4

Water splitting efficiency, cell current, gas flow rate and electric power consumption as function of signal amplitude. The figure shows that efficiency dropped about 4% as signal amplitude increased from 0 to 443 mV. The frequency dependence of the obtained values was negligible – the standard errors of the mean values were so low that error bars are not shown in the figure. The data shown here demonstrates that the efficiency drop was mostly caused by the increased power intake of the cell. Gas flow rate remained proportional to cell current

The data show that in the investigated frequency and amplitude range, the mass transfer and electrochemistry of the process did not change considerably. Efficiency was rather decreased by the increased power intake of the cell, which was caused by the oscillation of voltage and current. If the voltage and current signals are expressed as the superposition of a DC and AC component (assuming that there is a phase shift Φ relative to the voltage signal):

$$\begin{aligned} U &= U_{DC} + u = U_{DC} + a_U \sin(\omega t) \\ I &= I_{DC} + i = I_{DC} + a_i \sin(\omega t + \phi) \end{aligned} \tag{3}$$

where the index DC means the constant component, ω is radial frequency, t is time and a_U and a_I are the amplitudes, the power increase ΔP over the direct current case is the integral of the two time-varying components:

$$\Delta P = \frac{a_I a_U}{2} \tag{4}$$

When carrying out the correction of measured power by Equation 4, the drop in energy efficiency indeed proved to be around 4%, justifying our previous statement about the main cause of the efficiency drop.

By looking at the current efficiency, expressed as:

$$\eta_I = 100Q\left[\frac{V_m I}{F}\left(\frac{1}{z_{H_2}} + \frac{1}{z_{O_2}}\right)\right]^{-1} \tag{5}$$

it was observed that η_I decreased from approximately 99.7% to 99.1% as amplitude increased. The very slight change indicates that the electrochemistry of the system was not changed much by increased ripple magnitude in the studied limits.

By looking at the measured voltage and current signals, a phase shift was observed, which is shown in Figure 5.

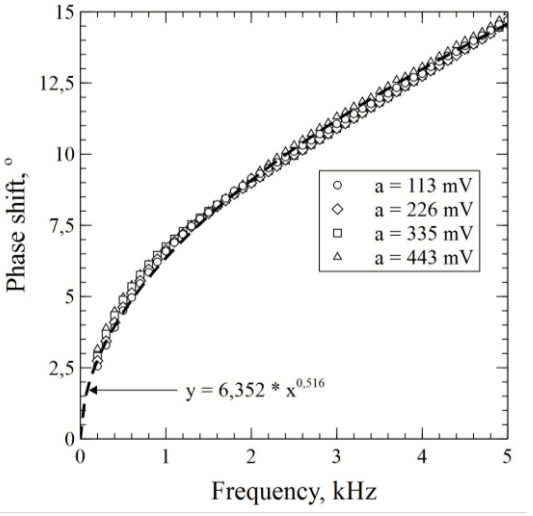

Figure 5
Phase shift between cell voltage and current. The phase shift increased with increasing frequency, but was fairly independent of ripple amplitude

As seen, the phase shift between voltage and current signals increased with increasing frequency, but was unchanged by increasing ripple amplitude. This indicates the capacitive behavior of the cell, while also pointing out that the effect of phase shift on cell power was not noticeable in the frequency limits investigated in this work. At higher frequencies, phase shift might affect cell efficiency. Further studies using the experimental system described in this paper may elaborate.

3. Notes on power supplies

Common silicon controlled rectifier (SCR) regulation techniques permit the design of low cost, compact power supplies, but their main disadvantage is relatively high ripple and noise [18]. For example a single phase, unfiltered, full-wave DC rectifier used in low power applications has around 48% rms ripple [19] at frequency 100 Hz, and a 3-phase rectifier used in high power applications has around 5% rms [20] at frequency 300 Hz. With inverter-grade thyristors the frequency can be increased to 600 Hz [21]. By reducing the output power in unfiltered 3-phase thyristor controlled rectifiers, the output ripple significantly grows – at 50% output power the ripple is around 40% rms [22]. Publications show that the voltage ripple can reach up to 60% rms [23]. To put these numbers into perspective, the highest magnitude ripple studied in this work was around 13%, which resulted in an energy efficiency loss of 4%. Although the ripple of the power supplies are mostly given for output voltage, in order to calculate or appreciate the efficiency loss the ripple of the electric current must also be known, what depends basically on the load.

By adding filters to a thyristor based rectifier the ripple can be reduced to 0.8% rms at full load, and a ripple of 2.8% rms is typical at 50% power [22]. According to our results, a ripple of similar magnitude causes an efficiency drop of 0.15%. By adding a filter to an SCR the ripple is lower, however, the overall cost of the power supply increase. The transistor based power supplies operates at much higher frequencies (from 5–10 kHz) than SCR, and their ripple is significantly lower, but the disadvantages are the higher cost and their usage in high power applications are not fully formed as yet.

Considering the strict requirements regarding energy efficiency in order to make water electrolysis a feasible technique for sustainable hydrogen production, it is therefore advisable to design electrolysis systems with an emphasized consideration of power supply stability. Since the rms ripple of typical power supplies increase when the unit is operated sub peak power, it is also advisable to avoid such modes of operation or provide other means to maintain cell efficiency at reduced powers.

Summary

The effect of power supply ripple on the efficiency of alkaline water electrolysis for hydrogen production was investigated. For the study, a novel, automated measurement system was used, that allowed for the remote collection of data from thousands of programmed experiments. Power supply ripple was modelled by applying sinusoidal voltage to an electrolysis cell. The voltage signals had a constant offset (DC component) and an alternating component with variable frequency and amplitude. A frequency range of 200–5000 Hz and an amplitude range of 0–443 mV was studied at an offset of 2.44 V. Results showed that the energy efficiency of the electrolysis process was not affected significantly by the source frequency, but was affected by the amplitude (the magnitude of the ripple). Cell efficiency dropped from 51% to 47% when the signal amplitude was increased from 0 to 443 mV (0–13% rms). The efficiency loss was mostly caused by the increased power consumption of the

cell, due to the effective power of the alternating components of voltage and current signals. Observations regarding current efficiency supported this conclusion, as current efficiency did not change much with increasing signal amplitude. The phase shift between cell voltage and current did not have a noticeable effect on cell efficiency in the studied frequency range. The results suggest that power supply signal stability must be an important factor in designing alkaline water electrolysis units, as typical ripple magnitudes may lead to significant efficiency drop.

Acknowledgement

This research was (partially) carried out in the framework of the Center of Excellence of Sustainable Resource Management at the University of Miskolc.

References

[1] Holladay, J. D.–Hu, J.–King, D. L.–Wang, Y.: An overview of hydrogen production technologies. *Catalysis Today*, 139, 2009, 244–260.

[2] Turner, J.–Sverdrup, G.–Mann, M. K.–Maness, P. C.–Kroposki, B.–Ghirardi, M.–Evans, R. J.–Blake, D.: Renewable hydrogen production. *International Journal of Energy Research*, 32, 2008, 379–407.

[3] Grimes, C. A.–Varghese, O. K.–Ranjan, S.: *Light, Water, Hydrogen – The solar generation of hydrogen by water photoelectrolysis*. Springer, 2008.

[4] Nikolic, V. M.–Tasic, G. S.–Maksic, A. D.–Saponjic, D. P.–Miulovic, S. M.–Kaninski, M. P. M.: Raising efficiency of hydrogen generation from alkaline water electrolysis – Energy saving. *International Journal of Hydrogen Energy*, 35, 2010, 12369–12373.

[5] Wang, M.–Wang, Z.–Guo, Z.: Water electrolysis enhanced by super gravity field for hydrogen production. *International Journal of Hydrogen Energy*, 35, 2010, 3198–3205.

[6] Li, S.-D.–Wang, C.-C.–Chen, C.-Y.: Water electrolysis in the presence of an ultrasonic field. *Electrochimica Acta*, 54, 2009, 3877–3883.

[7] Lin, M.-Y.–Hourng, L.-W.–Kuo C.-W.: The effect of magnetic force on hydrogen production efficiency in water electrolysis. *International Journal of Hydrogen Energy*, 37, 2012, 1311–1320.

[8] Marini, S.–Salvi, P.–Nelli, P.–Pesenti, R.–Villa, M.–Berrettoni, M.–Zangari, G.–Kiros, Y.: Advanced alkaline water electrolysis. *Electrochimica Acta*, 82, 2012, 384–391.

[9] Wang, M.–Wang, Z.–Gong, X.–Guo, Z.: The intensification technologies to water electrolysis – A review. *Renewable and Sustainable Energy Reviews*, 29, 2014, 573–588.

[10] Mazloomi, K.–Sulaiman, N.–Ahmad, S. A.–Yunus, N. A.: Analysis of the frequency response of a water electrolysis cell. *International Journal of Electrochemical Science*, 8, 2013, 3731–3739.

[11] Shimizu, N.–Hotta, S.–Sekiya, T.–Oda, O.: A novel method of hydrogen generation by water electrolysis using an ultra-short-pulse power supply. *Journal of Applied Electrochemistry*, 36, 2006, 419–423.

[12] Vanags, M.–Kleperis, J.–Bajars, G.: *Water electrolysis with inductive voltage pulses*. *Electrolysis.* Chapter 2. Published by InTech, 2012.

[13] Shaaban, A. H.: *Pulsed DC and anode depolarization in water electrolysis for hydrogen generation.* HQ air force civil engineering support agency, final report, 1994.

[14] Mazloomi, S. K.–Sulaiman, N.: Influencing factors of water electrolysis electrical efficiency. *Renewable and Sustainable Energy Reviews*, 16, 2012, 4257–4263.

[15] Mazloomi, K.–Sulaiman, N. B.–Moayedi, H.: Electrical efficiency of electrolytic hydrogen production. *International Journal of Electrochemical Science*, 7, 2012, 3314–3326.

[16] Ursúa, A.–Marroyo, L.–Gubía, E.–Gandía, L. M.–Diéguez, P. M.–Sanchis, P.: Influence of the power supply on the energy efficiency of an alkaline water electrolyser. *International Journal of Hydrogen Energy*, 34, 2009, 3221–3233.

[17] OPA549 type operational amplifier, technical datasheet (2016. 04. 06.) http://www.ti.com/lit/ds/symlink/opa549.pdf
[18] A. Technologies: *DC power supply handbook* (2016. 04. 06.) http://educypedia.karadimov.info/library/DC%20Power%20Supply%20Handbook.pdf
[19] MENTONE, P. F.: Pulse vs. DC plating: Knowing how and when to use each system is critical for producing plated metals. *Metal Finishing*, 103, 2005, 14–18.
[20] SMITH, C. C.–CAMBRIA, P.: DC power supplies. *Metal Finishing*, 97, 1999, 679–702.
[21] SINGH, M. D.– KHANCHANDANI, K. B.: *Power Electronics*. McGraw-Hill, 2008.
[22] What is ripple? (2016. 04. 06.) http://www.controlledpwr.com/whitepapers/ripple_formula.pdf
[23] STEIN, B.: Effects of voltage ripple on plating uniformity in chloride zinc baths. *Metal Finishing*, 93, 1995, 100–103.

Materials Science and Engineering, Volume 41, No. 1 (2016), pp. 32–38.

THE ELIMINATION OF THE UNFAVOURABLE INFLUENCE OF STEEL SCRAP IN THE CHARGE ON THE QUALITY OF CAST IRON

PETER FUTÁŠ[1]–ALENA PRIBULOVÁ[2]–ŠTEFAN NIŽNÍK[3]–
GABRIEL DÚL[4]–LÁSZLÓ VARGA[5]

Currently grey cast iron is the most widely used material in foundries. It is characterized mainly by its good technological and mechanical properties, which are required by certain metallurgical processes, and its solidifying and cooling conditions. There are a number of factors in metallurgy that can influence the final quality of cast iron: charge material, chemical composition, metallurgical preparation and finishing process of the casting. Small changes in the metallurgical processes cause variable melt quality and the development of castings defects. The charge material, especially its steel scrap content, has a strong influence on the quality of grey iron. After melting in electric furnaces, steel scrap is used to produce cast iron, mainly for economic reasons. Its capability of increasing the hardness and strength of cast iron has already been documented. However, the influence of the steel content of the charge on the final quality of the cast iron and on its properties are still unexplored issues. Also, the effects of the nitrogen content on the properties is still unknown. Therefore, the examination of the influence of high amount of steel scrap in the charge on the quality of cast iron is substantial.
Keywords: grey cast iron, degree saturation, charge materials, steel scrap, nitrogen in grey iron

Introduction

The impact of the charge material on the quality of grey iron is extensive. For economic reasons, re-melted steel scrap is widely used for producing grey cast iron.

Pig iron is one of the basic materials of metallic charges and has a great influence on the chemical composition and the properties of cast iron, and also on the cost of the production. It has been confirmed that the properties are effected by trace elements and other additives, like oxygen, nitrogen and hydrogen. The effect of these elements can be suppressed by overheating the grey iron and with higher basicity slag. The content of gases, hydrogen, nitrogen and oxygen in pig iron ranges from 30 to 80 ppm.

The typical quantity of steel scrap used is between 10–50%. The more the production cost of the charge is to be reduced, the higher content of steel scrap is used. During the

[1] Technical University of Košice
Letná 9; 04001 Košice, Slovak Republic
[2] Technical University of Košice
Letná 9; 04001 Košice, Slovak Republic
[3] Technical University of Košice
Letná 9; 04001 Košice, Slovak Republic
[4] Technical University of Košice
Letná 9; 04001 Košice, Slovak Republic
[5] University of Miskolc, Institute of Foundry
Miskolc-Egyetemváros 3515, Hungary
ontvlaci@uni-miskolc.hu

production of synthetic grey iron, the use of carburising agents with low sulphur, nitrogen and ash content is necessary. The high steel scrap content of the charge increases the tendency of chill wedge, shrinkage and perlite development. The content of nitrogen in steels is between 0.003–0.0160 percent. A small amount of nitrogen already increases the mechanical properties of grey cast iron, especially hardness, and leads to shrinkage and the development of chill [1, 2, 3].

1. Experimental part

On the basis of the initial statistical results from 122 melts [4, 5, 6], five experimental melts of grey cast iron were prepared from standard EN-GJL-250 at a constant degree of saturation (Sc):

Melt 1 – the most commonly produced half-synthetic grey iron, based on current production data;
Melt 2 – half-synthetic grey iron with the melt overheated to 1500 °C;
Melt 3 – half-synthetic grey iron alloyed with titanium, overheated;
Melt 4 – synthetic grey iron with carbon increased by 0.5%, compared to melt 1, and reduced silicon content due to the nitrogen being bounded by carbon, overheated;
Melt 5 – fully synthetic grey cast iron (100% steel scrap).

All of these were melted in a Siemens medium frequency induction furnace with the following parameters:

- nominal capacity of the furnace: 6 tons
- melting power: 5350 kg/h
- nominal frequency: 500 Hz

The cast iron was treated with FeSi75 during the heat treatment.
Next, samples were casted from the melts for various analyses:

- samples for chemical analysis;
- samples for step-down test to determine the correspondence between the thickness and hardness of the walls. Figure 1 shows an example of a block with 100, 50 and 20 mm diameter sections which are standard values for the walls of castings;
- test bars for tensile tests, 30 mm in diameter each (Rm);
- wedge-shaped test bars, Figure 2 [7];
- samples to determine the shrinkage tendencies: cylinder with a diameter of 95 mm and a height of 150 mm;
- samples to determine the nitrogen content of the grey cast iron.

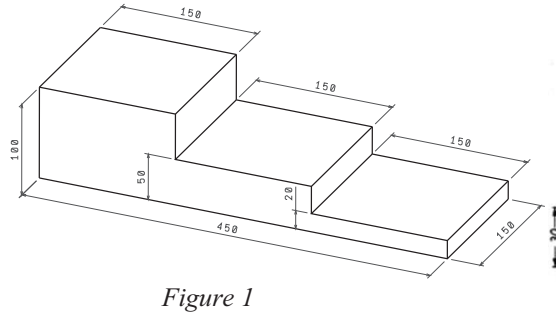

Figure 1
Step-down test

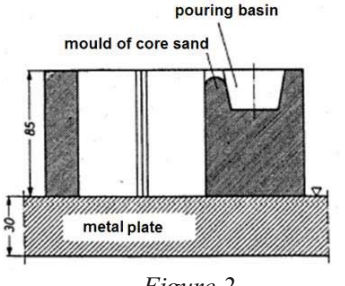

Figure 2
Wedge-shaped test bar

Samples for metallographic analysis were taken from the test bars and prepared in a standard manner.

Blocks were cut in each cross sectional areas. Brinell hardness was measured on every section with a HPO 3000 durometer. The hardness values were obtained using a 10 mm diameter ball with 3000 N force applied for a period of 10 seconds – 10/3000/10.

The tensile strength of the test bars, which were 30 mm in diameter, was measured with a universal ZWICK crackle machine.

2. Results and discussion

Table 1 shows data on the mechanical properties, the degrees of saturation (Sc), the carbon equivalents, the depth of chills and the tensile stresses of the melts.

Table 1

Results of chemical analyses, mechanical properties, depth of chills and tensile stresses

Melt	Portion of steel scrap [%]	wt. [%]			Sc	CE [%]	Rm [MPa]	HB	Depth of chill [mm]
		C	Si	N_2					
1	33	3.23	1.612	0.0113	0.848	3.721	297.25	185.87 *(205.25)	5
2	35.5	3.33	1.52	0.0152	0.868	3.793	351.75	204.58 *(223.78)	1
3	35.5	3.32	1.486	0.0091	0.863	3.773	268	217.02 *(224.50)	1
4	81.7	3.79	1.026	0.0073	0.951	4.103	256.25	211.81 *(221.22)	6
5	97.8	3.28	1.69	0.0175	0.869	3.805	257.67	243.84 *(312)	10
* HB measured on the thinnest wall of the samples (20 mm)									

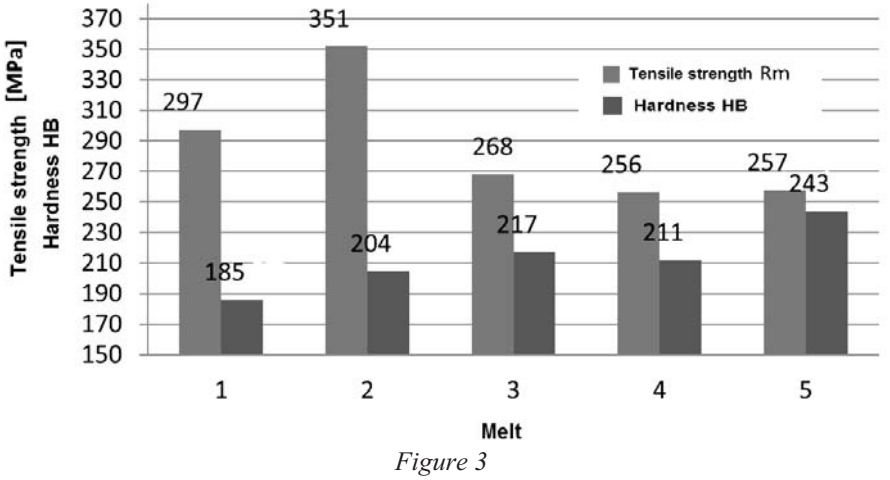

Figure 3

Tensile strength and Brinell hardness values of the melts

The tensile strength and the Brinell hardness of melt 1–5 are shown in Figure 3. All melts were undereutectic cast irons, the degree of saturation was always under 1 and the carbon equivalent was under 4.23. The data on the chemical composition and the mechanical properties correspond to the EN standard for cast iron GJL-250. All melts were inoculated with approximately 0.2% wt. "INOCAST" or approx. 0.3% wt. SiC during the heat treatment.

According to the chemical analyses, the degree of saturation was between 0.848–0.869 in all but one of the melts. Melt 4 had high carbon and low silica content, and low degree of saturation, all of which correspond to the EN standard GJL-250. The nitrogen content was the lowest in melt 4 and 3, the latter of which was alloyed with titanium. Melt 5 had the highest nitrogen content, the source of which was the steel scrap the sample was made out of.

The tensile strength results complied with the EN standards in case of all melts. Melt 5 had the lowest value, 257 MPa, so in this case overheating above 1450 °C is required. The expected impact of the high nitrogen content on the tensile strength could not be observed.

The Brinell hardness values ranged from 185 to 243 at 50 mm wall thickness which corresponds to standard STN and EN-GJL-HB255 (185–200 HB). It was remarkably high in melt 5.

The dependency of hardness on the wall thickness for each melts is shown in Figure 4.

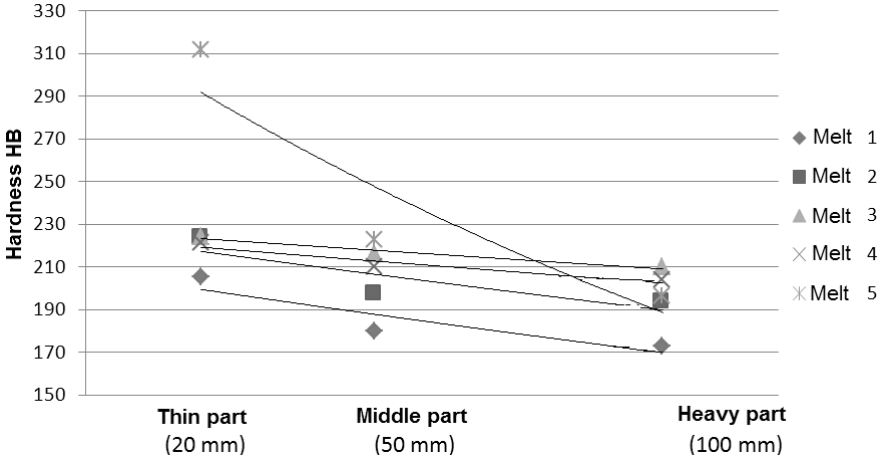

Figure 4
The change of the Brinell hardness of the blocks

The depth of chill was the highest, up to 10 mm, in melt 5. This indicates that nitrogen has negative impact on the depth of chill, whereas it increases the stability of carbides and perlite in the structure.

The depth of chill in melt 2 and melt 3 was 1 mm. The reason behind this was the overheating in case of melt 2, and the negative effect of nitrogen influenced by the titanium content in melt 3. In melt 1, which was the standard melt, the depth was 5 mm.

Synthetic cast iron had the greatest degree of shrinkage which reached 15 mm and had the greatest cross section with 30 mm, which confirms the negative impact of nitrogen. In the other melts, shrinkage was approximately 18 mm in diameter and 4 mm deep.

The results of the metallographic analyses are shown in Table 2.

Table 2
The results of the metallographic analyses

Melt No.	Perlite in structure [%]	Graphite size [µm]	Allocation of lamellar graphite
1. standard melt	92	60–120	Type C – mixed
2. overheated to 1500 °C	96	60–120	Type D – interdendritic undirected
3. melt with Ti	96	30–60	Type E – interdendritic undirected
4. higher C content	96	120–250	Type C – mixed
5. full-synthetic	100	60–250	Type C – mixed

The allocations of lamellar graphite were type C, D, and also type E in melt 3, in which the lamellae were shorter, thinner and corrugated, typically 30–60 µm long. Microstructures of melt 3 are shown in Figure 5 and microstructures of melt 2 in Figure 6.

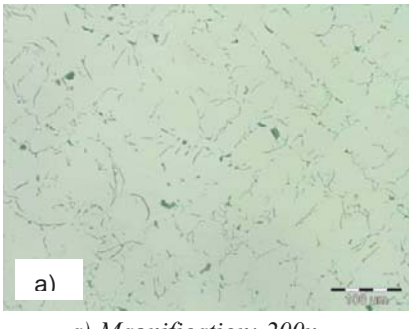

a) Magnification: 200x

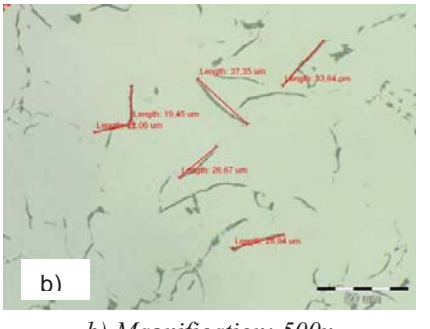

b) Magnification: 500x

Figure 5
Microstructures of melt 3

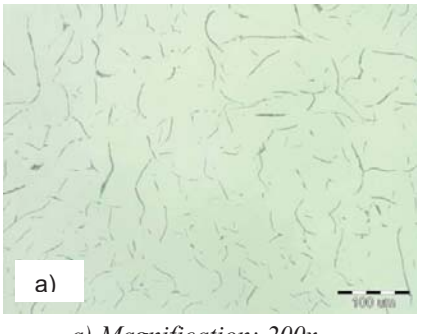

a) Magnification: 200x

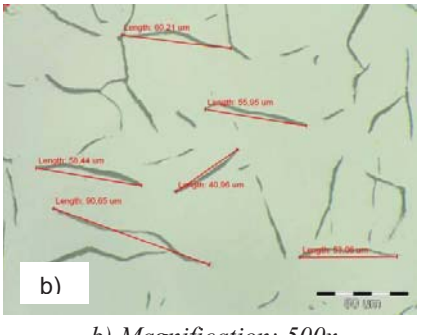

b) Magnification: 500x

Figure 6
Microstructures of melt 2

Cementite was not observed in the structure of the melts which was the result of the inoculation. Melt 5 had fully pearlitic microstructure and carbide could also be detected in the structure, as shown in Figure 7. The presence of carbide was the cause of the higher hardness of this grey iron sample.

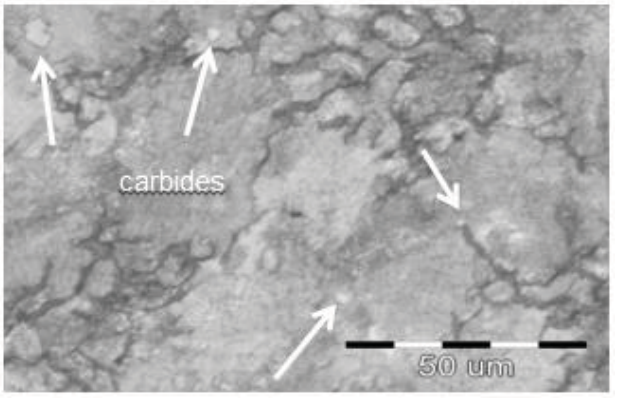

Figure 7
Microstructure of melt 5 after 2% nital etching; 500x magnification

Conclusions

The quality of cast iron is influenced by a large number of factors from which the influence of steel scrap in the charge and the nitrogen content are especially important. The correspondence between the increase in some mechanical properties, i.e. Brinell hardness, and the thickness of the walls can be observed. A significant difference could be noticed in the hardness of the thin- and thick-walled cross-sections in case of the fully synthetic cast iron. Melt 2 had the highest tensile strength value and the lowest deviation of Brinell hardness in case of the different wall thicknesses.

The quality of the grey cast iron is partially based on customer requests but also on financial conditions. The use of steel scrap has a significant importance in achieving the desired mechanical properties, in particular, the hardness of the cast iron. As the results showed, the negative impacts of high steel scrap content could be eliminated by inoculation, overheating the melt up to 1500 °C, and alloying with 0.1–0.3% titan.

The cost of the metal accounts for approximately 40% of the total production cost of castings made from grey cast iron. In conclusion, the composition of the charge should receive more attention for the above-mentioned reasons.

On the basis of the obtained information, melt 4 and 5 are recommended for the production of thick-walled castings and melt 3 for thin-walled castings.

During the production of thick-walled castings with higher hardness, alloying with up to 0.5% chromium is recommended in addition to overheating and inoculating the melt.

Acknowledgements

This work was supported by the Scientific Grant Agency of the Ministry of Education of the Slovak Republic No. VEGA 1/0836/12.
The authors are grateful to Mária Ambrus for her advice.

References

[1] FUTÁŠ, P.–PRIBULOVÁ, A.–VASKOVÁ, I.: Influence of steel scrap in a charge on cast iron properties. *Archives of Foundry Engineering*, Vol. 8, No. 2 (2008), 71–74.

[2] MORES, A.: Technické požadavky a přejímaní odlitků z litiny s kuličkovým grafitem. *Slévárenství*, Vol. XLIX, No. 5–6 (2001), 355–361.

[3] KIJAC, J.–SLADÍKOVÁ, R.–BUĽKO, B.–BOROVSKÝ, T.: The Nitrogen Content Management in the Oxygen Converter Steelmaking. *Metalurgija*, Vol. 51, No. 2 (2012), 191–194.

[4] FUTÁŠ, P.–PRIBULOVÁ, A.: Quality criteria as implement for advisement of metallurgical quality of grey iron. In: BORKOWSKI, S.–ROSAK-SZYROCKA, J.: *Evaluation of people and products features*. University of Maribor, Celje, Slovenia, 2014, 99–118.

[5] FUTÁŠ, P.–JELČ, I.–BARTOŠOVÁ, M.: Usage of Quality Criteria for Advertisement of Metalurgical Quality of Grey Cast Iron. *Quo Vadis Foundry IV conference*, Tále, 10–12. 10. 2012, Košice, Slovakia, 2012, 58–64.

[6] FUTÁŠ, P.–JELČ, I.–VASKOVÁ, I. et al.: The Gist of Thermal Stresses of Cast Iron Castings. *Manufacturing technology*, Vol 13, No. 2 (2013), 173–177.

[7] ROUČKA, J.: *Metalurgie litin.* PC–DIR, Brno, 1998.

Materials Science and Engineering, Volume 41, No. 1 (2016) pp. 39–50.

CELLULAR AUTOMATA SIMULATION OF THE ALLOTROPIC TRANSFORMATION OF URANIUM

SZILVIA GYÖNGYÖSI[1]–PÉTER BARKÓCZY[2]

Cellular automata are non-conventional calculation methods [1]. Both the method itself and its applications are being researched. In literature numerous examples show its use in the field of materials science. In our previous studies simulations of short-range diffusion using cellular automata were presented. Simulations for recrystallization, grain coarsening and allotropic transformation were developed [1, 2, 3]. It was also presented that the automata can be scaled with the Nelder-Mead simplex procedure [4]. After further development and increasing the efficiency one-dimensional automata were created for recrystallization and grain coarsening showing that these versions of the automata can be fitted to measurement results thus providing applicability in simulation tasks [5, 6, 7]. In this study one-dimensional automata results are shown for allotropic transformation where, similarly to previous results, the data follow the kinetics of the process. Furthermore, the scaling of the results calculated by the automata using literary information on uranium measurements is presented.
Keywords: cellular automata, fitting, scaling, Nelder-Mead, simplex, allotropic transformation, uranium

Introduction

In this study the allotropic transformation processes of uranium are examined using cellular automata simulations. Three allotropes of uranium are knows, these are α – orthorhombic, β – tetragonal and γ – face-centered cubic which are respectively more stable with increasing temperature. According to the U-Zr phase diagram reviewed by OKAMOTO [12] the transformation temperatures are as follows: $\alpha \rightarrow \beta$ transformation 941 K (668 °C), $\beta \rightarrow \gamma$ transformation 1049 K (776 °C). Nowadays mostly metallurgical researches of actinoids trend towards the allotropic transformations of pure uranium, therein the effect of cooling and heating rate on the transformation temperature is also researched. It was found that the transformation temperatures of $\gamma \rightarrow \beta$ and $\beta \rightarrow \alpha$ are sensitive to the cooling rate, the most sensitive allotrope being the face-centered cubic (γ). In fact some details of the aforementioned phase transformations are unclarified to date that resulted in several scientific disciplines paying attention to these transformations recently. Major advancements were made in the field of physical metallurgy on both the historic and experimental fronts. These advancements mostly cover the kinetics of the transformations and controlled phase transformations. Understanding the transformation kinetics has high significance as supported by the continuously growing applications of uranium (for example, choosing the optimal composition in the case of metal-based fuels in reactor-technology). The most widely accepted examination method for similar aims is the differential scanning calorimetry (DSC).

[1] University of Debrecen, Department of Solid State Physics
H-4026 Debrecen, Bem tér 18/B., Hungary
gyongyosi.szilvia@science.unideb.hu
[2] University of Miskolc, Institute of Materials Science, FUX Co.
peter.barkoczy@fux.hu

1. Allotropic transformations of uranium

For our calculations literary data were used [9]. Arun Kumar Rai et al. examined the allotropic transformations of uranium (composition of sample in Table 1) using DSC at different cooling and heating rates (10^0–10^2 $Kmin^{-1}$) while following the process of the transformation.

Table 1
Chemical composition of the sample (ICP-AES) [9]

Al	Cd	Ce	Co	Cr	Dy	Er	Eu	Fe	Gd	Mg	Mn	Ni	Sm	Y	Yb	C	N	O	Si
349	<0.12	2.2	0.2	15	<0.1	<0.1	<0.04	74	0	11	9.3	33	0.4	<0.1	<0.1	316	246	552	615

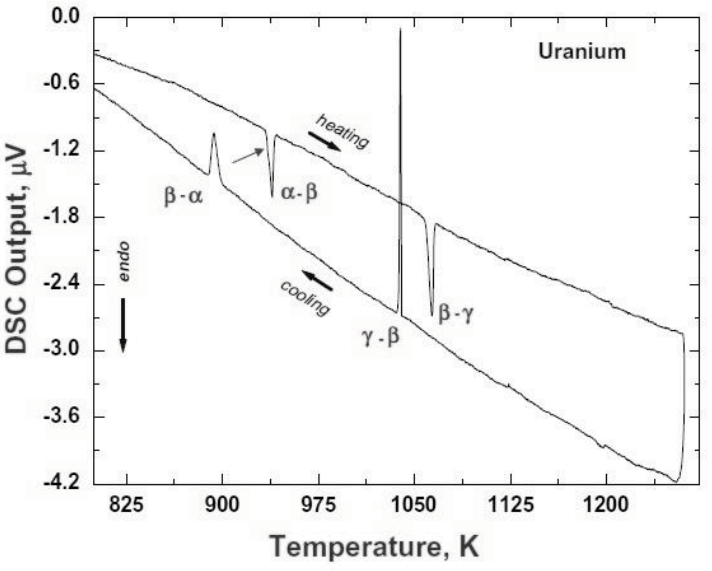

Figure 1
Typical DSC profile for uranium (3 $Kmin^{-1}$) [9]

Cast samples with average grain sizes of 300–400 μm were used for the measurements. This has to be taken into account during the evaluation of simulation results as a significant factor in the transformation kinetics. In addition, considerable amount of uranium-silicide phases segregated on the grain borders were identified.

In the examined temperature range (200 °C–1050 °C) the solubility of silicon in uranium does not change in a significant way [18, 19, 20], thus the presence of phases does not affect the kinetic examination. The measurements were performed in a heat-flux DSC device. One of the characteristics of heat-flux DSC devices is that the measured signal is slightly behind the actual transformation due to the finite rate of heat equalization [18, 19, 20]. This does not change the method of evaluation, however, it has to be taken into account during the scaling of the simulation, especially in the case of high heating rates. An example of the measurement results is shown on Figure 1. where the heating and subsequent cooling program used for examining allotropic transformations is visible. A typical DSC profile can be seen on Figure 1 where the peaks corresponding to certain transformations are shown. During heating the α

→ β and β → γ transformations happen according to the well-known Johnson–Mehl–Avrami– Kolgomorov (JMAK) model for nucleation and growth which is also true for cooling (Figure 2–5).

The large grain size of the sample cannot be considered basic as it is only true before the α → β transformation after which the new grain size affects the kinetics. Since the grain size depends on the cooling and heating rates and the kinetics depend on the grain size, which is not known from the measurements, the effect of grain size cannot be taken into account during the fitting of the simulation. A fitting optimization task is present as a future plan to examine the effect of the grain size by refining the fitting results for which further data is required.

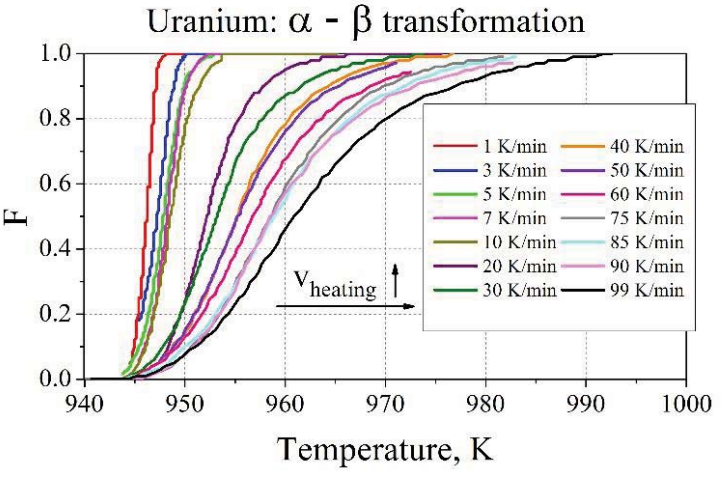

Figure 2
Transformed fraction curves during α → β transformations of uranium in the case of heating

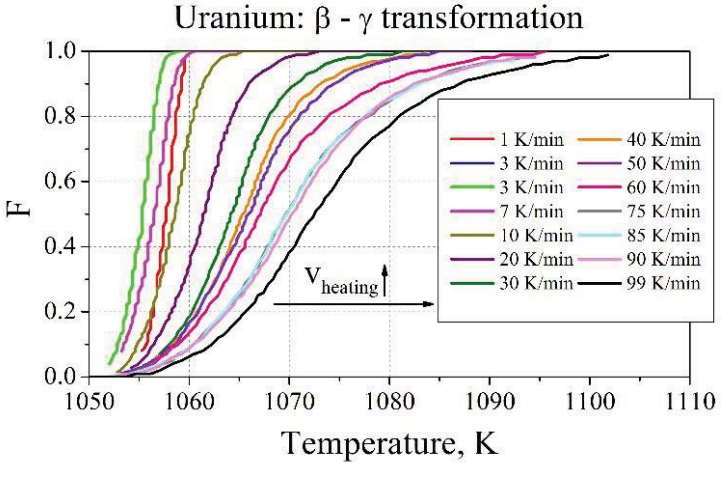

Figure 3
Transformed fraction curves during β → γ transformations of uranium in the case of heating

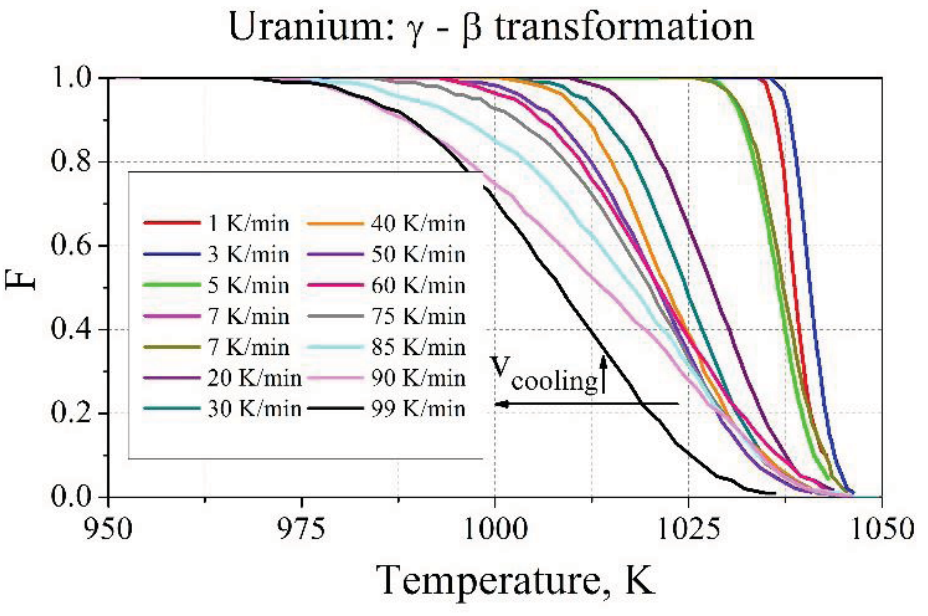

Figure 4
Transformed fraction curves during γ → β transformations of uranium in the case of cooling

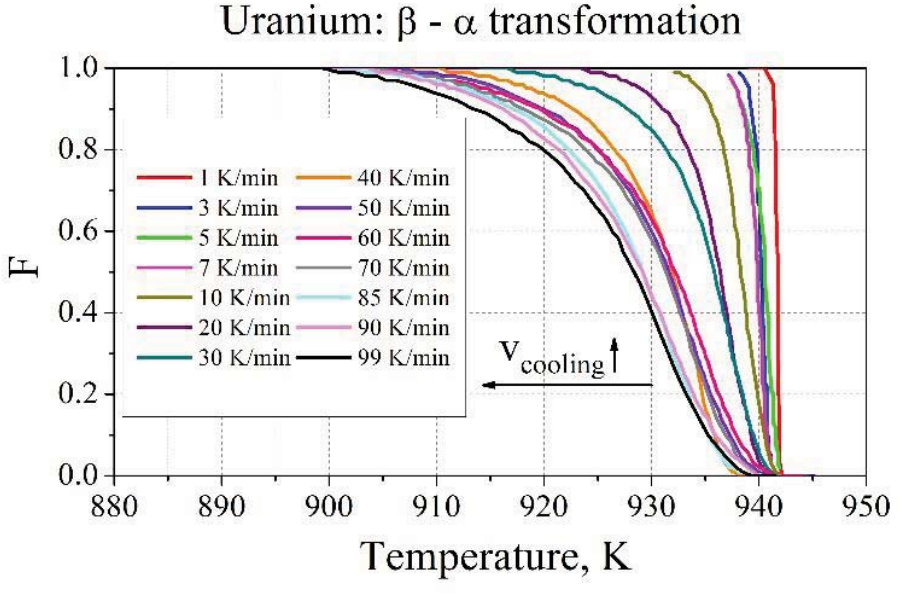

Figure 5
Transformed fraction curves during β → α transformations of uranium in the case of cooling

2. One-dimensional cellular automata simulation of allotropic transformation

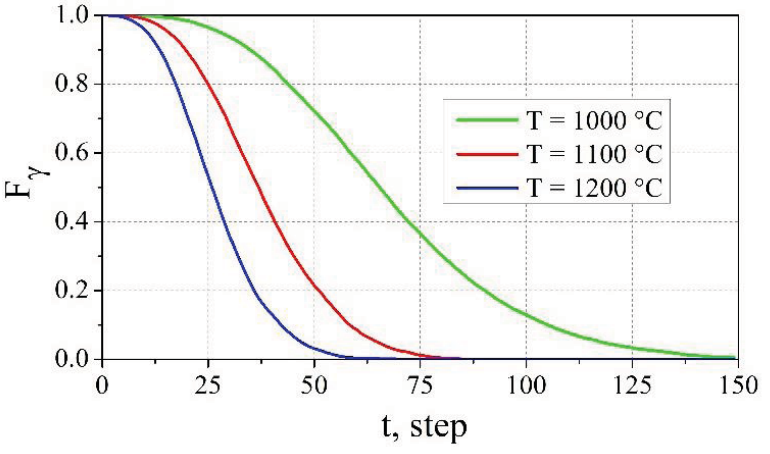

Figure 6
Transformed fraction as a function of time during γ → α transformation

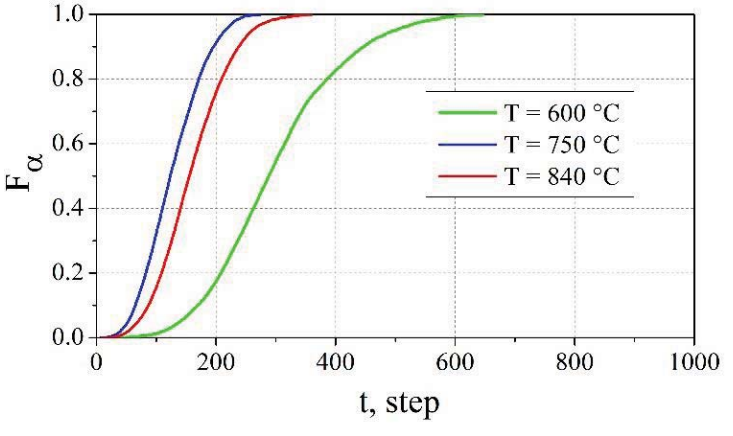

Figure 7
Transformed fraction as a function of time during α → γ transformation

The automata works in a synchronic, stochastic principle in one dimension [8]. The cell chain is built from 10,000 cells [1]. Periodic boundary conditions were used for the first and last element of the universe to solve the problem of missing neighbours. A cell may take one of two states, 1 or 0, which states serve as phase indicators (stable or unstable). The neighbourhood of a cell consists of the cells in front of it and behind it. The driving force of allotropic transformations is the difference in free enthalpy between the stable and the unstable phases. The main parameters of the automata are the nucleation (Q_n) and growth (Q_g) activation energies, the phase border energy and the temperature. The allotropic transformation is a nucleation and growth process that serves as the base for two rule systems for the mentioned subprocesses. The rule system for nucleation defines that a nuclei is only

formed from a cell if the cell and all of its neighbours are in an unstable phase. Growth starts when the examined cell is unstable and has at least one stable neighbour. If the possibility process permits it, the new state of the cell will be stable.

The test results of the automata are shown on Figure 6–7. The examination was performed with Qn = 120,000 J/mol and Qg = 60,000 J/mol values. From the results the transformed fraction curves were determined for both $\gamma \rightarrow \alpha$ and $\alpha \rightarrow \gamma$ transformations. During the simulation test iron was used as a base with 911 °C as transformation temperature below which the base-centered cubic α-iron and above which the face-centered cubic γ-iron is the stable phase.

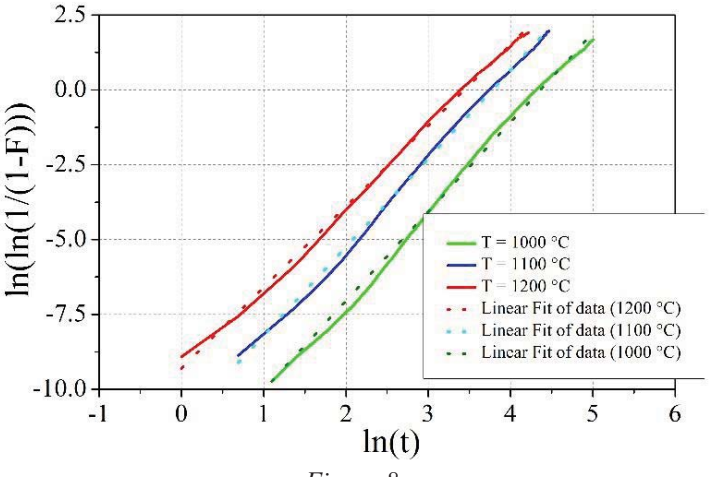

Figure 8
JMAK kinetics in the cases of γ → α transformations

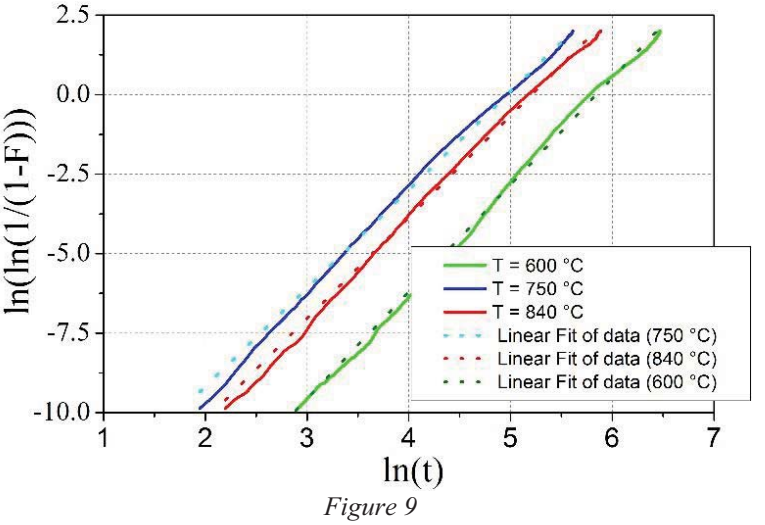

Figure 9
JMAK kinetics in the cases of α → γ transformations

Investigating Figure 6 depicting the $\alpha \rightarrow \gamma$ process it is visible that the process is faster at a higher temperature which is in correspondence with reality. In the case of the reverse process on Figure 7 it is visible that the process is faster at a lower temperature while at the same time it slows down as a result of the atoms moving slower. This also means that the transformation at 750 °C is shifting towards a shorter time period compared to the one at 840 °C while the transformation at 650 °C takes more time compared to the other two. The results coincide with the physical reality.

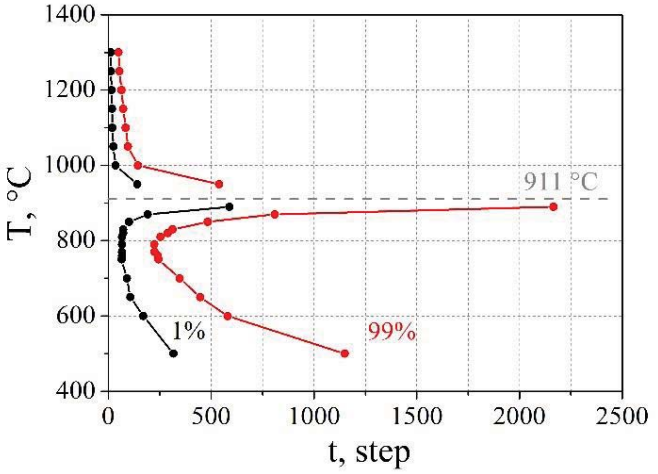

Figure 10
Transformation diagram from one-dimensional cellular automata

Performing the JMAK analysis on the results it is visible that the process follows the presumed kinetics (Figure 8–9). Allotropic transformations are usually described using the transformation diagram. Calculations were performed for the diagrams as well. Running the automata on different temperatures above and below the transformation temperature creates the transformation diagram (Figure 10).

3. Fitting

In cellular automata time passes in the form of calculation steps. From the aspect of distance the cell is the base unit. Since these are not real values, they limit the practical use of the automata. In simulations however, effect from changes in parameters can be examined that cannot be examined in any other way. In my research the Nelder–Mead simplex algorithm was chosen for scaling from the global optimization methods.

This method belongs to the family of direct searching procedures [13, 14]. Only a small amount of points is required at start that decreases the number of necessary function evaluations at each iteration. For N variables N+1 points in the parameter space are required. If two parameters are given, the searching procedure starts from three points on the given surface. For a function with two variables the three points have to be chosen to avoid being on the same line [15, 16, 17]. First the worst point of the simplex is being searched, then according to certain rules a new simplex is determined from the old one. These rules are reflection, contraction and expansion [15, 16, 17]. With these rules it can be achieved to get as far from the worst point as possible.

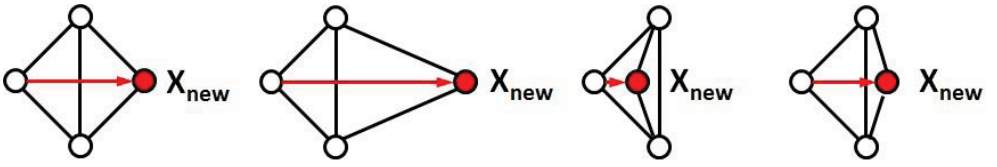

Figure 11
Simplex method rules (a) reflection, (b) expansion and (c), (d) contraction [15, 16, 17]

Ignoring the worst point the median of the others is determined. The worst point is then reflected on the median [Figure 11 a)]. This creates the new point (X_{new}) and the new simplex. If the new point is more suitable for the function than the best point of the old simplex, the advancement is favourable and the new point is moved in this direction. This is the expansion [Figure 11 b)]. If the new point means a worse case than the best point of the old simplex, it is taken as a wrong direction and the point is moved to the opposite of the reflection direction (expansion). If the function value is better than the best and worse than the second worst point, contraction is used [Figure 11 d)]. The new point replaces the worst point and the algorithm continues with the new simplex [15, 16, 17].

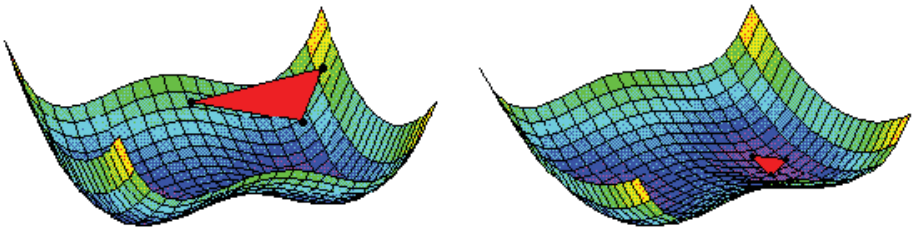

Figure 12
Nelder–Mead simplex method (a) starting simplex, (b) ending simplex [15]

In this research the mentioned global optimization procedure was used. Based on the Nelder–Mead algorithm a function depending on the nucleation and growth activation energy which shows the sum of squares of the differences between the measured and calculated transformed fraction curves. The best fitting of the two curves is realized in the minimum of the surface described by the previous function. This minimum was found with the simplex procedure. The procedure starts from three points in case of two parameters. Ignoring the point corresponding to the highest difference sum of squares the centre of mass was determined for the remaining points, then the worst point was reflected to the centre of mass. If the sum of squares is lower in this point, these three points are used. Applying the simplex method the results of the automata can be scaled.

4. Results

The territory under the curve drawn during the DSC measurement equals the total heat absorption or emission of the process. The normalized integral of the DSC peaks may be considered equal to the change in the transformed fraction. The transformed fraction curved (continuous line) can be seen for heating $\alpha \rightarrow \beta$ and $\beta \rightarrow \gamma$ (Figure 13–14) and cooling $\gamma \rightarrow$

β and β → α transformations (Figure 15–16). The process was so fast in all four cases that during fitting the curves at the same time the simplex procedure could not find the proper fitting in a manageable time period. As a result, the four curves were fitted separately. In this case the maximum value of the driving force and the change in the activation energies affect the kinetics calculated by the automata in the same way. The maximum value of the driving force was thus fixed before the fitting after a preliminary calculation. Accordingly, the simplex procedure only determined the activation energy values, the starting temperature and the temperature dependence of the driving force.

Table 2

The results of the cellular automata

	Q_n	Q_g	T_{min}	G_m	k
α → β	125100	20316.1	668.029	60000	0.05
β → γ	188000	18457.4	668.352	95000	0.15
β → α	312000	20962.9	777.048	110000	0.28
γ → β	171000	23491.5	770.171	70000	0.16

The results are shown in Table 2. The fitted curves can be seen on Figure 13–16. In the case of some curves the fitting is evidently not perfect and may diverge from the standard of the array of curves. One reason is in connection with the rate of the processes. It is visible that the transformations take place within a short amount of time which means the automata have to calculate fast processes, the dangers of which affecting the precision of the calculation were covered in an examination of automata stability. Another important factor is the fact that in the case of DSC measurements the integrals of the transformed fraction curve and the peak are not equal, correction has to be made using data based on the equipment and the examined material [10, 11] which was not performed on literary results. Moreover, the change of the grain size affects the calculation as a yet unknown factor. Taking these statements into account however, it is stated that the one-dimensional automata of allotropic transformation can be fitted with the allotropic transformation measurement result of uranium.

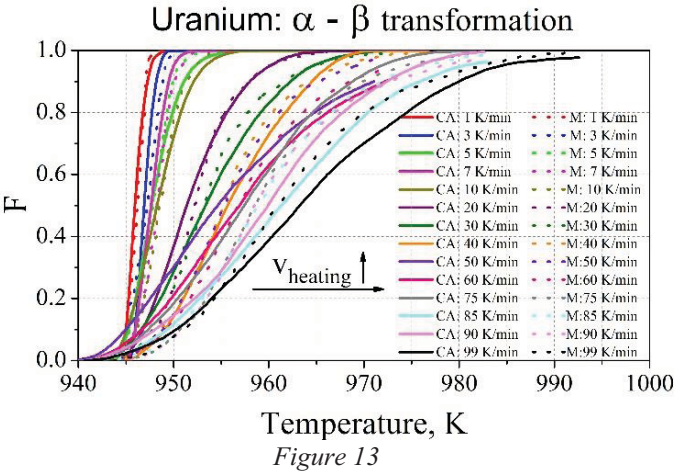

Figure 13

Transformed fraction curves during α → β transformation of uranium in the case of heating and the curves fitted with the simplex procedure by the one-dimensional automata for different heating rates

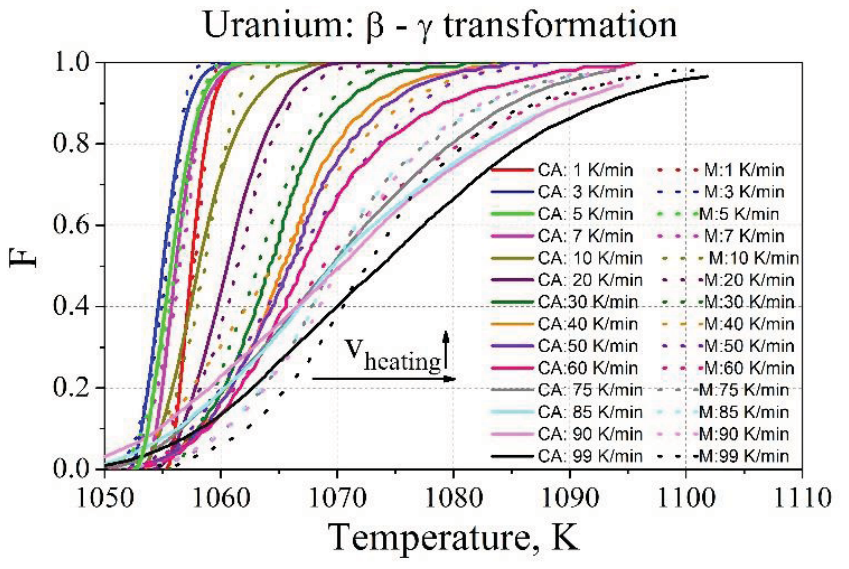

Figure 14

Transformed fraction curves during β → γ transformation of uranium in the case of heating and the curves fitted with the simplex procedure by the one-dimensional automata for different heating rates

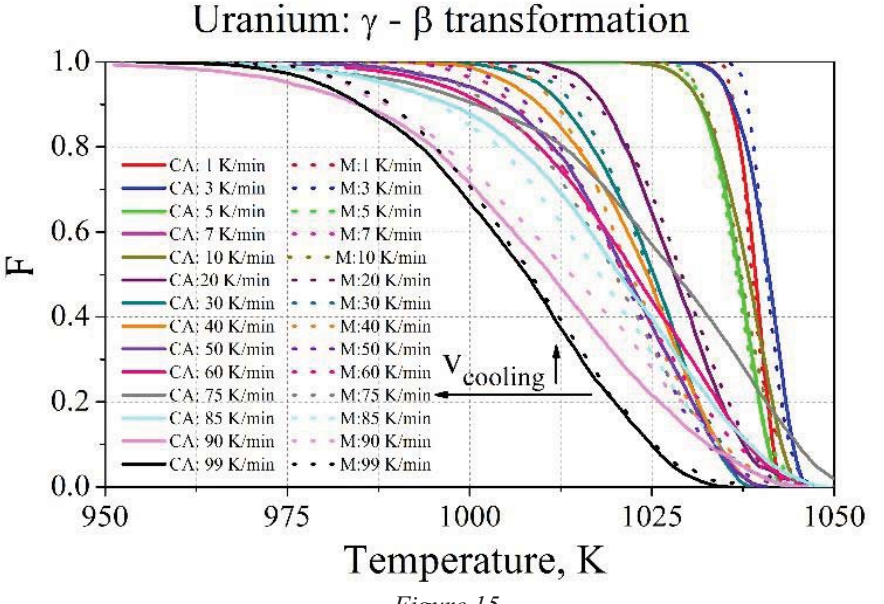

Figure 15

Transformed fraction curves during γ → β transformation of uranium in the case of cooling and the curves fitted with the simplex procedure by the one-dimensional automata for different cooling rates

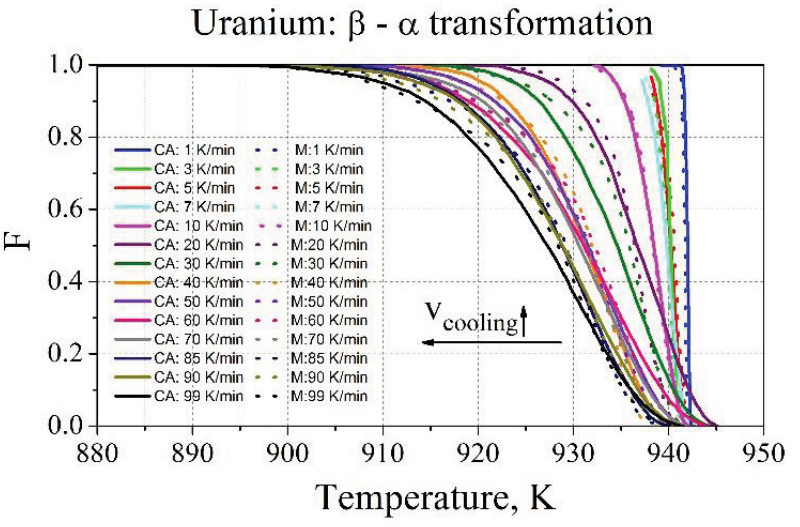

Figure 16
Transformed fraction curves during β → α transformation of uranium in the case of cooling and the curves fitted with the simplex procedure by the one-dimensional automata for different cooling rates

Summary

In this study the simulation model of one-dimensional cellular automata allotropic transformation is presented. Based on the results it is proven that one-dimensional versions of cellular automata are suitable for simulating short-range diffusion as shown in previous publications. Aside from recrystallization and grain coarsening this is also true for allotropic transformation. It is presented through the example of pure iron that the model follows the Avrami-type kinetics. It is also proven that the scaling of the automata can be performed in this case, using literary DSC measurement results of uranium. The validation of one-dimensional cellular automata simulations can be fulfilled for modelling allotropic transformations.

Acknowledgements

This research was (partially) carried out in the framework of the Center of Applied Materials Science and Nano-Technology at the University of Miskolc.

References

[1] BARKÓCZY P.–GYÖNGYÖSI Sz.: *Sejtautomata anyagtudományi alkalmazásai.* Miskolci Egyetem, Miskolc, 2012.
[2] GYÖNGYÖSI Sz.–BARKÓCZY P.–TÓTH A.: Rövid távú diffúziós folyamatok szimulációja sejtautomata módszerrel. *Miskolci Egyetem Közleményei – 2. sorozat. Anyag- és Kohómérnöki Tudományok.* Miskolc, 2010, 17–26.
[3] GYÖNGYÖSI, S.–TÓTH, A.–BARKÓCZY, P.: Simulation of Phase Transformations Driven by Short Range Diffusion by Cellular Automaton. *Materials Science Forum,* 659, 2010, 405–410.
[4] GYÖNGYÖSI, Sz.–BARKÓCZY, P.: Scaling cellular automaton simulations of short range diffusion processes. *Materials Science Forum,* 729, 2013, 150–155.

[5] WOLFRAM, S.: *A New Kind of Science.* 2002.
[6] GYÖNGYÖSI Sz.–BARKÓCZY P.: Szemcsedurvulás szimulációja egydimenziós sejtautomatával. *Miskolci Egyetem Közleményei. Anyagmérnöki Tudományok,* Vol. 38, No. 1 (2013), 103–111.
[7] GYÖNGYÖSI Sz.–BARKÓCZY P.–HLAVÁCS A.: Egydimenziós sejtautomata skálázása. *MicroCAD 2012, D Section: Applied Materials Science and Nanotechnology Symposium,* 2012, D201–D206.
[8] DAVIES, C. H. J.: *Scripta Metall,* Vol. 36, No. 1 (1997), 35–40.
[9] RAI, A. K–RAJU, S.–JEYAGANESH, B.–MOHANDAS, E.–SUDHA, R.–GANESAN, V.: Effect of heating and cooling rate on the kinetics of allotropic phase changes in uranium: A differential scanning calorimetry study. *Journal of Nuclear Materials,* 383, 2009, 215–225.
[10] BENKE, M.–TRANTA, F.–BARKÓCZY, P.–MERTINGER, V.–DARÓCZI, L.: Effect of heat-flux on the differential scanning calorimetry curve of a thermoelastic martensitic transformation. *Materials Science and Engineer A,* 481–482, 2008, 522–525.
[11] BENKE, M.–MERTINGER, V.–TRANTA, F.–BARKÓCZY, P.–DARÓCZI, L.: Supplement on "Effect of heat-flux features on the differential scanning calorimetry curve of a thermoelastic martensitic transformation". *Material Science and Engineering A,* 527, 2010, 2441–2443.
[12] OKAMOTO, H. J.: *Phase Eq,* 13 (1992), 109.
[13] LAGARIAS, J. C.–REEDS, J. A.–WRIGHT M. H.–WRIGHT, P. E.: Convergence Properties of the Nelder-Mead Simplex Method in Low Dimensions. *SIAM Journal on Optimization,* Vol. 9, No. 1 (1998), 112–147.
[14] POWELL, M. J. D.: Direct search algorithms for optimization calculations. *Acta Numerica,* Vol. 7 (1998), 287–336.
[15] GAO, F.–HAN, L.: Implementing the Nelder–Mead Simplex algorithm with adaptive parameter. *Comput. Optim. Appl,* 2010.
[16] PALÁNCZ B.: *Numerikus módszerek.* Budapesti Műszaki és Gazdaságtudományi Egyetem. Fotogrammetria és Térinformatika Tanszék, Budapest, 2010.
[17] BABARCZY M.: *Nelder–Mead algoritmus és variánsainak alkalmazása, tesztelése.* Eötvös Lóránd Tudományegyetem. Operációkutatási Tanszék, Budapest, 2013.
[18] VAUGOYEA, H.–LOMBARD, L.–MORLEVAT, J. P.: A Contribution to the Study of the Uranium-Silicon Equlibrium Diagram. *Journal of Nuclear Materials,* Vol. 39, No. 3 (1971), 3223–3229.
[19] DOMAGAAL, R. F.: *Phases in U-Si Alloys.* Materials and Components Technology Division. Argonne National Laboratory,1986.
[20] KAUFMANN, A.–CULLITY, B.–BITSIANES, G.: Uranium-Silicon Alloys. *Journal of Metals,* 1957, 23–27.

Materials Science and Engineering, Volume 41, No. 1 (2016) pp. 51–61.

SYNTHESIS AND INDUSTRIAL APPLICATION OF AMINOPYRIMIDINES

ANETT JUHÁSZ[1]–ATTILA TIMKÓ[2]–RENÁTA ZSANETT BOROS[3]

The aim of this research was to synthetize 2-amino-4,6-dimethoxypyrimidine (ADMP) derivatives with different methods in order to optimize their yields. The 2-amino-4,6-dihydroxypyrimidine (ADHP) was obtained at yield of > 90% by a ring closing reaction. The hydroxyl groups of ADHP were changed with chlorines to form the product. In this case the highest yield was reached with use of the acid-trapping agent, N,N-diethyl-aniline. Finally, the methoxy groups were built up by alkaline methanolic heating. The 2-amino-4,6-dimethoxypyrimidine (ADMP) was phosgenated expecting to get the 2-amino-4,6-dichloroypyrimidines (ADCP).
Optimization of the 2-amino-4-chloro-6-methoxypyrimidine (ACMP) synthesis was also carried out. The purest product was obtained with the use of the 1.1 equivalent alkaline which was added in three portions within 3 hours according to the GC-MS measurements. Since the yield of this reaction was only 48% further optimization of the reaction conditions is required.
Keywords: pesticides, amino-pyrimidine, phosgenation, synthesis

Introduction

Pest management has been playing an extremely important role in agriculture since Ancient Sumerians who used sulfur compounds to kill insects [1]. However, pesticides may be dangerous due to the accumulation of the harmful pesticide residues in the plant products, the resistance ability against the agents and the mass death of the useful pollinator inspects [2], just to name a few.

Because of the elimination of these problems and the growing requires of the market, continuous active development needs to be carried out. The sulphonyl-carbamides are one of the most modern groups of herbicides. It is considerable that their applied dosages are much smaller than the amount of pesticides which have been used so far. They can be fed in gram/hectare amount. Therefore, their application causes fewer loads for the soil [3].

At KISCHEMICALS LLC. a research and development work is carrying out for synthetizing sulfonyl-carbamide agents which raw materials are the amino-pyrimidines.

Beside the products the base material production is also going to be executed by the company so that is why it is very important to find out and deeply examine these compounds.

Several methods are known for synthetizing amino-pyrimidines [4]. 2-amino-4, 6-dimethoxypyrimidine can be synthetized from 2-amino-4, 6-dihidroxypyrimidine (ADHP) *via* a catalysed phase transfer reaction [5]. Tetrabutylamonium bromide (TBAB) can be

[1] BorsodChem Zrt., Bolyai tér 1.
H-3700 Kazincbarcika
anett.juhasz@borsodchem.eu
[2] KISCHEMICALS – Manufacturing & Mercantile LLC.
H-3792 Sajóbábony
timko.attila@kischemicals.hu
[3] BorsodChem Zrt., Bolyai tér 1.
H-3700 Kazincbarcika
renata.boros@borsodchem.eu

used as phase-transfer catalyst, while dimethyl-carbonate (DMC) is used as methylation agent [5].

The reaction has a good conversion harmful by-products are not generated. In the view of green-chemistry this is a favourable synthesis pathway. Because this is new result it has never been applied in this research work [5].

1. Experiment

The heterocycle was synthetized first by a ring closing reaction, then the required functional group was built up on the ring. The synthesis of the 2-amino-4,6-dihydroxypyrimidine (ADHP, Figure 1) was from the reaction of guanidine and diethyl malonate.

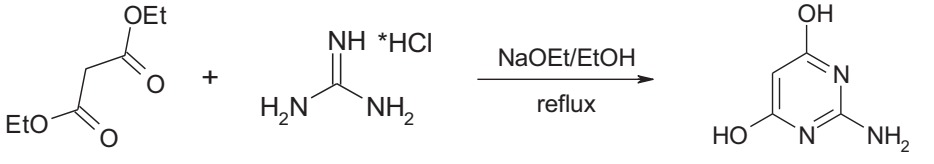

Figure 1
Synthesis of 2-amino-4,6-dihydroxypyrimidine (ADHP)

The synthesis of the 2-amino-4,6-dimethoxypyrimidine (ADMP, Figure 3), was attempted either directly from ADHP or *via* intermediate such as 2-amino-4,6-dichloropyrimidine (ADCP, Figure 2).

Figure 2
Formation of 2-amino-4,6-dichloropyrimidine (ADCP) using phosphorous-oxychloride

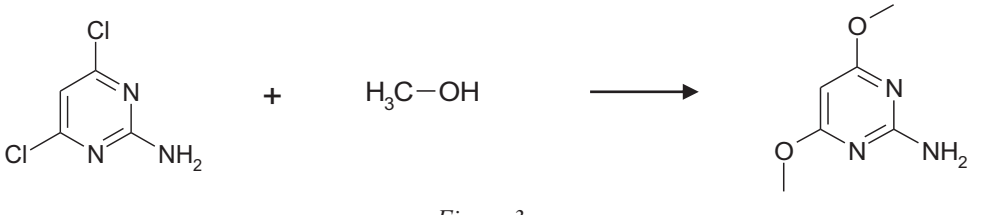

Figure 3
Formation of 2-amino-4,6-dimethoxypyrimidine (ADMP) from ADCP and ethanol

Transformation of ADHP to ADCP was also studied here using both phosphorus-oxochloride ($POCl_3$) and phosgene ($COCl_2$) reagents. The synthesis of the other possible intermediate, ACMP, was also our intent, so the reaction of ADCP with methanolic NaOH solution was investigated, although the dichloropyrimidine (ADCP) was the raw material in this case.

1.1. General experimental section

The melting points were measured with Büchi B-540 instrument. The GC-MS measurements were carried out with Agilent 7890 A gas chromatograph, used with 5979 C mass spectroscopy. The IR analysis was achieved by Bruker Alpha FT-IR spectrometer.

1.2. Detailed experimental section

1.2.1. Synthesis of 2-amino-4,6-dihydroxypyrimidine

Guanidine solution was prepared by dissolving sodium (12 g, 0.52 mol) in 300 cm^3 of ethanol and then 48 g of guanidine-hydrochloride (40.50 mol) was added to it and the solution was filtrated.

23 g of sodium (1.0 mol) was dissolved in 500 cm^3 of ethanol in order to prepare sodium ethoxide solution. Then diethyl malonate (80 g, 0.50 mol) and the previously prepared guanidine solution were added room temperature. The reaction mixture was stirred for an hour under reflux temperature. After it was evaporated to dryness and taken up with water and the pH was adjusted to 6 with acetic acid. The precipitate was filtered and then was washed with ethanol and ether. Finally, it was dried at 60 °C under vacuum [6]. The product could not be examined with GC-MS, because it is hardly soluble to organic solvents used for the GC-MS analysis. Therefore, IR spectra of the product was recorded and compared with the results of the detailed experimental and theoretical investigation of ADHP published in Ref. [7] Melting point: > 300. The colour of it was pinkie white.

1.2.2. Synthesis of 2-amino-4,6-dichloropyrimidine (ADCP) from ADHP

Method A

ADHP (25.4 g, 0.2 mol) was added to the 100 cm^3 (1.12 mol) phosphorus-oxochloride ($POCl_3$) at room temperature and it was stirring for an hour at 75 °C. Triethylamine (TEA, 46 g, 0.45 mol) as acid adhesive agent was added dropwise to this solution.

The redundant phosphorus-oxochloride was evaporated under vacuum. The lowest temperature in the reaction vessel needed to be 75 °C because of its boiling point.

The residue was mixed with water and stirred for 2 hours at 50 °C. The pH was adjusted to 3 with the use of 20 w/w% of NaOH solution. The product was filtrated, washed with water and dried in air [8]. Melting point: 218–220 °C. The colour of it was yellow-reddish.

Method B

In the phosgenation reaction 200 cm^3 chlorobenzene was added to the ADHP (10 g, 0.08 mol). Phosgene was fed continuously to the reaction mixture under the liquid level at 100 °C. After two hours the redundant phosgene was eliminated with nitrogen for about 30 minutes. The phosgene elimination process went on until the phosgene content was 0%. The phosgene content was monitored by classic titration method. 20.24 g trimethylamine (0.2 mol) was added to the system at 30 °C, then the temperature was increased to 75 °C during the feed. The chlorobenzene was distilled by rotation vacuum evaporator. The achieved product was dried in air. Melting point is unknown. The colour of it was red and brown. Probably not the required product was formed so the yield of it was not determined.

1.2.3. Optimization of the synthesis of 2-amino-4,6-dimethoxypyrimidine (ADMP) from ADCP

NaOH (16.1 g, 0.366 mol) was added in small doses to 300 cm^3 of methanol at room temperature. After an hour of stirring, 20 g of ADCP (0.122 mol) was introduced to the reac-

tion mixture and was heated up to 75 °C for 5, 4 and 3 hours. The methanol was evaporated. The residue was cooled down and filtered off [9]. Melting point: 94–97 °C. The colour of it was light yellow.

1.2.4. Optimization of the synthesis of 2-amino-4-chlorine-6-methoxypyrimidine (ACMP) from ADHP

To 100 cm^3 of methanol is added 6 g of ADHP (0.048 mol). Given amounts of methanolic NaOH solution was added to it (Table 2). After 30 minutes the first part of NaOH solution (33.33 cm^3) was added to the solution then in each hour the residue of the alkaline (66.66 cm^3) in two parts. The compound was stirred for an hour after the 100 cm^3 of alkaline had been added.

After all, the methanol was evaporated with means of a rotation vacuum evaporator. The dry compound was washed with water, filtrated and then dried in air. Melting point is unknown. The colour of it was white.

2. Results

2.1. Synthesis of 2-amino-4,6-dihydroxypyrimidine (ADHP)

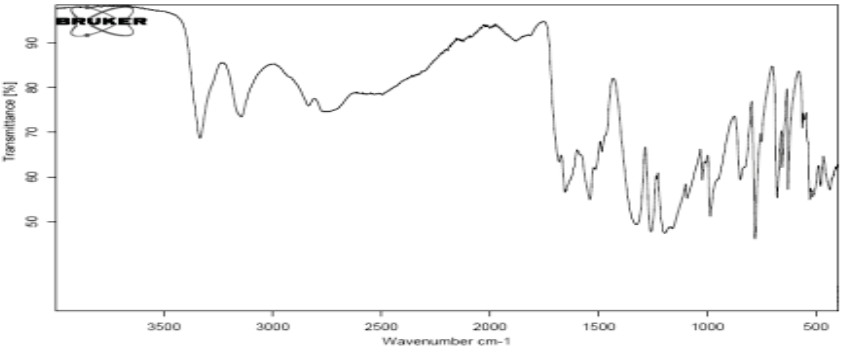

Functional group	Wavelength (cm^{-1})
O-H	3330
N-H	3140
C-H (ar)	2700–2800
C-C (ar)	1550
C-N	1350

Figure 4
IR spectrum of 2-amino-4,6-dihydroxypyrimidine (ADHP) and the bands of the relevant functional groups

Guanidine hydrochloride was added to freshly made sodium ethylate solutions. In this endothermic reaction white sedimentation, sodium chloride, was formed, which was then filtrated. Diethyl malonate was added to another portion of fresh sodium ethylate solution and then it was mixed with the colourless filtrate previously made. After the mixing, high viscosity solution with white precipitate was formed, which was difficult to stir. After 15–20 minutes it became clear. This stirring problem was prevented in the next experiments

because the diethyl malonate and the sodium ethylate were previously stirred for 20 minutes during which the white sedimentation was precipitated from the system. After that the filtrate of the guanidine base was added dropwise in 30 minutes. Then it was heated for 1–1.5 hours under reflux. To adjust the pH to 6 acetic acid and hydrochloric acid were used. The formed sediment was difficult to filtrate, therefore the loss of it was high. To overcome on this issue, the filtrated material was washed out with 200 cm^3 of acetone and the mixture of the combined filtrates was heated up to the boiling point. From the cooled solution, additional amounts of ADHP was crystalized. To make our further experiments simple, the acetone was added to the pH 6 solution and then formed pinkie white crystals were easy to filtrate. Yield of the reaction was 95%.

2.2. Synthesis of 2-amino-4,6-dichloropyrimidine (ADCP)

ADHP was added to the $POCl_3$. The $POCl_3$ was a reagent and a solvent at the same time. Triethylamine (TEA) was used as an acid-trapping agent which was fed into the solution within an hour. Firstly, reddish sediment was precipitated then partially was dissolved.

In the first experiment more precipitate was dissolved while less in the second run, which can be the reason for lower yield in the second case (Table 1).

Table 1
Results of the reaction (ADCP)

Entry	Conditions (acid trapping agent)	Yield (%)
1.	Triethylamine	87
2.	Triethylamine	61
3.	N,N-diethyl-aniline	96
4.	N,N-diethyl-aniline	98

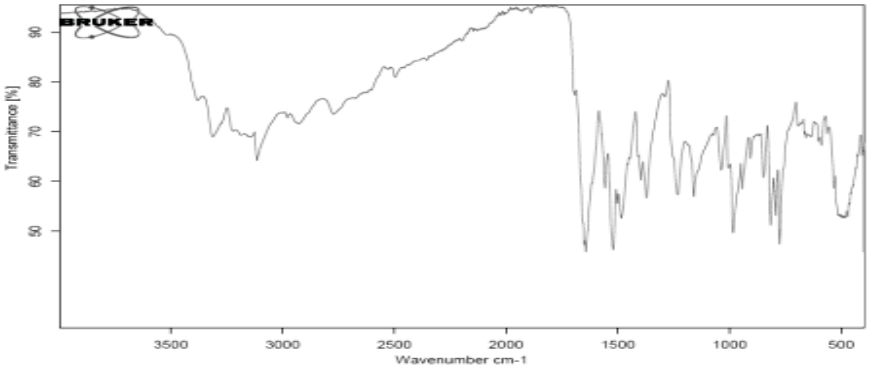

Functional group	Wave number (cm^{-1})
N-H	3315
C-H (ar)	3100
C-C (ar)	1520
C-N	1410
C-Cl	770–820

Figure 5
IR spectrum of 2-amino-4,6-dichloropyrimidine (ADCP) and the bands of the relevant functional groups

In order to avoid the precipitation, the acid-trapping agent was introduced below the liquid level which caused higher yield. In the fourth experiment, N,N-diethyl-aniline was used as an acid-trapping agent. Here, sedimentation was not observed and the highest yield of a yellow-reddish ADCP was achieved.

The GC-MS spectrum of the product can be seen on Figure 5. The molecule ion peak can be found at 163.9 m/z, while the base peak is at 128 m/z. Chlorine losing process could be concluded from the difference of these two peaks and then the second chlorine was split off at 92 m/z.

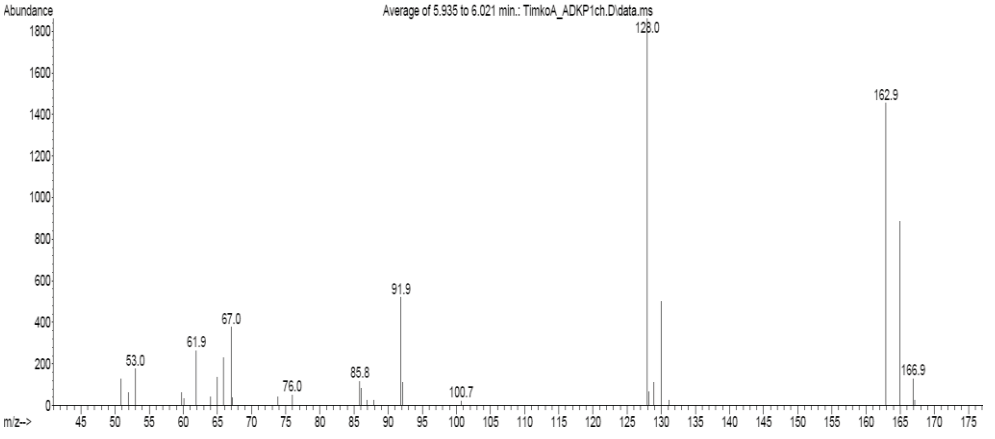

Figure 6
Mass spectrum of 2-amino-4,6-dichloropyrimidine (ADCP)

Table 2
Retention time of GC-MS analysis

Compound name	Molecule mass (g/mol)	Retention time (min)
2-amino-4,6-dichloropyrimidine (ADCP)	163.99	5.951

According to our assumption when the 2-amino-4,6-dihydroxypyrimidine (ADHP) occurs in its another tautomer form (Figure 7) the following reaction (Figure 8) takes place in which the hydroxyl group of the 2-amino-4,6-dihydroxypyrimidine (ADHP) can be substituted by chlorines with phosgenation.

Figure 7
The tautomer forms of 2-amino-4,6-dihydroxypyrimidine

It is known that the chloroformiates can lose carbon dioxide in the present of alkaline catalyst resulted in 6-chloro-2-imino-2,3-dihydropyrimidin-4(1H)-one.

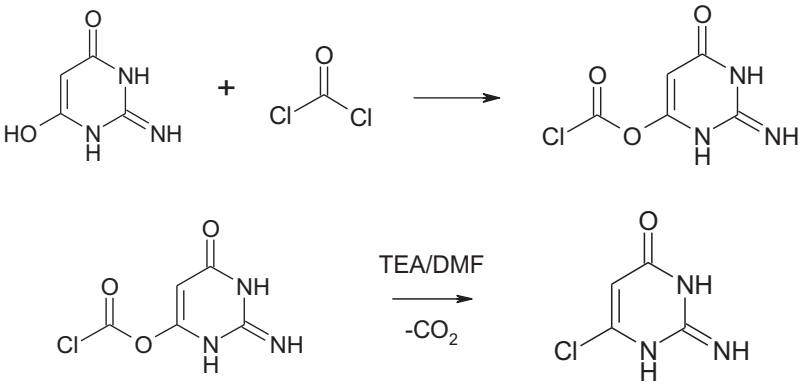

Figure 8
Reaction of 2-amino-4,6-dihydroxypyrimidine (ADHP) with phosgene

In the first reaction the phosgenation occurred in chlorobenzene solvent at 100 °C. The phosgene was added continuously in 2 hours with an intensive flowrate during which different gradients were observed. But in the end of the dosage the solution became clear. The residual solid phase became red. The unreacted phosgene was eliminated with nitrogen gas. For decomposition of the assumed chloroformiate triethylamine was added to the solution at 30 °C and then it was heated at reflux temperature (75 °C). In the second and third reaction dimethylformamide (DMF) was also added to the reaction mixture instead of the triethylamine in different mole ratios. The time of the phosgene was introduced within three hours. In the fourth reaction tetrahydrofuran (THF) was used as a solvent. The phosgene feed was continuously with intensive bubbling during two hours. After that the given product was tried to convert into the required product but not the expected reaction occurred.

Because of the 2-amino-4,6-dihydroxypyrimidine's keto-enol tautorism property probably the phosgene was reacted with the nitrogen atom of the amino group instead of the oxygen atom or the generated carbamoyl-chloride was further reacted with the raw material during which dimer or polymer compounds were formed.

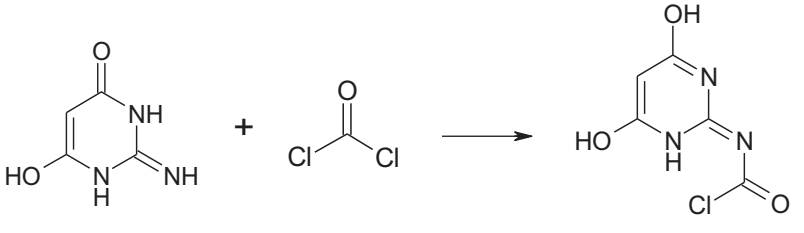

Figure 9
One of the possible side reactions of 2-amino-4,6-dihydroxypyrimidine's tautomer with phosgene

2.3. Synthesis of 2-amino-4,6-dimethoxypyirimidine

The NaOH was dissolved in small portions in methanol and then the 2-amino-4,6-dichloropyrimidine (ADCP) was added to it. In the first experiment it was heated for 5 hours, in the second for 4 hours and in the third for 3 hours at reflux temperature. After that

the redundant methanol was evaporated with distillation. Then the reaction product was cooled down and filtrated with 100 cm^3 of water. Light yellow product was formed.

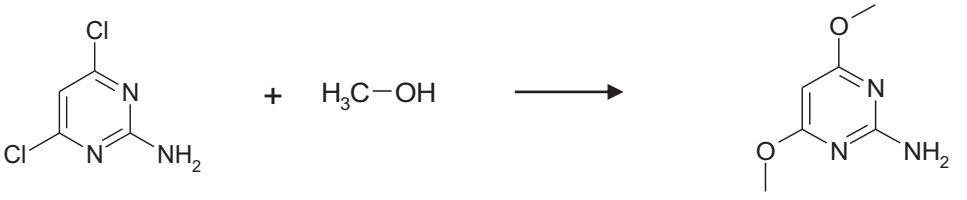

Figure 10
Formation of 2-amino-4,6-dimethoxypyrimidine (ADMP) from ADCP and ethanol

Table 3
Results of the reaction (ADMP)

Entry	Conditions	Yield (%)
1.	5 hours stirring	93
2.	4 hours stirring	75
3.	3 hours stirring	66

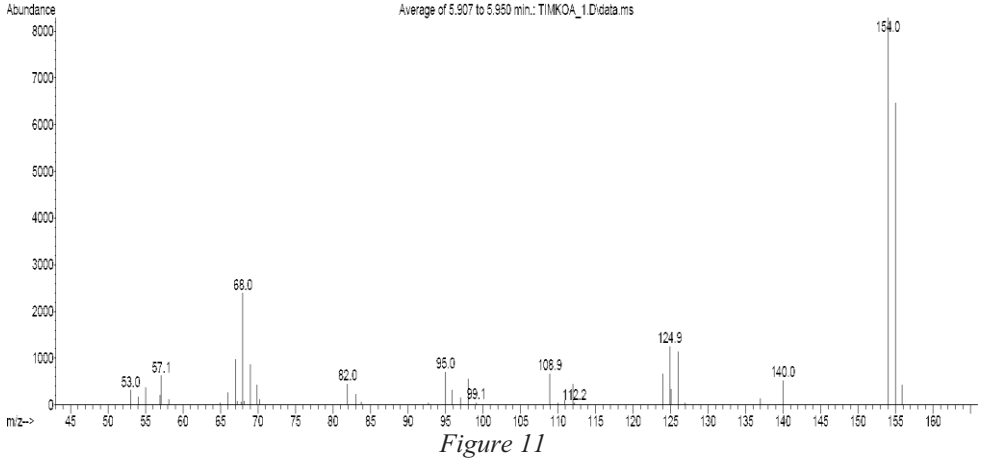

Figure 11
Mass spectrum of 2-amino-4,6-dimethoxypyrimidine

Table 4
Retention time of 2-amino-4,6-dimethoxypyrimidines arising from the GC-MS analysis

Compound name	Molecule mass (g/mol)	Retention time (min)
2-amino-4,6-dimethoxypyrimidine (ADMP)	155.16	5.930

The GC-MS spectrum of the product can be seen in the attachment 2 the molecule ion peak can be found at 155 m/z value. The base peak is at 154 m/z. The split off the two methylene groups occurred at 140 and 124.9 m/z values.

2.4. Synthesis of 2-amino-4-chloro-6-methoxypyrimidine (ACMP)

Several equivalent amounts (1.0, 1.1 and 3.0) of NaOH was added to the methanolic 2-amino-4,6-dichloropyrimidine (ADCP) solution and lasted 3 hours. The product was analysed by GC-MS.

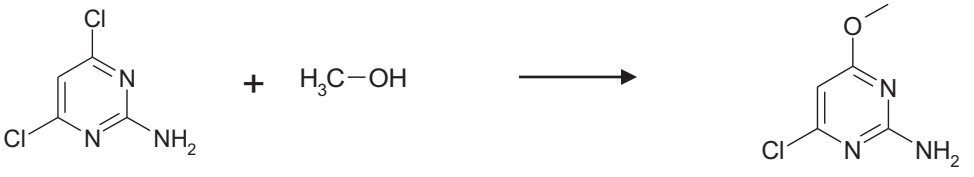

Figure 12
Formation of 2-amino-4-chloro-6-methoxypyrimidine (ACMP) from ADCP and ethanol

The mass spectrum of the 2-amino-4-chloro-6-methoxypyrimidine (ACMP) can be seen on Figure 13. The molecule ion peak occurs at 159 m/z, the base peak is at 158 m/z. There is a methoxy group losing at 129 m/z and a chlorine losing process at 94 m/z.

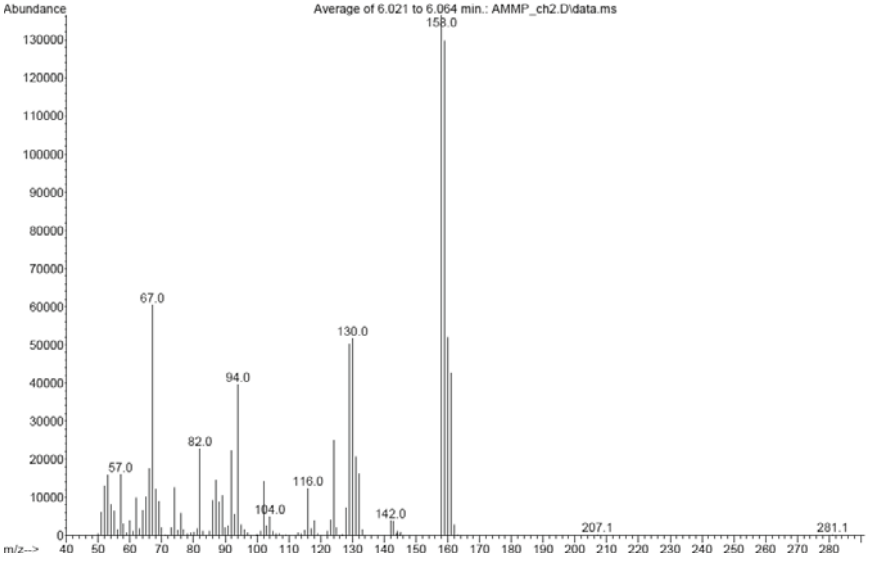

Figure 13
MS spectrum of 2-amino-4-chloro-6-methoxypyrimidine (ACMP)

According to the GC-MS results it could be concluded that when 1 equivalent alkaline was used some initial compound was remained beside the product. In the case of 3 equivalents alkaline the initial compound was further converted, the two chlorine groups were transformed into methoxy groups. Regarding to the mass spectrum and thin layer chromatography the pour 2-amino-chlorine-methoxypyrimidine (ACMP) product was synthetized when 1.1 equivalent alkaline was added to the solution during 3 hours.

Table 5
Obtained GC-MS parameters and yields of the products for synthesis of ACMP by methanolic NaOH solution using several amounts of alkaline

Amount of eq. alkaline	Compound name	Molecule mass (g/mol)	Retention time (min)	Area (%)	Yield (%)
1	2-amino-4,6-dichloropyrimidine (ADCP)	163.99	5.907	23.07	56
	2-amino-4-chloro-6-methoxypyrimidine (ACMP)	159.58	6.045	76.93	
1.1	2-amino-4-chloro-6-methoxypyrimidine (ACMP)	159.58	6.055	99.55	48
3	2-amino-4,6-dimethoxipyrimidine (ADMP)	155.16	5.927	35.19	57
	2-amino-4-chloro-6-methoxipyrimidine (ACMP)	159.58	6.054	64.81	

Summary

The aim of our research works was to synthetize 2-amino-4,6-dimethoxypyrimidine. The initial compound, 2-amino-4, 6-dihydroxypyrimidine (ADHP), was formed via a ring closing reaction. After this reaction step the hydroxyl groups of ADHP were changed into chlorine groups with phosphorus oxychloride and then these groups were converted into methoxy groups with the use of methanol. In the first substitution reaction, 2-amino-4,6-dichloropyrimidine (ADCP) was formed. The best yield was achieved with the change of the acid-trapping agent from trimethyl amine (TEA) to N,N-diethyl-aniline. When triethylamine was added under the liquid level the yield was 96%, while with the use of N,N-diethyl-aniline it was 99%.

In the case of 2-amino-4,6-dimethoxypyrimidine the best obtained yield was 93.5%. In the case of this experiment it was observed that longer the heating period under reflux temperature higher the yield was. The amount of the alkaline might also had an influential role on the yield. It was also attempted to react phosgene with 2-amino-4,6-dihydroxypyrimidine (ADHP) in order to form 2-amino-4,6-dichloropyrimidine (ADCP). The given product was further reacted.

After an alkaline methanolic heating it was analysed by mass spectrometry. According to the MS results it was concluded that only side reaction occurred.

Another aim was to synthetize the 2-amino-4-chloro-6 methoxypyrimidine (ACMP) intermediate. Regarding to the MS analysis the purest product was generated by the use of 1.1 equivalent alkaline, which was added within 3 hours in three parts, but the yield was only 48%. This reaction needs to be further examined [10].

References

[1] PESHIN, R.: Economic Benefits of Pest Management. In: *Encyclopedia of Pest Management, Marcel Dekker.* 2002, 224–227.

[2] TERÉNYI, S.–JOSEPOVITS, Gy.–MATOLCSY, Gy.: *Pesticides Chemistry.* Academic Publisher, 1967.

[3] SZENTEY, L.: Herbicides of sulfonyl-carbamides. *Agroforum: monthly paper of herbicides and plant growers,* No. 40 (2011), 53.
[4] JUHÁSZ, A.: *Synthetis and industrial application of amino-pyrimidines.* Diploma work. University of Debrecen, 2013, 16–18.
[5] XIONG, Z.–ZHOU, M.–XIAO, G.: Synthesis of 2-amino-4,6-dimethoxypyrimidine with dimethyl carbonate as methylating agent. *Research on Chemical Intermediates,* Vol. 40, Issue 5 (2014), 1789–1797.
[6] DUNN, Danny L.–SKINNER, Charles G.: Pyrimido [4,5-b][1,4]oxazines, 8-Ocadihydropteridines. *J. Org. Chem*, Vol. 40 (1975), 3715.
[7] KRISHNAKUMAR, V.–PRABAVATHI, N.: DFT simulations and vibrational analysis of FTIR and FT-Raman spectra of 2-amino-4,6-dihydroxypyrimidine. *Journal of Raman Spectroscopy,* Vol. 39, Issue 5 (2008), 679–680.
[8] United States Patent. 5,563,270, (1995) 25.
[9] AKHMETOVA, A. G.–LIKHACHEVA, V. M.: Improvement of the process of obtaining 4-amino-2,6-dimethoxypyrimidine in the manufacture of sulfadimethoxyne. *Pharmaceutical Chemistry Journal*, Vol. 6, Issue 12 (1972), 788.
[10] JUHÁSZ, A.: *Synthetis and industrial application of amino-pyrimidines.* Diploma work. University of Debrecen, 2013.

Materials Science and Engineering, Volume 41, No. 1 (2016) pp. 62–68.

APPLICATION OF A SIMULATION MODEL TO AN INDUSTRIAL ETHANE-CRACKING FURNACE OPERATION

JÁNOS KEREZSI[1]

Computer simulation of an ethane furnace in the olefin production is presented. It is focused on the application of modelling programs for the simulation of multistage chemical technology processes. The submitted strategy allows the modelling of homogeneous and heterogeneous processes in reactors of any complexity on basis of experimental data processing. The simulation of reactor processes has been performed with the use of the CHEMCAD program for the ethane thermal cracking. The main products of Steam Cracking Olefin production technology are the ethylene and propylene. It is necessary to use an appropriate kinetic model for the simulations, because it determines the results of the simulation. Choice of the mathematical theory is also important, since it determines the number of the iterations and the running time of the simulations. The chosen model has to harmonise with the pyrolysis simulation and in order to get accurate results and it is also necessary to consider each radical reaction.
Keywords: Chemcad, computer simulation, ethane pyrolysis, olefin production, optimization, thermal cracking

Introduction

At present, chemical engineers are showing great interest in development of computer models for reactor processes and their application for the simulation and optimization in industrial level. The modern approach to the creation of resource-saving technologies assumes the application of suitable software to simulate complete multistage industrial systems, in particular, reactor processes. The thermal decomposition of ethane takes place at 830–860 °C temperature in a pyrolysis furnace. From kinetic aspect, this reactor can be considered as a plug-flow reactor. This kind of kinetic reactor has been chosen from ChemCad list for modelling of the furnace [1]. Application of modelling programs for the purpose of their inclusion in models of complete industrial system imposes certain requirements on their procedure. In case we want to modify some parameters of technology, than we can do it in a simulation program.

1. Ethane cracking simulation

1.1. Mathematical model of the simulation

According to this, the strategy of simulation of reactor processes with the application of modelling programs in the construction of computer models for complete flow sheets of industrial chemical processes consists of the following:
(1) stoichiometric data are specified for each reaction;
(2) key component conversions in the reactions, which can be determined from experimental data, are specified for each reaction; and
(3) the reactor process is calculated with determination of the flow rate, composition, temperature and other characteristics of an outlet stream, as well as the required flow rate for a heating (or cooling) agent, if it is necessary to supply/remove heat etc. [1].

This is the way of solving the direct problem of computer modelling for reactor processes. Chemical engineers from petroleum companies widely use cubic equations of state (EoS) and

[1] University of Miskolc
kerezsi@gmail.com

especially the ones proposed by Peng and Robinson (Peng–Robinson EoS noted PR-EoS afterwards) and by Soave (Soave–Redlich–Kwong EoS, noted SRK EoS afterwards) [2]. These state equations directly come from the Van der Waals theory and can be written for a given mixture under the general form (1):

$$P = \frac{RT}{v-b} - \frac{a}{Q(v)} \tag{1}$$

where P is the pressure, T is the absolute temperature and v, the molar volume of the fluid, Q(v) is a second order polynomial in Classical Van der Waals mixing rules are frequently used to relate the a and b parameters of a mixture to the composition and to the a_i and b_i parameters of the pure components i. Parameter a is taken to be a quadratic function of the mole fractions and parameter b is a linear function. The key point when using such cubic EoS to describe complex mixtures like petroleum fluids is to give appropriate values to the binary interaction parameters. The thermodynamic derivative properties are second order derivatives of some thermodynamic potential with respect to other properties that are first-order derivatives with respect to the same potential, e.g. pressure, volume, and enthalpy [2]. The rigorous thermodynamic expressions for thermal expansivity is αP, isothermal compressibility is βT, calorific capacity is C_P, and Joule–Thompson coefficient is μ (2).

$$\begin{aligned}
\alpha_P &= \frac{1}{\rho}\frac{(\partial P/\partial T)_\rho}{(\partial P/\partial \rho)_T} \\
\beta_T &= \frac{1}{(\rho(\partial P/\partial \rho)_T)} \\
C_P &= C_V^R + \frac{T\alpha_P}{\rho}(\partial P/\partial T)_\rho - R + C_P^{id} \\
\mu &= \frac{1}{\rho C_P}(T\alpha_P - 1)
\end{aligned} \tag{2}$$

where $C^R{}_V$ is the residual calorific capacity at constant volume $C^{id}{}_P$ is the ideal gas calorific capacity, and $\rho = P/ZRT$, where ρ is the molar density, Z is the fluid compressibility factor, R is the universal gas constant, P is the absolute pressure, and T is the absolute temperature of the system.

The next step is to find the right mathematical program that can be used for present simulation. The hydrocarbons are in vapour phase in the radiant zone so it is possible to use the Soave–Redlich–Kwong enthalpy model [3]. The model is based on ideal gas law, but it considers the realistic gases as well. The base equations are the followings (3):

$$\begin{aligned}
p &= \frac{RT}{V_m - b} - \frac{a\,\alpha}{V_m\,(V_m + b)} \\
a &= \frac{0.427\,R^2\,T_c^2}{P_c} \\
b &= \frac{0.08664\,R\,T_c}{P_c}
\end{aligned} \tag{3}$$

$$\alpha = \left(1 + \left(0.48508 + 1.55171\,\omega - 0.15613\omega^2\right)\left(1 - T_r^{0.5}\right)\right)^2$$

$$T_r = \frac{T}{T_c}$$

where:

P: partial pressure [Pa]
T: temperature [K]
R: gas constant [kJ/kmol K]
V: volume (l)
ω: kinesics speed
α: factor

1.2. Theoretical considerations

The traditional mathematical modelling technique for reactor processes is based on the application of detailed kinetic models. Kinetic data of many processes may be absent or their kinetics may be studied insufficiently. Moreover, numerical non-convergence may be observed both for a single reactor process and for an entire flow sheet while simulating multistage chemical technology processes with recirculation [4]. One of the raw materials of olefin plants is the recycled ethane. The technology of pyrolysis is based on the thermal cracking of hydrocarbons. The temperature inside the radiant tubes of furnace is between 830–860 °C. The high temperature indicates the high – energy collision and the decomposition of hydrocarbon molecules into radicals. Thermal cracking of ethane in the furnace means a series of complex consecutive and parallel reactions, but the yield of ethylene is more than 40%. The reaction processes is mainly based on radical mechanisms though molecular reactions can also be identified in the system. These mechanisms have three main steps. The first one is the chain-initiation step that includes endothermic reactions, so that need heat to start decomposition. The second group consists of chain-propagation reactions and the last group of reactions is the group of chain-termination reactions that generate new molecules like olefins, paraffins and hydrogen [5]. Reactions in the third group are exothermic that means it is necessary to use cooling. The ethane enters the furnace in 100 mol% after separation and recycling while the cracked gases contain 30–40% ethane, so the pyrolysis per one pass cannot be considered very effective. Chemcad simulator was used for the simulation of ethane cracking in the radiant zone of the furnace. The main objective of the simulation was to optimize the ethane re-pyrolysis cycle.

1.3. Kinetic Model

The first step of ethane thermal pyrolysis simulation is creating the reaction scheme (4–7) [6].

$$M_p - CH_2 - H \longrightarrow M_p - CH_2 \bullet + H \bullet \tag{4}$$

$$M_pCH_2\text{.} + R_1\bullet \rightarrow R_1H + R_3\bullet \tag{5}$$

$$R_3 \rightarrow M_o + R_4\bullet \tag{6}$$

$$R_4\bullet + M_p \rightarrow R_3\bullet + H \tag{7}$$

where:

M_p – paraffin
M_O – olefin
R_1-R_4 – radical molecule
H – hydrogen.

Decomposition of generated radicals is modelled on the basis of steady-state, so all radicals are transformed in each integration step. The most important beta-scission reactions are modelled using temperature dependent selectivity. Beta-scission is divided to scission of C-H and C-C bonds. C-H scission recognizes primary, secondary and tertiary carbon atoms and C-C bonds scissions are divided according to the count of substituents (substituents of the bond).

A mechanistic kinetic model was developed on the basis of a detailed reaction network containing 81 pieces of individual reactions [5], including both radical and molecular ones. Kinetic parameters were assigned to each reaction from published and arranged in the literature data [7, 10]. Validation of the model was performed by comparing its results with those obtained experimentally from cracked gas analysis of an industrially operated furnace, fitting the kinetic parameters to experimentally measured yield data.
The theory of kinetic parameters is based on the Arrhenius equation (8) [7, 10].

$$\ln k = -\frac{E}{RT} + \ln A_0 \tag{8}$$

where:

k: reaction rate constant
T: temperature [K]
R: gas constant [kJ/kmol K]
E: activation energy [kJ/Kmol]
A_0: frequency factor

The radical reactions cannot be shown with "normal" kinetic equations. Experts launched the Severity factor instead, that is a simple method for complex pyrolysis reaction-system, which was introduced by LINDEN and PECK (9) [8]

$$S = t \cdot \tau^{0,06} \tag{9}$$

where:

S: severity of pyrolysis
t: coil outlet temperature [°C]
τ: residence time [sec]

1.4. Modelling

To build-up the furnace model, a simulation program is also needed. According to this, the calculation strategy of reactor processes with the application of modelling to build up computer models for complete flow-sheets of industrial chemical processes as it was described in 2.1. [9].

For nearly 25 years [3] Chemstations Co. and its chemical process simulation software CHEMCAD have been evolving with the highly dynamic chemical engineering industry. The steps to make the ethane cracking simulations in CHEMCAD are as follows:

1. to build the flow sheet, kinetic reactor to define the special molecules (radicals)
2. to choose the right mathematical model
3. to install each parameter of the reactor
4. to run the simulation program
5. to collect the results

First step is to define the reactions. The composition of raw material and the products came from the laboratory data of the measurements. Next step is to determine the type of model. The mechanistic model was chosen for this purpose. Since this model is very complex and it calculates the results through numerical iterations, needs more running time. The next step is to assign kinetic parameters for each reaction. It was very important to take care about the complexity.

1.5. Technology

The ethane and the steam enter the convection zone together and the mixture is heated up by the flue gases, which come from the radiant zone. Outlet temperature of the convection zone is 550–650 °C, where the cracking of some hydrocarbons is already started. The purpose of the water feed is to keep the pressure in the tube and suppress the coke formation. The stream enters the radiation section where the conditions are controlled, such as the temperature, pressure, and residence time. The temperature at the exit of radiation zone achieves 850–860°C. In this zone the hydrocarbons crack and some other kinds of different (shorter) molecules are formed. The hydrocarbon fractions are very diverse from C_1 fraction to C_{10} fraction in case of ethane cracking. The main product of the ethane cracking furnace is the ethylene. The furnace produces approximately 24 vol% ethane. The first period of the reactions is endothermic, so it needs high energy impute. In industrial practice a mixture of methane fraction and natural gas is used for heating. At the end of the radiant zone the reactions became exothermic, so the reaction mixture needs cooling. The cooling method is the quench cooling system that includes a heat-exchanger cooling the "cracked" gases by high-pressure boiler-feed-water (BFW), producing high-pressure steam by using the heat of cracked gases. The gases are further cooled by a direct spray of pyrolysis heavy oil reaching a temperature of 300 °C. Following this, the cracked gases are driven to the gas separation units. The technology parameters have to be set in such a way to obtain the maximum monomer (ethylene, and propylene) production and the minimum yield of methane and heavy hydrocarbons. The constraints of the process (ex. Capacities) as well as the financial aspects have also to be considered. For example it is not profitable to increase the amount of dilution steam, because it needs lot of energy and increases the operational cost.

1.6. Chemcad simulation

Figure 1 shows the furnace scheme in Chemcad software.

The raw materials, steam and ethane enter a theoretical mixer (2), so it is possible to vary the CH/Steam ratio within the specified limits. The heat exchanger (3) symbolizes the convection section. The radiation zone is simulated by the kinetic reactor (1). The controller has the role to keep the integration time. The component separator (5) is a theoretical separation, in order to measure the hydrocarbons and the water separately. The geometry of

the furnace could be set up and the radiation zone has four independent tube sections (the height of tubes is 10 m and the inside diameters of the tubs are 0,108 m and the full length is 70 m). The ethane feed is 10.5t/h, and the steam feed is 4t/h in each tube. The raw material contains 99,96 w% ethane. The ethane and ethylene are the two key components. The theoretical conversion is about 60%. The main purpose of the ethane cracking simulation is to build up the model that can be suitable for modelling the ethane cracking furnace operation. The results of the simulations produced similar data like the real furnace (same operational data, and same stream properties).

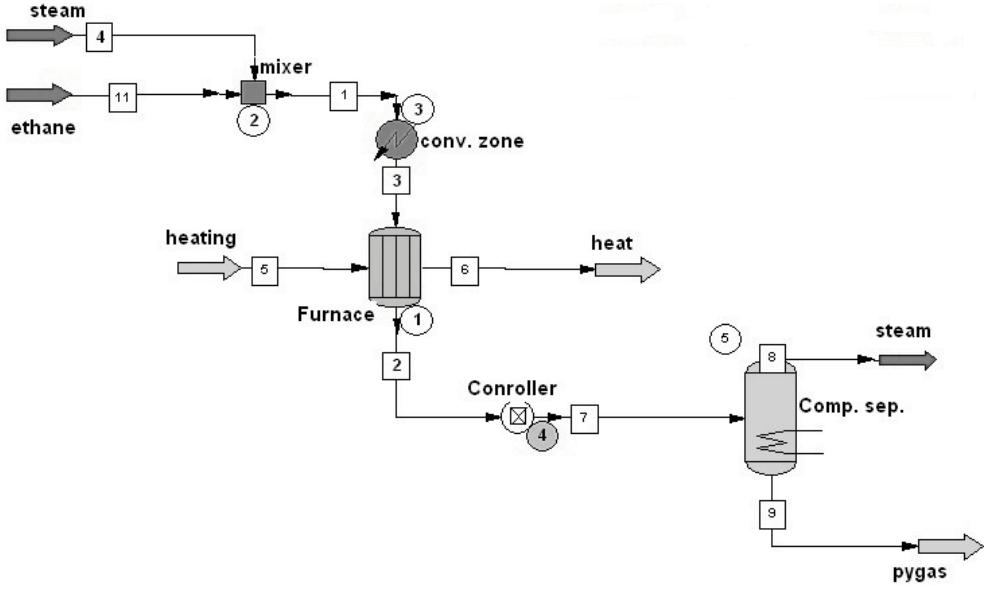

Figure 1
Process flow diagram of the ehtane furnace

Table 1
Cracked gas composition by CHEMCAD and laboratory data

pygas properties	hydrogen (V%)	methane (V%)	ethane (V%)	ethylene (V%)	propane (V%)	propylene (V%)	acetylene (V%)	buta diene (V%)	others (V%)
Chemcad data	35.79	4	24	35	0.04	0.42	0.26	0.49	0
laboratory data	35.36	3.79	24.97	34.35	0.06	0.44	0.3	0.53	0.2

According to the table it can be concluded that the results are similar. The hydrogen, ethane, ethylene, propylene concentrations modelled by CHEMCAD and measured laboratory data are in good harmony with each other.

Conclusions

The main products of the olefin plant are the ethylene and propylene, which are produced by thermal cracking of different hydrocarbons. The ethylene goes to the polymer plants and the ethane is driven to the furnace again for re-pyrolysis. However, there are more furnaces in operation in the olefin plant and each furnace produce ethane, so the ethane-recycle shall be established by the operation of ethane-cracking furnace. The most important task of the optimization is to find the optimum parameters of the ethane cycle, between the ethane – ethylene distillation column and ethane cracking furnace. The ethane cracking furnace is not able to take in all the ethane produced in the furnaces because the inlet feed has a maximum capacity, and the distillation tower has a maximum capacity. It is necessary to find those optimum parameters, by means of which the ethane quantity continuously recycling in the olefin plant system can be reduced. Moreover, the purpose of the simulation is to choose the right mathematical model, because it is necessary to get similar results to the real operational data and yields.

References

[1] TURTON, R.–BAILIE, R. C.–WHITING, W. B.–SHAEWITIZ, J.: *Analysis, synthesis and design of chemical processes.* 2009, 1–200.

[2] GARTMAN, T. N.–SOVETIN, F. S.–NOVIKOVA, D. K.: *Mendeleev Experience in the Application of the CHEMCAD Program.* The Modelling of Reactor Processes University of Chemical Technology of Russia, Moscow, June 02, 2009.

[3] http://www.chemstations.net 2015

[4] SUNDARAM, K. M.–FROMENT, G. F.: Modeling of thermal cracking kinetics. 3. Radical mechanisms for the pyrolysis of simple paraffins, olefins, and their mixtures. *Ind. Eng. Chem. Fundam,* 17 (1978), 174–182.

[5] ALIEVA, A. M.–TAIROVA, A. Z.–GUSEINOVAA, A. M.–ISMAILOVB, N. R.–SHAKHTAKHTINSKIIA, T. N.: Optimum Zoned Fuel Gas Supply to the Coil of an Ethane Pyrolysis Furnace. *Theoretical Foundations of Chemical Engineering,* Vol. 44, No. 6 (2010), 913–919.

[6] BELOHLAV, Z.–FIEDLER, L.: The primary product distribution in naphtha thermal cracking. *Chem. Biochem. Eng. Q,* 10 (1996), 113–117.

[7] DENTE, M.–PIERUCCI, S.–RANZI, F.: New improvements in modelingkinetic schemes for hydrocarbon pyrolysis reactors. *Chem. Eng. Sci,* 47 (1992), 2629–2634.

[8] LINDEN, H. R.–PECK, R. E.: Severity function in pyrolysis. *Ind Eng. Chem,* Vol. 46, No. 12 (1955), 2470–2474.

[9] PECHURO, N. S.–KAPKIN, V. D.–PESIN, Y. O.: *Khimiya i tekhnologiya sinteticheskogo zhidkogo topliva i gaza. Chemistry and Technology of Synthetic Liquid Fuel and Gas*. Khimiya, Moscow, 1986.

[10] GÁL, T.–LAKATOS, B. G.: Industrial scale modeling of a hydrocarbon gas-mixture cracking furnace. *Thermal Engineering,* 2007. doi: 10.1016/

Materials Science and Engineering, Volume 41, No. 1 (2016) pp. 69–78.

HEAVY METAL CONTAMINATED BIOMASS COMBUSTION AS TREATMENT AFTER PHYTOREMEDIATION – A REVIEW

HELGA KOVACS[1]–KATALIN SZEMMELVEISZ[2]

The biomass properties and behaviors are changed in wide range. Technically, the efficiency of biomass combustion depends on fuel composition significantly. The hevy metal contaminated biomass combustion is a special renewable enegy source, because the burning process could cause high environmental risk. The biomass with high heavy metal content are coming from phytoremediation, an environmentl friendly soil remediation technique. Several methods have been developed for the disposal of heavy metal contaminated biomass, for example the liquid extraction, direct disposal, composting or combustion. This review deals with combustion technology as a disposal option of the contaminated biomass, and examines the possibility and circumstances of this process considering environmental aspects. This disposal technique is very complex. If we analyze the economic aspects, we can take notice of the fact, that thanks to this process the energy production is possible. In order to produce energy from the contaminated biomass without environmental pollution, a special technology is required during the disposal (combustion). In case of ordinary biomass combustion, there are several solid and gaseous air pollutants, which have to be considered. If the aim of combustion is disposal, and the fuel is contaminated with heavy metals, certain emissions will probably increase. The problem of volatile and solid heavy metal compounds in flue gas has to be analyzed. The heavy metals and their compounds have various behaviors, thus certain metals are less volatile and concentrate in the ash, and others leave the combustion chamber in a gaseous form. A part of these volatile compounds condensate in the flue gas system, other parts could be detected in solid or gaseous form at the end of the chimney as emission. This is an avoidable environmental pollution. This review deals with the recent reasearches of this comlex topic.

Keywords: heavy metal, combustion, temperature, phytoremediation

Introduction

Heavy metals are naturally presented in the environment and are taken up in small amount by living organisms. As trace elements, they provide essential nutrients for plants and herbivores, while at toxic level; they cause harmful effects to the whole ecosystem.

Excessive heavy metal concentrations are regularly encountered at areas of extensive mining spoil and metal processing (mine tailings, plant sites). In any case, measures should be taken to prevent the spread of pollution and to reduce toxic levels of pollutant concentration – whether apparently detectable or not. For the remediation of misused industrial sites, various recovery techniques are known. Biological treatments include bioaccumulation, which is based on the capacity of plants and microorganisms to absorb and store chemical substances in concentrations higher than typical for the original environmental source (soil). The absorbed chemicals are accumulated in the plant cells and tissues.

By extracting large quantities of toxic contaminants (e.g. lead, cadmium, zinc) from soil and groundwater, certain plant species effectively contribute to the remediation of heavy metal contaminated sites [1]. The metals are soaked up by the roots and transported through conductive tissues to the aboveground plant parts (shoots), yielding easily harvestable

[1] University of Miskolc, Department of Combustion Technology and Energy Affairs
kovacs.helga@uni-miskolc.hu

[2] University of Miskolc, Department of Combustion Technology and Energy Affairs
tuzszemt@uni-miskolc.hu

biomass. This vegetal activity effectively improves soil quality and helps restoring the ecological balance [2].

1. Biomass coming from phytoremediation

The plants accumulate nutrients through roots or leaves, but the primary source is the root system. Several factors affect the nutrient uptake from the soil, for example the temperature, the water content of the soil, the soil texture, and the pH. For plants, the pH 6.5 is beneficial; the natural living condition for them is between pH 4–8. Further factors are the temperature and water supply of the soil [3].

When chemical compositions of different biomass (for dry sample) were compared, the results varied in a small interval. The main chemical elements of biomass are (in decreasing order) C, O, H, N, Ca, K, Si, Mg, Al, S, Fe, P, Cl, Na, Mn and Ti [4].

Not only the heavy metal nutrient deficient could give rise to metabolic confusion in plants, but also the extremely high concentration [5]. The chemical balance in living organisms is a primary criterion for growing and developing. This is the main reason, why soil treatments (for example liming) are often necessary for keeping alive a plant organism [6] [7] [8]. The effect of heavy metal concentration change to the plant growth could be described by a kinetic model. This allows the recognition of a heavy metal contaminated soil-plant system. Researches prove, that the heavy metal accumulation in plants depends not only on the properties of heavy metals and plants, but also on the soil type, and on environmental circumstances [9].

The mobility and solubility of pollutants could be decreased with cement or $Ca(OH)_2$ in a high pH soil environment, but under low pH conditions the mobility of cadmium, cobalt, copper, nickel, lead and zinc increases [10].

The connection between the concentration and the toxicity is different in the case of every nutrient. Some microelements important for the plants (B, Cl, Cu, Fe, Mn, Mo, Ni, Zn) are untoxic in high concentration [11]. In low concentration, other elements, like cadmium, chromium, mercury and lead do not interfere with the plant growth, but in higher concentration, the plant life is risked. It is important to notice, that a certain amount of heavy metals could be piled up in plants without toxicity symptoms (leaf atrophy, plant growth stopping, necrosis). Several researches deal with the effect of heavy metals for plant life, and determine the toxic concentration of heavy metals in plants [12].

During the remediation with phytoextraction, the heavy metal content of soil decreases, thereby the environmental risk caused by the toxic elements is moderated. Through this process, the pollutants are transferred into the plants; this gives rise to another environmental danger. Soil remediation and polluted biomass formation arise simultaneously. The treatment of this contaminated biomass is required. In 2004 a research [13] determined the following disposal options:

- Composting: American researchers have shown the water solubility of bioaccumulated zinc and other metallic components [14], therefore this method is only applicable with strict control requirements. Total heavy metal content should be minimized through mixing the metal-enriched biomass with high proportions of uncontaminated dry matter and other biodegradable substances. The technology requires the close and continuous monitoring of mixture composition. On the other hand, the phytoextracted metals are returned to the soil in small doses to provide for nutrient recovery. Ex-situ composting is proposed as a post-harvest treatment for

biomass by which the disposal of hazardous plant material can be made more effective [15].

- Pyrolysis: Flash pyrolysis can be used for the disposal of heavy metal contaminated biomass [16] [17] [18] [19]. Low-temperature pyrolysis renders liquid fuel, with the metallic substances concentrated in the solid residues and the by-products [18]. Unless it is further processed as recyclables, the produced coke breeze should be treated as hazardous waste.
- Direct disposal: The direct disposal of the harvested biomass waste would cause environmental problems; therefore, it is forbidden [20]. Disposal as hazardous waste is a feasible yet cost-demanding solution, thus, it is less preferred.
- Leaching: this disposal technology is based on the behaviour of soluble metals to percolate from the carrying medium – which is the very property that accounts for the categorization of metal contaminated biomass as hazardous waste. After enrichment, toxic metals are leached with different solvents from the compacted biomass. The leached product (residual biomass matter) can be treated as non-hazardous material [13]. There are viable technologies to recover the metallic components from the leached solution at relatively high costs, though [21]. The leachability (i.e. recovery rate) of toxic metals from biomass is generally determined as a function of time and pH value [22].
- Incineration (smelting): this process is based on the thermal degradation of contaminated woody biomass into manageable volumes of metal-containing ash. By substantially reducing the volume of hazardous waste material, both transport and disposal can be made more cost-effective. Countless descriptions of the technology are known [23], but there is a paucity of data on the efficiency and technical feasibility of the process. Note that the thermal energy obtained from smelting can be utilized for energy purposes, which adds to the benefits of this method.

The incineration of heavy metal contaminated biomass is a promising yet not fully mature technology. Various combustion systems are currently under development for field-scale application. In the near future, this method is likely to mean an environmentally sound and economically acceptable alternative [13].

Disposal through incineration is an excellent option to replace the expensive treatment and costly transportation of the harvested biomass to hazardous waste disposal facilities. In this way, up to 99% volume reduction of the contaminated material can be reached, with the pollutants concentrated in the solid combustion residues (ash, fly ash). The final product is easy to mobilize and handle in a controlled, environmentally acceptable manner.

2. Heavy metal contaminated biomass combustion

2.1. Heavy metal behaviors and emissions during biomass combustion

During the combustion of heavy metal contaminated biomass, there are not only regular emissions (CO, NO_x, fly ash), but also the problem of the solid and gaseous metal compounds. It would be important to examine these compounds by combustion of ordinary biomass fuels, because certain researches prove, that the heavy metal emission could cause environmental problems, even if the biomass is coming from a non-polluted area [24] [25].

One of the basic sources of danger is the solubility of heavy metals, which are enriched in the bottom ash after combustion. These leaching behaviors determine the disposal options of ash. The leached heavy metals cause environmental damages in waste yards [26] [27].

Another basic source of danger is, that the heavy metal compounds are volatile at the combustion temperature [28] [29]. During the flue gas flowing across the offtake system, the temperature decreases, and the toxic compounds condensate to the solid parts in its environment [30]. The heavy metal compounds have two types at the end of the chimney (depending on the temperature):

- solid (condensed) form, as fly ash; and
- volatile form.

Along with the increasing flue gas temperature, the gaseous-solid transition (particle formation) is controlled by two mechanisms [31] [32]:

- homogeneous condensation, where new particles are formed; and
- heterogeneous condensation, which takes place on the surface of particles

As soon as the metal vapors reach the super-saturation condition, the condensation begins and it contributes to the formation of ulta-fine particles [33].

The researches in the topic of examining biomass burning remains deal with ash analysis primarily [34] [35]. The expansion of this research topic includes the heavy metal examinations inside the biomass combustion system. The distribution of heavy metals in solid and gaseous burning residues is referred to as partition of metals [36].

The main goal is to treat and dispose of the biomass formed in contaminated lands, thus the accumulation of the contaminants could be considered as an aim. The biggest problem is the volatility of these elements. The material flows of the pollutants are required to know.

In the case of fluid bed combustion, the heavy metals (Cd, Pb, Zn) from the biomass are in volatile form at the temperature of the combustion chamber [37]. These compounds condensate at different temperatures, thus the examination of the volatility behaviors should be considered [38]. After the flue gas cools down (180–200 °C), the heavy metals are detected primarily in solid form, except As, Co and Sb, these could stay in gaseous phase [30]. Table 3 shows the volatility of heavy metals at 1 Pa pressure based on thermochemical calculations (with and without chlorides in the burning system) [36].

Table 1

Volatility temperatures and chemical formulae of metals at 1 Pa operating pressure (Randall Seeker, 1991)

Heavy Metal	No chlorides		With 10% of chlorides	
	Volatility temperature (°C)	Form	Volatility temperature (°C)	Form
Cr	1613	CrO_2/CrO_3	1610	CrO_2/CrO_3
Ni	1210	$Ni(OH)_2$	693	$NiCl_2$
Pb	627	Pb	−15	$PbCl_4$
Cd	214	Cd	214	Cd

It can be stated based on Table 1, that several metals (Pb, Cd) are volatile at the biomass burning temperature, especially the chlorides [36].

The release of metals depends on many factors, including the volatility, the burning environment and the ash, fly ash treatment [39]. Furthermore, the amount of metals in flue gas depends on the presence of different types of chlorine-, sulfide-, carbon-, nitrogen- and other compounds in the combustion chamber and flue gas. Fly ash samples coming from municipal solid waste burners were analyzed by X-ray scattering technique, and the results

show that the following compounds were detectable in flue gas at 420 °C (the burning temperature was 953 °C).

- oxides: Al_2O_3, MnO, Pb_3SiO_5, $Pb_3Sb_2O_7$, $PbSiO_4$, Fe_3O_4, Fe_2O_3,
- others: $Pb_3O_2SO_4$, $Cd_5(AsO_4)_3Cl$, $CdSO_4$, K_2ZnCl_4, $ZnCl_2$, $ZnSO_4$ [39].

The fluid bed combustion experiments of biomass with high heavy metal content show that the Pb, Zn and Cd compounds leave the combustion chamber at 700–800 °C especially quickly. The Pb, Zn and Cd contents of flue gas depending on time are shown in Figure 1 [40].

Three different exit ways should be studied in reference to heavy metals entering the combustion chamber: the solid remains in the combustion chamber (bottom ash); the solid particles in the flue gas (fly ash); and the exhausted gas (flue gas). Based on this fact a research determined, that the metals distribute very differently in the combustion system. Almost all of the Hg is exhausted; contrarily the Cu stays in the bottom ash mostly. The Cd and the Pb distribution was more uniform [36].

In every respect, the solubility of metals is a very important fact. The metals could be solubilized with chemicals from the solid remains (bottom ash, fly ash), but the solubility is influenced by the combustion technology [36] [42] [43], the metal compounds properties and other circumstances [44].

The change of heavy metal content depending on the pH of hydrochloric acid solvent was determined in fly ash [41]. Based on Figure 2, it can be stated, that the solubility of heavy metals is the highest in undiluted hydrochloric acid environment.

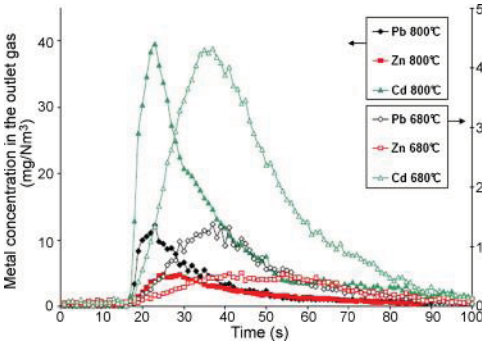

Figure 1
Pb, Zn and Cd content of flue gas depending on time [40]

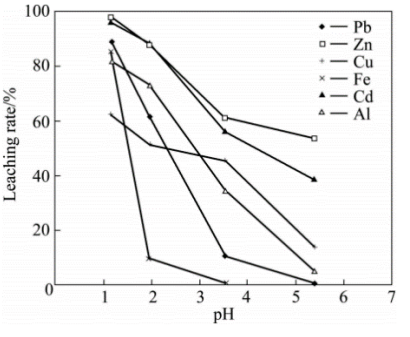

Figure 2
Solubility of heavy metals depending on hydrochloride pH [41]

During the combustion of metal contaminated biomass, it is required to analyze the hazard risk of solid remains (bottom ash, fly ash). Based on researches the volatile, toxic metals mean risk primarily to the environment [45] [37]. To determine the amount of metals in flue gas in volatile form is a higher technological challenge, and the technology of minimizing or ceasing the metal emission is the biggest environmental task. The dust (and condensed metal) extractor of flue gas is an obvious solution, but not perfect. The dust extractor could solve the metal emission problem only if the temperature of flue gas is low enough, and the condensation of metal compounds ends before the separator. If this condition is not fulfilled, than the efficiency of the extractor system is not fit for metal separation. In this case additional flue gas cleaning technology is required.

2.2. Particle removal systems

The particle removal technologies are very important in the case of biomass combustion especially if the fuel contains a high amount of metals.

The amount of solid particles in flue gas depends on fuel properties [46] and combustion technology [47]. Usually two types of fly ash are discerned: rough and fine dust particles [48]. In the cooling zones of the burning system, the metals are condensed with two different methods; fine particles are formed with homogeneous condensation [49], and on the surface of fine dust heterogeneous condensation takes place [50].

Several different particle separator systems exist, but to select and form the correct, efficient and sufficient technology is an engineering task. Particle removal from flue gas can be divided into categories (Figure 3) [51].

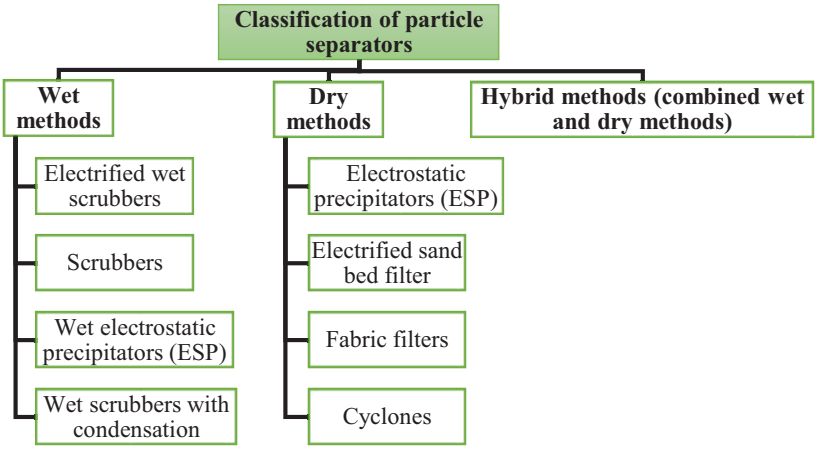

Figure 3
Particle removal system categories [51]

Figure 4 shows, that these technologies are applicable for the separation of specific solid particle diameter intervals efficiently.

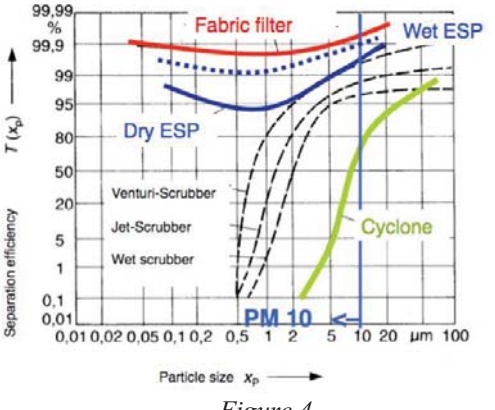

Figure 4
The dust extractor types regarding the efficient particle size separating [52]

Multi-cyclone equipment is often used by small industrial biomass furnaces, but the solid particle emission could exceed the emission limit value [53]. With filters or electrostatic precipitators the solid particle emission could decrease under 10 mg/Nm^3, but these equipments increase the operational costs significantly [53]. The fly ash needs to be bigger than 5 μm to separate with cyclones, but to separate the particles smaller than 1 μm electrostatic precipitators or filters are required [45]. The efficiency data of different particle separators are summarized in Table 2 [51].

Table 2
Particle separator efficiencies [52] [51]

Technology	a*	b**	c***	Notes
Cyclone	90–99	80–90	< 80	Less effective for small particles
Multi-cyclone	90–99	90–99	< 80	Less effective for small particles
Electrostatic Precipitator	> 99	> 99	80–90	Removal efficiency and emission may be low for small plant
Fabric Filter	> 99	> 99	> 99	Final emission should be much less than 5 g/GJ
Ceramic Filter	> 99	> 99	> 99	Final emission should be much less than 5 g/GJ
Mop Fan	> 95	> 95	> 95	Technology needs to be tested more for validity, also removes water soluble gas
Hybrid	> 99	> 99	> 99	Novel technology, more niche and problem specific

*a: Effectiveness (coarse particles) (%), b: Removal efficiency (PM10) (%), c: Removal efficiency (PM2.5) (%)

It can be stated that the cleaning of flue gas from biomass combustion is a complex task, and it is difficult to obtain high efficiency for a smaller particle range. The particle removal efficiency especially for PM 2.5 is usually low.

Conclusion

The environmental problems of solid particle emission are a seeded area in air cleaning protection goals. Solid particles are produced during every solid fuel combustion process, accordingly by biomass firing. The compounds of solid particles are composed by the fuel composition. It is evident, that every biomass contains a certain amount of metal compounds, but in the last decade, the metal contaminated biomass achieved increasing attention. Several researches deal with this topic including the biomass based remediation techniques, the metal accumulation process of biomass and the disposal options of biomass. The combustion, as a disposal option is a known process, but experiments dealing with emissions were performed only in the last few years. This research area is also important concerning energy production, as in these energy-hungry times every potential energy source should be analyzed. Regarding the literature it can be stated, that the combustion of contaminated biomass is not an ordinary biomass firing process. The particles in flue gas contain metal compounds, thus an efficient air cleaning system is crucial. The particle separation efficiency depends mainly on the cleaning equipment and on the temperature of flue gas. The flue gas temperature must be

under the temperature, where the condensation of metal compounds is finished. For particle separation, filters or an effective hybrid technology is required.

Acknowledgements

This research was carried out in the framework of the Center of Excellence of Sustainable Resource Management at the University of Miskolc.

References

[1] Phytoextraction. http://www.biology-online.org/articles/phytoremediation-a-lecture/phytoextraction.html (downloaded: June 7, 2016)

[2] DALUN, T.–FAN, Z.–WENDE, Y.–XI F.–WENHUA, X.–XIANGWEN, D.–GUANGJUN, W.–CHANGHUI, P.: Heavy metal accumulation by panicled goldenrain tree (Koelreuteria paniculata) and common elaeocarpus (Elaeocarpus decipens) in abandoned mine soils in southern China. *Journal of Environmental Sciences*, Vol. 21 (2009), 340–345.

[3] SZÁSZ G.: *Agrometeorológia.* Mezőgazdasági Kiadó, Budapest, 1988.

[4] VASSILEV, S. V.–BAXTER, D.–ANDERSEN, L. K.–VASSILEV, C. G.: An overview of the chemical composition of biomass. *Fuel*, Vol. 89, Issue 5 (2010), 913–933.

[5] GOMES, M. P.–CARNEIRO, M. M. L. C.–GARCIA, Q. S.: Chapter 17 – Trace Elements Tolerance Modulated by Antioxidant System in Plants. In: AHMAD, P. (ed.): *Oxidative Damage to Plants, Antioxidant Networks and Signaling.* Academic Press, 2014, 523–540.

[6] RUTTENS, A.–ADRIAENSEN, K.–MEERS, E.–VOCHT, A. D.–GEEBELEN, W.–CARLEER, R.–MENCH, M.–VANGRONSVELD, V.: Long-term sustainability of metal immobilization by soil amendments: Cyclonic ashes versus lime addition. *Environmental Pollution*, Vol. 158, Issue 5 (2010), 1428–1434.

[7] WILSON, S. C.–LEECH, C. D.–BUTLER, L.–LISLE, L.–ASHLEY, P. M.–LOCKWOOD, P. V.: Effects of nutrient and lime additions in mine site rehabilitation strategies on the accumulation of antimony and arsenic by native Australian plants. *Journal of Hazardous Materials*, Vol. 261 (2013), 801–807.

[8] GRAY, C. W.–DUNHAM, S. J.–DENNIS, P. G.–ZHAO, F. J.–MCGRATH, S. P.: Field evaluation of in situ remediation of a heavy metal contaminated soil using lime and red-mud. *Environmental Pollution*, Vol. 142, Issue 3 (2006), 530–539.

[9] GUALAB, S. D.–VEGA, F. A.–COVELO, E. F.: The dynamics of heavy metals in plant-soil interactions. *Ecological Modelling*, Vol. 221, Issue 8 (2010), 1148–1152.

[10] HALE, B.–EVANS, L.–LAMBERT, R.: Effects of cement or lime on Cd, Co, Cu, Ni, Pb, Sb and Zn mobility in field-contaminated and aged soils. *Journal of Hazardous Materials*, Vol. 199–200 (2012), 119–127.

[11] HÄNSCH, R.–MENDEL, R. R.: Physiological functions of mineral micronutrients (Cu, Zn, Mn, Fe, Ni, Mo, B, Cl). *Current Opinion in Plant Biology*, Vol. 12, Issue 3 (2009), 259–266.

[12] GANGWAR, S.–SINGH, V. P.–TRIPATHI, D. K.–CHAUHAN, D. K.–PRASAD, S. M.–MAURYA, J. N.: Chapter 10 – Plant Responses to Metal Stress: The Emerging Role of Plant Growth Hormones in Toxicity Alleviation. In: AHMAD, P.–RASOOL, S. (eds.): *Emerging Technologies and Management of Crop Stress Tolerance, Volume 2: A Sustainable Approach.* Academic Press, 2014, 215–248.

[13] SAS-NOWOSIELSKA, A.–KUCHARSKI, R.–MALKOWSKI, E.–POGRZEBA, M.–KUPERBERG, J. M.–KRYŃSKI, K.: Phytoextraction crop disposal – an unsolved problem. *Environmental Pollution*, Vol. 128, Issue 3 (2004), 373–379.

[14] ZHAO, F. J.–LOMBI, E.–BREEDON, T.–MCGRATH, S. P.: Zinc hyperaccumulation and cellular distribution in Arabidopsis halleri. *Plant Cell & Environment*, Vol. 23 (2000), 507–514.

[15] GUANGWEI, Y.–HENGY, L.–TAO, B.–ZHONG, L.–QIANG, Y.–XIANQIANG, S.: In-situ stabilisation followed by ex-situ composting for treatment and disposal. *Journal of Environmental Sciences*, Vol. 21 (2009), 877–883.

[16] BRIDGWATER, A. V.: Principles and practice of biomass fast pyrolysis processes for liquids. *Journal of Analytical and Applied Pyrolysis*, Vol. 51 (1999), 3–22.
[17] AL CHAMI, Z.–AMER, N.–SMETS, K.–YPERMAN, J.–CARLEER, R.–DUMONTET, S.–VANGRONSVELD, J.: Evaluation of flash and slow pyrolysis applied on heavy metal contaminated Sorghum bicolor shoots resulting from phytoremediation. *Biomass and Bioenergy*, Vol. 63 (2014), 268–279.
[18] STALS, M.–THIJSSEN, E.–VANGRONSVELD, J.–CARLEER, R.–SCHREURS, S.–YPERMAN, J.: Flash pyrolysis of heavy metal contaminated biomass from phytoremediation: influence of temperature, entrained flow and wood/leaves blended pyrolysis on the behaviour of heavy metals. *Journal of Analytical and Applied Pyrolysis*, Vol. 87, No. 1 (2010), 1–7.
[19] LIEVENS, C.–YPERMAN, J.–VANGRONSVELD, J.–CARLEER, R.: Study of the potential valorisation of heavy metal contaminated biomass via phytoremediation by fast pyrolysis: Part I. Influence of temperature, biomass species and solid heat carrier on the behaviour of heavy metals. *Fuel*, Vol. 87, Issues 10–11 (2008), 1894–1905.
[20] ŠYC, M.–POHOŘELÝ, M.–KAMENÍKOVÁ, P.–HABART, J.–SVOBODA, K.–PUNČOCHÁŘ, M.: Willow trees from heavy metals phytoextraction as energy crops. *Biomass and Bioenergy*, Vol. 37 (2012), 106–113.
[21] MULLIGAN, C. N.–YONG, R. N.–GIBBS, G. F.: Remediation technologies for metal-contaminated soils and groundwater: an evaluation. *Engineering Geology*, Vol. 60 (2001), 193–207.
[22] SAEEDA, A.–AKHTER, M. W.–IQBAL, M.: Removal and recovery of heavy metals from aqueous solution using papaya wood as a new biosorbent. *Separation and Purification Technology*, Vol. 45, Issue 1 (2005), 25–31.
[23] GARBISU, C.–ALKORTA, I.: Phytoextraction: a cost-effective plant-based technology for the removal of metals from the environment. *Bioresource Technology*, Vol. 77 (2001), 229–236.
[24] SARABÈR, A.: Co-combustion and its impact on fly ash quality; pilot-scale experiments. *Fuel Processing Technology*, Vol. 104 (2012), 105–114.
[25] STEENARI, B. M.–LINDQVIST, O.: Fly ash characteristics in co-combustion of wood with coal, oil or peat. *Fuel*, Vol. 78, Issue 4 (1999), 479–488.
[26] CHRISTENSEN, T. H.–KJELDSEN, P.–BJERG, P. L.–JENSEN, D. L.–CHRISTENSEN, J. B.–BAUN, A.–ALBRECHTSEN, H. J.–HERON, G.: Biogeochemistry of landfill leachate plumes. *Applied Geochemistry*, Vol. 16 (2001), 659–718.
[27] KJELDSEN, P.–BARLAZ, M. A.–ROOKER, A. P.–BAUN, A.–LEDIN, A.–CHRISTENSEN, T. H.: Present and long-term composition of MSW landfill leachate: a review. *Critical Reviews in Environmental Science and Technology*, Vol. 32, Issue 4 (2002), 297–336.
[28] CENNI, R.–FRANDSEN, F.–GERHARDT, T.–SPLIETHOE, H.–HEIN, K. R. G.: Study on trace metal partitioning in pulverized combustion of. *Waste Management*, Vol. 18 (1998), 433–444.
[29] KARIMANAL, K. V.–HALL, M. J.: Effect of temperature and flow on the volatilization of elemental lead and cadmium. *Hazardous Waste and Hazardous Materials*, Vol. 13 (1996), 63–71.
[30] PÁL KÁROLYNÉ: Nehézfémek a pernyében. *Környezetvédelmi Füzetek*, 1999.
[31] JÖLLER, M.–BRUNNER, T.–OBERNBERGER, I.: Modeling of aerosol formation during biomass combustion for various furnace and boiler types. *Fuel Processing Technology*, Vol. 88 (2007), 1136–1147.
[32] MCNALLAN, M. J.–YUREK, G. J.–ELLIOT, J. F.: The formation of inorganic particulates by homogeneous nucleation in gases produced by the combustion of coal. *Combuston and Flame*, Vol. 42 (1981), 45–60.
[33] JIAO, F.–ZHANG, L.–YAMADA, N.–SATO, A.–NINOMIYA, Y.: Effect of HCl, SO_2 and H_2O on the condensation of heavy metal vapors in flue gas cooling section. *Fuel Processing Technology*, Vol. 105 (2013), 181–187.
[34] RYUA, C.–YANGA, Y. B.–KHORA, A.–YATES, N. E.–SHARIFIA, V. N.–SWITHENBANKA, J.: Effect of fuel properties on biomass combustion: Part I. Experiments – fuel type, equivalence ratio and particle size. *Fuel*, Vol. 85, Issues 7–8 (2006), 1039–1046.
[35] SIMONEIT, B. R. T.–ROGGE, W. F.–MAZUREK, M. A.–STANDLEY, L. J.–HILDEMANN, L. M.–CASS, G. R.: Lignin pyrolysis products, lignans, and resin acids as specific tracers of plant classes in

emissions from biomass combustion. *Environmental Science & Technology*, Vol. 27, No. 12 (1993), 2533–2541.
[36] RANDALL SEEKER, W. M.: Waste combustion. *Symposium (International) on Combustion*, Vol. 23, Issue 1 (1991), 867–885.
[37] KHAN, A. A.–JONG, W. D.–JANSENS, P. J.–SPLIETHOFF, H.: Biomass combustion in fluidized bed boilers: Potential problems and remedies. *Fuel Processing Technology*, Vol. 90, Issue 1 (2009), 21–50.
[38] VERHULST, D.–BUEKENS, A.–SPENCER, P. J.–ERIKSSON, G.: Thermodynamic behavior of metal chlorides and sulfates under the conditions of incineration furnaces. *Environmental Science & Technology*, Vol. 30, No. 1 (1996), 50–56.
[39] EVANS, J.–WILLIAMS, P.: Heavy metal adsorption onto flyash in waste incineration flue gases. *Process Safety and Environmental Protection*, Vol. 78, Issue 1 (2000), 40–46.
[40] FALCOZ, Q.–GAUTHIER, D.–ABANADES, S.–PATISSON, F.–FLAMANT, G.: A general kinetic law for heavy metal vaporization during municipal solid waste incineration. *Process Safety and Environmental Protection*, Vol. 88 (2010), 125–130.
[41] KAI, H.–INOUE, K.–HARADA, H.–KAWAKITA, H.–OHTO, K.: Leaching behavior of heavy metals with hydrochloric acid from fly ash generated in municipal waste incineration plants. *Transactions of Nonferrous Metals Society of China*, Vol. 21, Issue 6 (2011), 1422–1427.
[42] TAO, H. C.–LEI, T.–SHI, G.–SUN, X. N.–WEI, X. Y.–ZHANG, L. J.–WU, W. M.: Removal of heavy metals from fly ash leachate using combined bioelectrochemical systems and electrolysis. *Journal of Hazardous Materials*, Vol. 264 (2014), 1–7.
[43] IZQUIERDO, M.–QUEROL, X.: Leaching behaviour of elements from coal combustion fly ash: An overview. *International Journal of Coal Geology*, Vol. 94 (2012), 54–66.
[44] VAN DER BRUGGEN, B.–VOGELS, G.–VAN HERCK, P.–VANDECASTEELE, C.: Simulation of acid washing of municipal solid waste incineration fly ashes in order to remove heavy metals. *Journal of Hazardous Materials*, Vol. 57, No. 1–3 (1998), 127–144.
[45] OBERNBERGER, I.–BRUNNER, T.–BARNTHALER, I.: Chemical Properties of Solid Biofuels – Significance and Impact. *Biomass and Bioenergy*, Vol. 27 (2006), 653–669.
[46] OBERNBERGER, I.–THEK, T.: Physical characterisation and chemical composition of densified biomass fuels with regard to their combustion behavior. *Biomass & Bioenergy*, Vol. 27 (2004), 653–669.
[47] JOHANSSON, L. S.–LECKNER, B.–GUSTAVSSON, G.–COOPER, D.–TULLIN, C.–POTTER, A.: Emission characteristics of modern and old-type residential boilers fired with wood logs and wood pellets. *Atmospheric Environment*, Vol. 38, No. 25 (2004), 4183–4195.
[48] WIINIKKA, H.–GEBART, R.–BOMAN, C.–BOSTRÖM, D.–NORDIN, A.–ÖHMAN, M.: High-temperature aerosol formation in wood pellets flames: Spatially resolved measurements. *Combustion and Flame*, Vol. 147, No. 7 (2006), 278–293.
[49] SENIOR, C. L.–FLAGAN, R. C.: Ash vaporization and condensation during combustion of a suspended coal particle. *Aerosol Science and Technology*, Vol. 1, Issue 4 (1982), 371–383.
[50] LINAK, W. P.–PETERSON, T. W.: Effect of Coal Type and Residence Time on the Submicron Aerosol Distribution from Pulverized Coal Combustion. *Aerosol Science and Technology*, Vol. 3, Issue 1 (1984), 77–96.
[51] SINGH, R.–SHUKLA, A.: A review on methods of flue gas cleaning from combustion of biomass. *Renewable and Sustainable Energy Reviews*, Vol. 29 (2014), 854–864.
[52] HAMILTON, S.–FLEMING, S.–STEWART, R.: *The assessment of flue gas particulate abatement in wood burning boilers. Report for Forestry Commission Scotland.* 2010. http://www.usewoodfuel.co.uk/media/234619/assessment-of-flue-gas-particulate-abatement-in-wood-burning-boilers-phase-1.pdf, (downloaded: June 7, 2016)
[53] HASLER, P.–NUSSBAUMER, T.: Particle size ditribution of the fly ash. In: KOPETZ, H.: *Biomass for Energy and Industry. 10th European Conference and Technology Exhibition.* C.A.R.M.E.N. Print, Würczburg, 1998, 1330–1333.

Materials Science and Engineering, Volume 41, No. 1 (2016) pp. 79–88.

AIR QUALITY IN THE NORTHERN HUNGARIAN REGION

KATALIN LANTAI[1]–ÁGNES WOPERA[2]–GÁBOR NAGY[3]

The emission of contaminants is determined by the structure of the national production and consumption, the quality and quantity of fuels used, the applied technologies, the transportation system and the demand for mobility. The amount of emitted contaminants has radically decreased during the past century. The contribution of each sector to air pollution has significantly changed as well. The tendencies characteristic to the Northern Hungarian region can only be determined based on long-term monitoring.
Keywords: air pollutants, emission, limit values, particulates

Introduction

A remarkable part of the population of Europe lives in places – mainly in cities – where sometimes certain limit values of air quality are exceeded. Serious health risks are presented by ozone, nitrogen dioxide, sulphur dioxide and particulate matter (PM) pollution.
Air pollution is not only a regional problem but one that affects whole Europe.
Currently, the two most significant pollutants with regard to health impacts are two fractions of particulate matter (the fraction under 10 micrometer: PM_{10}, and the fraction under 2.5 micrometer: $PM_{2.5}$) and ground level ozone.

In comparison with the international levels of air pollution, Hungary is in an average position. Therefore, the quality of air in Hungarian municipalities is considered not to be radically different from municipalities with similar size, characteristics and location abroad. Between 1990 and 2003, the changes in the economic system had a major effect on the air pollution of the country. The changes in the structure of industry had a considerable role in the decrease of air pollutants. Although the number of vehicles rapidly increased, the specific emissions decreased. The role of service industry also increased. Besides, the effects of environmental legislations and provisions are also noticeable during these years.

1. Data on national and regional air pollution

The emission of contaminants is determined by the structure of the national production and consumption, the quality and quantity of fuels used, the applied technologies and the transportation system. In case of air quality management, significant progress has taken place during the last 15 years and the quantity of emitted pollutants has considerably decreased. Between the late 80's and mid 90's, the change of the economic system and the declining of energy-intensive industrial activities resulted in a remarkable decrease of emission. The results of later measurements are the consequences of deliberate human interventions. The

[1] University of Miskolc, Department of Combustion Technology and Thermal Energy
3515 Miskolc-Egyetemváros, Hungary
uramkati@gmail.com
[2] University of Miskolc, Department of Combustion Technology and Thermal Energy
3515 Miskolc-Egyetemváros, Hungary
wopera.sa@gmail.com
[3] University of Miskolc, Department of Combustion Technology and Thermal Energy
3515 Miskolc-Egyetemváros, Hungary
nagy.gabii86@gmail.com

strict environmental requirements of the European Union force operators of activities causing air pollution to effectively reduce the emissions [1]. Figure 1 shows the changes in air pollution in Hungary from 2003 to 2013.

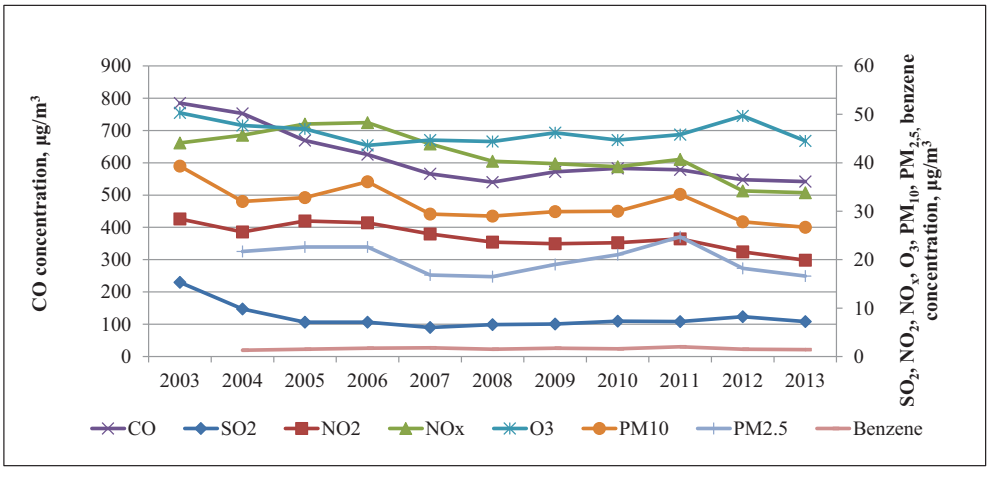

Figure 1
Air pollution in Hungary (2003–2013) [1]

Peaks of PM_{10} and $PM_{2.5}$ concentrations can be observed in 2011 caused by the cold winter weather. The concentration of all components decreased by 2013 which was partially a result of more favourable weather conditions. Precipitation contributes to the removal of surface dust. When the temperature is below the freezing point, the roads can not be washed therefore the accumulation of surface dust and the increase of PM_{10} concentration should be expected.

Not only the purification of air from pollutants is inhibited by dry weather, but the lifting of subsided dust is also facilitated. Table 1 gives information on the annual amount of precipitation.

Table 1
The annual amount of precipitation [2]

Year	Average annual precipitation compared to the average of 1971–2000 [%]
2005	120
2006	95
2007	108
2008	102
2009	105
2010	169
2011	72

Analysis of this data reveals interesting correlations: 2011 was a rather dry year as the annual amount of precipitation represented only 72% of the average of the base years (1971–2000), in contrast with the averages of 2005, 2007, 2008, 2009 and 2010 which exceeded that amount [2]. Moreover, overlapping can be observed between the rainless periods and the heating seasons of 2011, see Figure 2.

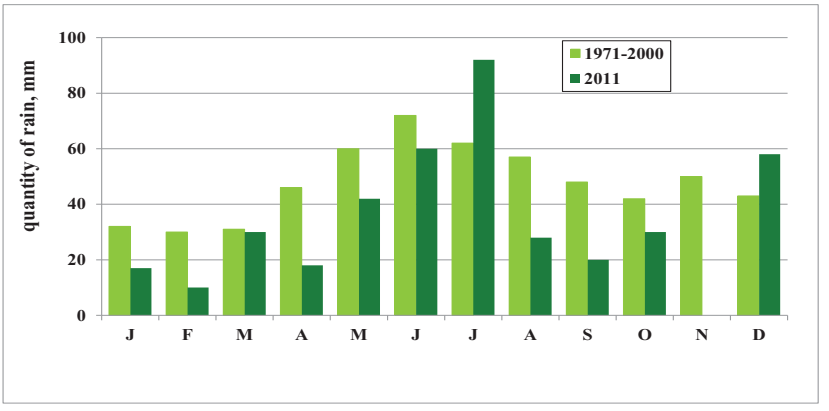

Figure 2
The amount of precipitation (2011) [2]

Based on the location of the monitoring station compared to the source of emission, the stations can be classified as urban, rural and industrial background and traffic type. Urban and rural background type stations are located in urban/rural areas not directly affected by industrial and traffic emissions, while industrial background types can be found near industrial establishments and traffic types near roads carrying heavy traffic. Figure 3 shows the aggregate PM_{10} concentration at the different types of monitoring stations in Hungary.

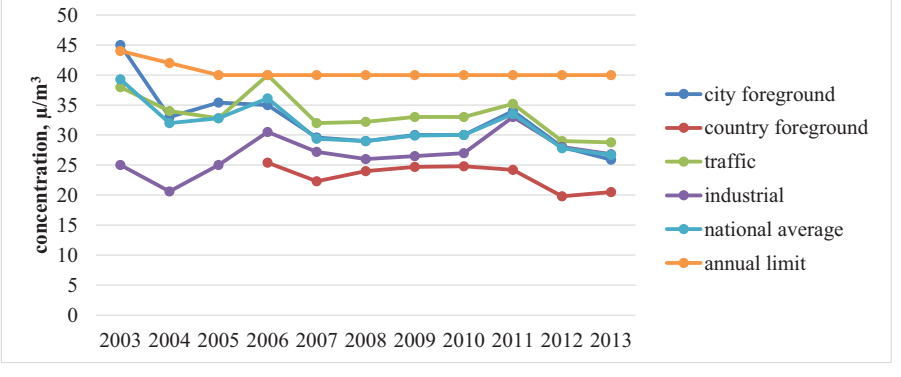

Figure 3
PM_{10} concentration at various types of monitoring stations [1, 5]

The measurement and evaluation of air quality in Hungary is performed by the Hungarian Air Quality Network (Országos Légszennyezettségi Mérőhálózat – OLM). The network consists of two major parts: automatic monitoring stations with continuous measurements of a wide range of air pollutants in ambient air, and a manual system (RIV) with sampling points and consecutive laboratory analysis of sulphur dioxide and nitrogen dioxide (and also subsiding dust in some places).
The locations of the monitoring stations in the Northern Hungarian region can be seen in Figure 4 [3].

Figure 4
Measuring stations in the Northern Hungarian region [3]

Information on the results of the measurements of various air pollutants from 2004–2014 can be seen in Figures 5–14.

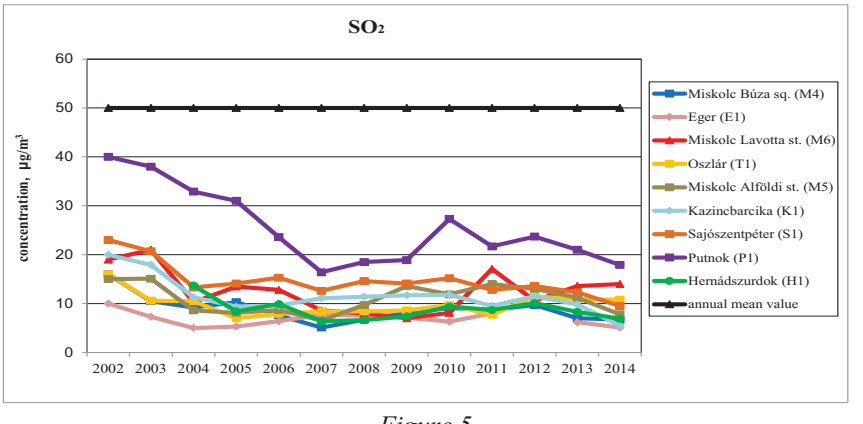

Figure 5
The change of SO_2 concentration in the region [3]

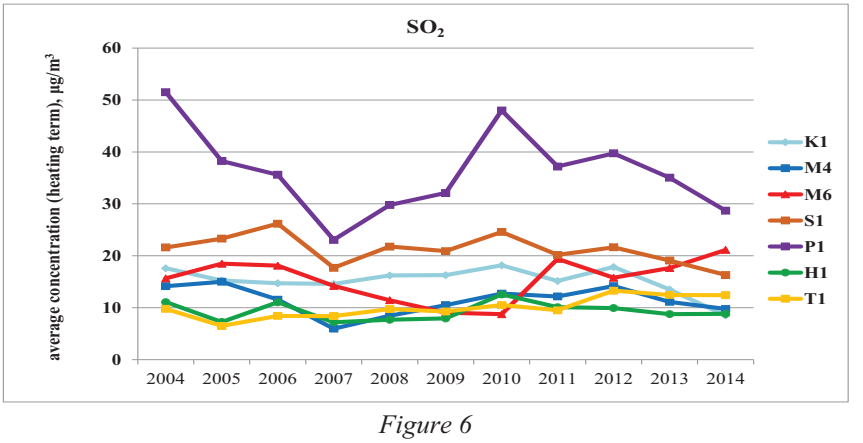

Figure 6
Average SO_2 concentration during the heating season [3]

One can see that the average annual concentration of SO_2 has been higher at Station P1 (Putnok), where coal based heating became increasingly more popular, than at any other monitoring stations. The effect has decreased over the past 3 years, though. Figure 6 and 7 illustrates that the values are higher at each monitoring station during the heating season.

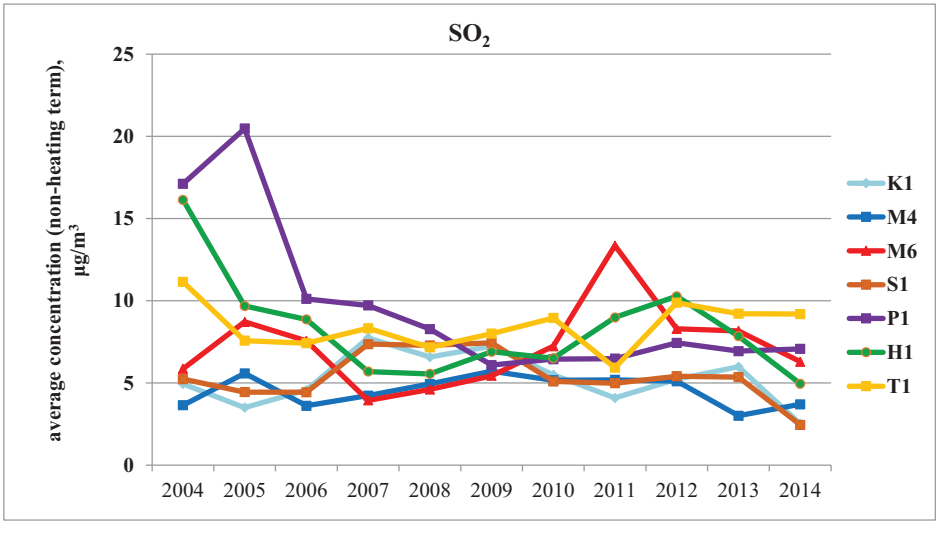

Figure 7
Average SO_2 concentration during the non-heating season [3]

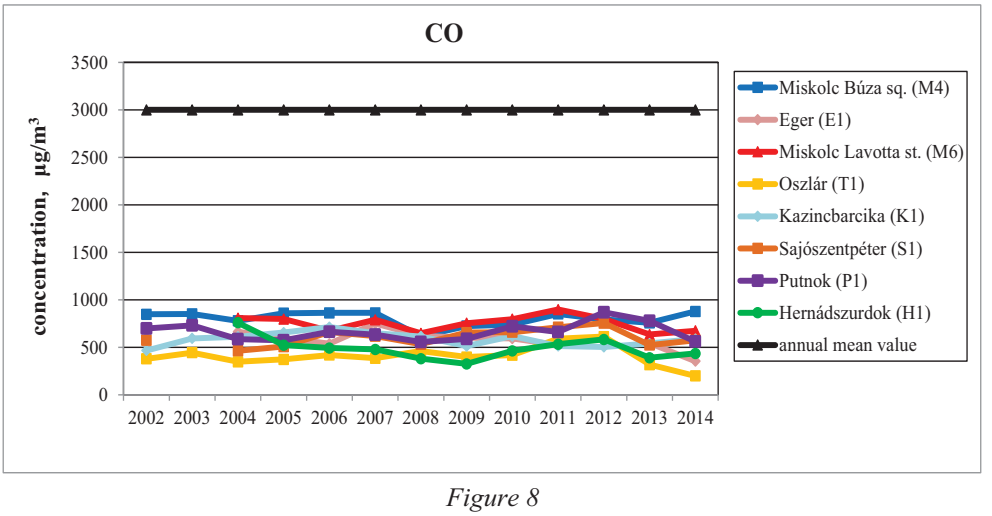

Figure 8
The change of CO concentration in the region [3]

The measured carbon monoxide values were always between 10–15% of the limit value. This pollutant does not pose any air quality risks.

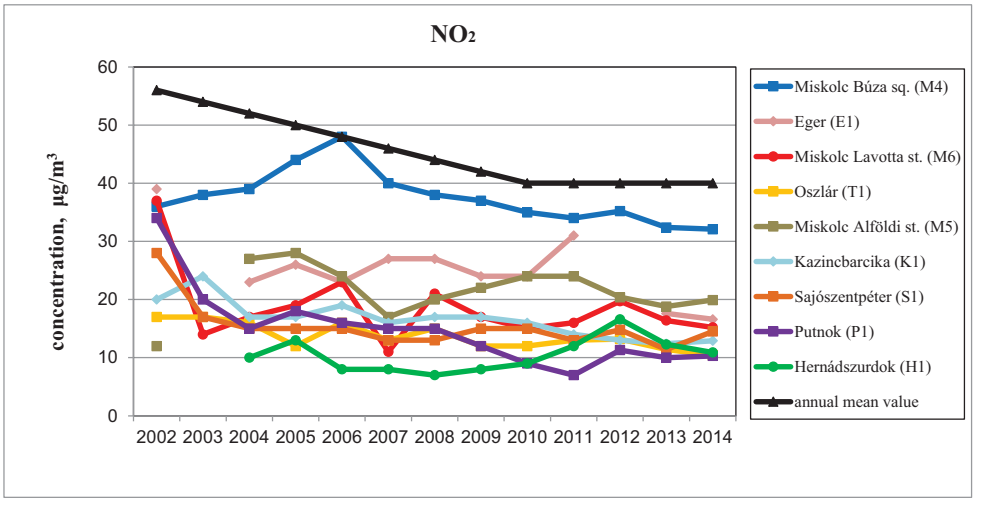

Figure 9
The change of NO_2 concentration in the region [3]

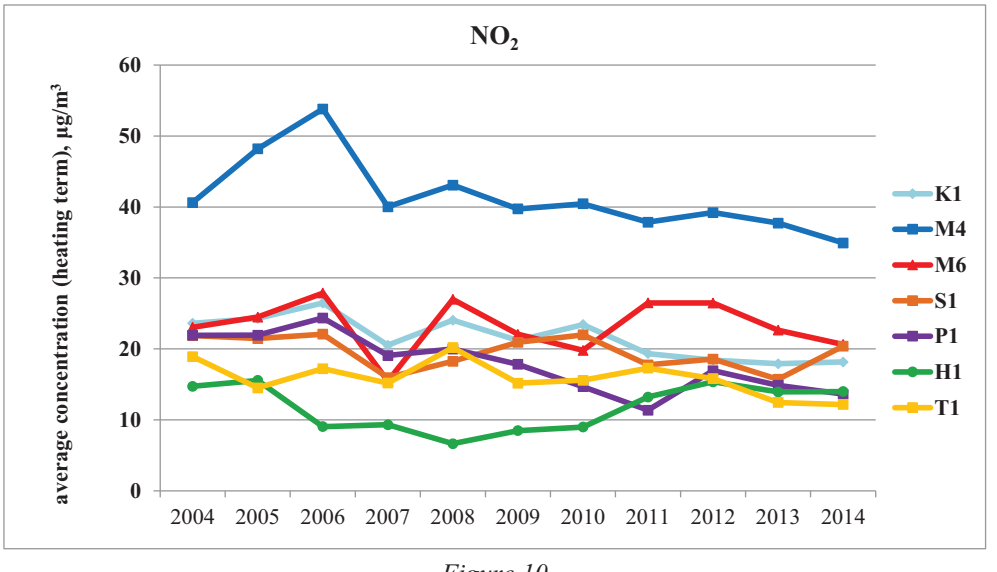

Figure 10
Average NO_2 concentration during the heating season [3]

Unlike the national results, NO_2 concentrations monitored at the regional monitoring stations were below the annual limits all the time, even at Station M4 (City of Miskolc, Búza square) where the emission is typically of traffic origin.

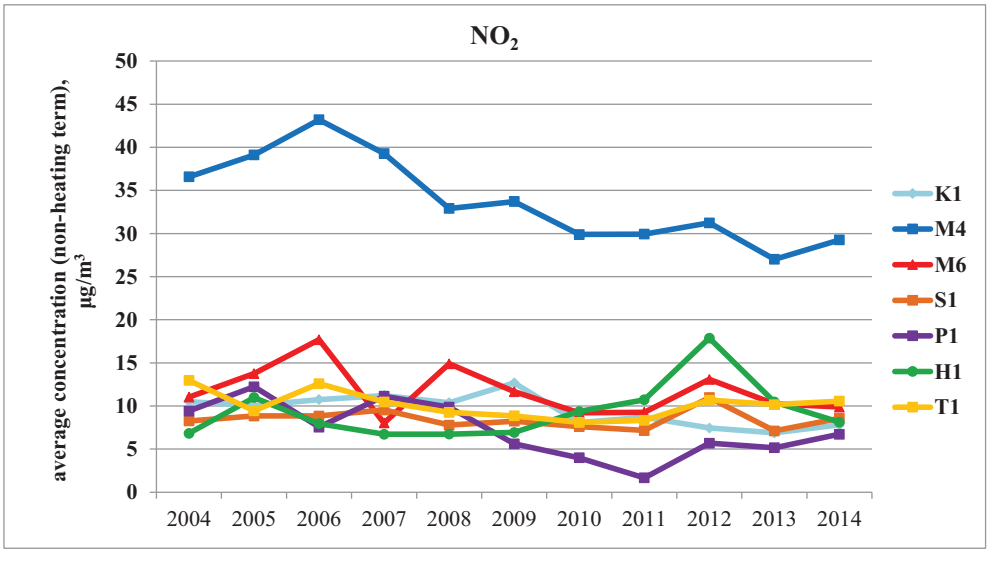

Figure 11
Average NO_2 concentration during the non-heating season [3]

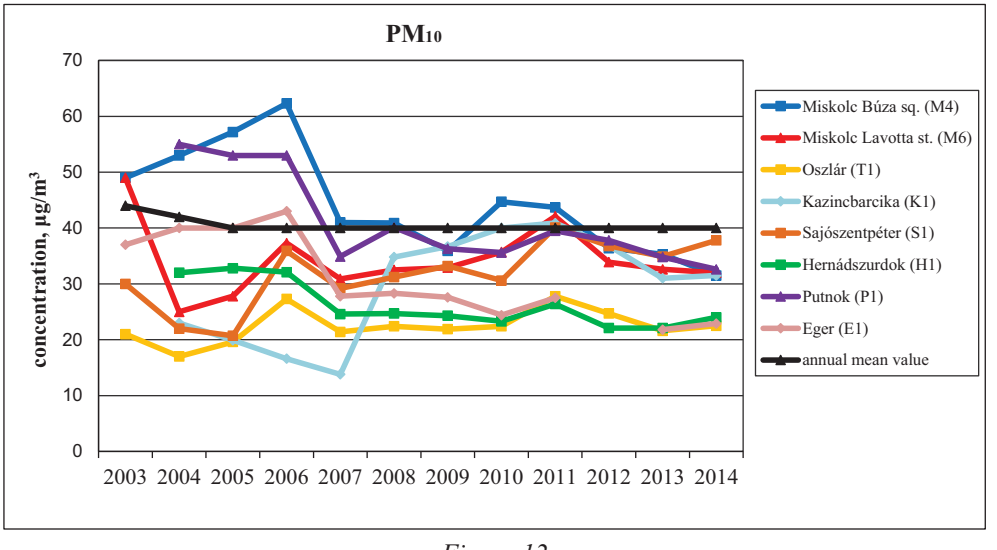

Figure 12
The change of PM_{10} concentration in the region [3]

From 2012 on the average annual PM_{10} concentrations are below the limit values (40 µg/m^3) at each station. However, this limit is exceeded during the heating season (Figure 13).

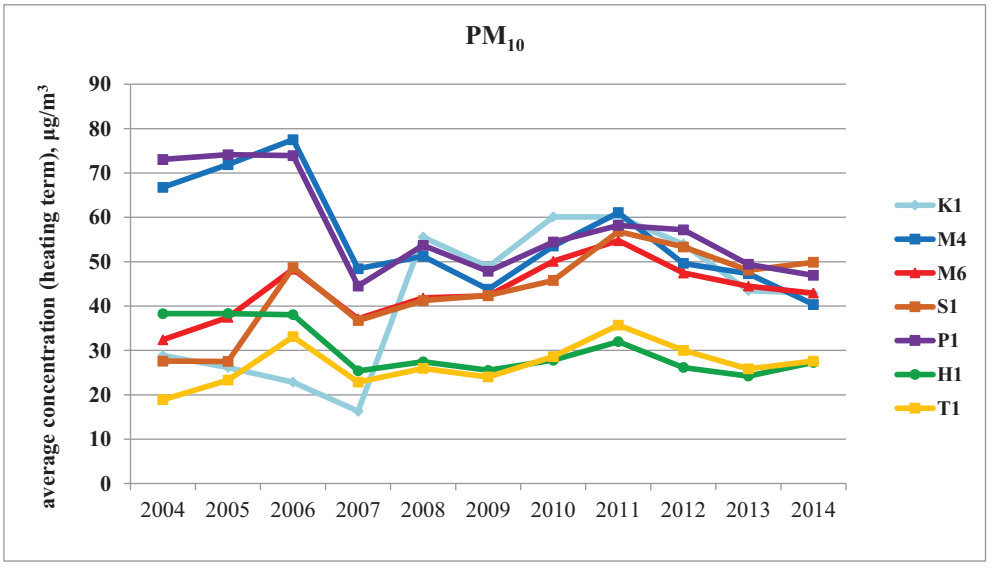

Figure 13
Average PM_{10} concentration during the heating season [3]

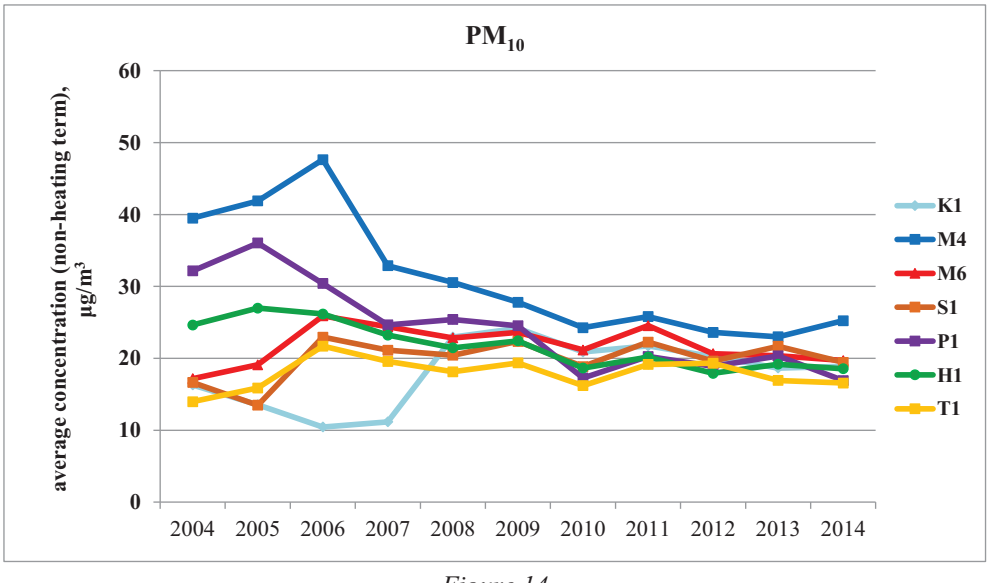

Figure 14
Average PM_{10} concentration during the non-heating season [3]

The importance of various anthropogenic sources in PM_{10} and $PM_{2.5}$ emissions in the EU member States in 2009 can be seen in Figure 15. According to the figure, an outstanding proportion is occupied by non-industrial combustion sources in both PM emissions, 9% higher in case of $PM_{2.5}$. Transportation comes second in both fractions. The difference

between the proportion of agricultural emission is rather conspicuous, as the PM_{10} emission is almost three times higher than the $PM_{2.5}$ emission [6].

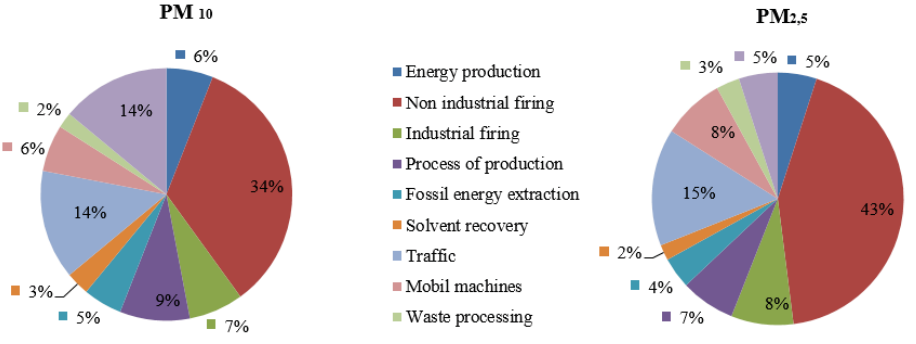

Figure 15
The distribution of PM_{10} and $PM_{2.5}$ emissions, based on the sources (2009) [6]

The information and alert thresholds of particulates were introduced in Regulation 14/2001 (V. 9.) KöM-EüM-FVM on 25 October 2008 and are also contained in Regulation 4/2011 (I. 14.) VM which is currently in force [4]. Information on the PM_{10} concentration during the smog episode in 2014 can be seen in Figure 16.

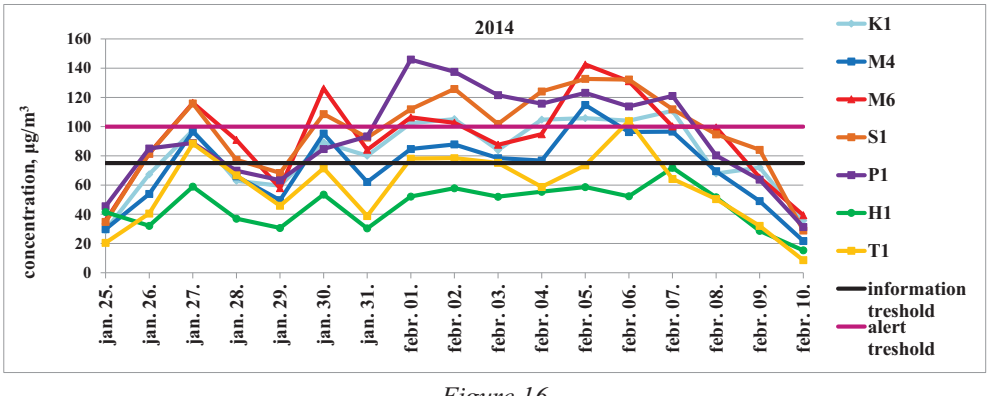

Figure 16
The change of PM_{10} concentration during the smog episode in January–February 2014 [3]

During the investigated period, similarly to previous results from the region, the only value to exceed information and alert thresholds was the concentration of PM_{10}. Almost all exceedances happened during inversion periods or unfavourable meteorological conditions, and the PM_{10} concentration was high at all monitoring and background stations in the country.

Conclusions

According to the data presented, the limit values of the average annual CO, SO_2 and NO_2 concentrations given by the relevant legislation were not exceeded in the Northern Hungarian

region. However, some measurements showed SO_2 concentrations close to the limit value during the heating season.

The carbon monoxide values never exceeded the 10–15% of the limit value in the region. This pollutant does not pose any air quality risks.

Unlike the national results, the NO_2 concentrations measured at the regional monitoring stations were below the annual limits every time, even at the Miskolc Búza sq. Station where the emission is typically of traffic origin.

However, the measurements of PM_{10} (particulate matter) are more adverse. The limit is exceeded at some stations evet at an annual basis but the exceedance of limitations is more significant during the heating season and detectable at almost all, with the exception of two, measuring stations.

Acknowledgement

This research was carried out in the framework of the Centre of Excellence of Sustainable Resource Management at the University of Miskolc.
The authors are grateful to Mária Ambrus for her advice.

References

[1] LRK Data Centre: *Year 2011 summary of the evaluation of Hungarian air quality based on the data of automatic monitoring network, prepared by the National Meteorological Services*. http://www.levegominoseg.hu/Media/Default/Ertekeles/docs/2011_automata_ertekeles.pdf
[2] National Meteorological Services http://www.met.hu
[3] National Network for Air Quality Monitoring http://www.levegominoseg.hu/
[4] Regulation "4/2011. (I. 14.) VM" about the limits of air quality levels and the limits for stationary air pollution emitters. http://net.jogtar.hu/jr/gen/hjegy_doc.cgi?docid=A1100004.VM
[5] PUSKÁS, M.: *Change of National Air Quality in 2012.* Balatonöszöd, 2013.
[6] KUGLER: *Straßenverkehrsemissionen in Europa – Emissionsberechnung und Bewertung von Minderungsmaßnahmen.* Universität Stuttgart Institut für Energiewirtschaft und Rationelle Energieanwendung, Forschungsbericht, 2012.

Materials Science and Engineering, Volume 41, No. 1 (2016) pp. 89–95.

STUDY OF THE ELECTROLYTIC DEGRADATION OF ORGANIC POLLUTANTS IN WASTEWATER

FERENC MOGYORÓDY[1]

The electrolytic degradation of organic pollutants in pesticide wastewaters was studied in a three electrode system. The lab-scale experiments show complete mineralization.
Keywords: wastewater, degradation, electro oxidation, thiocarbamate

Introduction

Thiocarbamates are widely used as herbicides and pesticides world-wide. The thiocarbamate containing wastewater formed during their production as well as the herbicides transferred from the plantations (fields, soil) into the surface waters can be regarded as a serious environmental protection problem.

Our aim was the possible maximum decontamination of the thiocarbamate herbicides by electrochemical degradation.

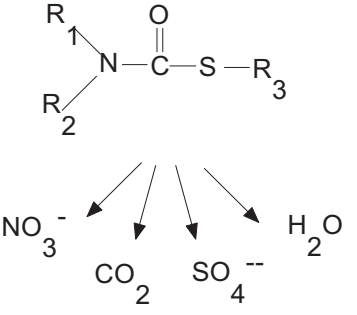

The aim is complete mineralization by electro-oxidation, resulting in the above decomposition products from the thiocarbamate molecule. Electrochemical techniques have often been considered to be a way of eliminating the toxic compounds contained in certain effluents and wastewaters [1]. It is now accepted that a simple modification of the molecular structure can considerably reduce the toxicity of a compound [2].

Nowadays, the thiocarbamate wastewater is first treated with Cl_2 gas, then it undergoes biological treatment, where bacteria degrade the contaminants further, and finally relatively clean water leaves the water cleaning system.

We have studied the electrochemical degradation of five thiocarbamate based herbicide (EPTC, Butylate, Cycloate, Molinate, Vernolate) produced by Sagrochem Ltd. The results are illustrated for the case of EPTC (S-Ethyl-N,N-dipropyl-thiocarbamate).

[1] University of Miskolc, Institute of Chemistry
3515 Miskolc-Egyetemváros
fkmmf@.uni-miskolc.hu

1. Experimental

A three electrode system was used in the laboratory experiments: the anode and the cathode consisted of an indifferent Pt-mesh with a large surface area; AgCl-electrode was used as the reference electrode. The constant potential was maintained by an EF 427 type potentiostate. The intermediates produced were analyzed by a Hewlett-Packard 1084B HPLC. The determination ot the Total Organic Carbon content (TOC) was done by a Heraeous Liqui TOC 2001 instrument. A Hewlett-Packard 8452A diode-array spectrophotometer was applied for the determination of the SO_4^{2-} content according to standard procedure.

Reagents

The initial concentration of the EPTC made by Sagrochem Ltd. was 100 ppm. The conducting electrolyte was 0.5 kmol.m^{-3} NaCl (Reanal).

The pH was set by HCl in the acidic or by NaOH in the basic range. Distilled water was used as the solvent.

2. Results and Discussion

The total degradation of EPTC (its structure shown below)

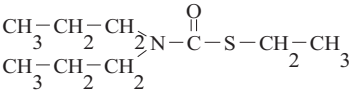

(1)

and other thiocarbamates can be realized by chemical oxidation (using chlorine or hypochlorite as the oxidizing agent), photochemical oxidation [3] (photolysis or photo catalysis by TiO_2). These procedures can be extended by the electrochemical oxidation the application of which for this problem has not been mentioned in the literature before [4].

Based on the oxidation with hypochlorite, we tried to form Cl_2 and hypochlorite *in situ* by the electrolysis. The production of hypochlorite by electrolysis has been extensively studied in the literature. KELSALL et al. [5] studied the electrolysis of NaCl in aqueous solution.

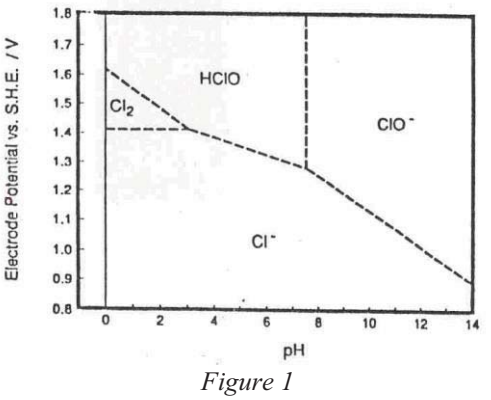

Figure 1
The electrochemical stability diagram of NaCl-H_2O system (KELSALL et al. [5])

Depending on the pH and the potential, four stable regions can be distinguished. The electrode reactions taking place in this system are the following:

$$\text{Anode: } 2\ Cl^- \rightarrow Cl_2 + 2\ e^- \quad (2)$$

$$\text{Cathode: } 2\ H_2O + 2\ e^- \rightarrow 2\ OH^- + H_2 \quad (3)$$

The reactions occurring in the solution:

$$Cl_2\ (aq) + H_2O \rightarrow HClO + Cl^- + H^+ \quad (4)$$

$$HClO \leftrightarrow H^+ + ClO^- \quad (5)$$

Besides the above reactions, other side reactions can also take place. Thus, the system is very complex depending on the pH and the applied potential. The electrochemical degradation of the EPTC can be realized in this system based on the fact that in addition to the electrochemical oxidation, chemical reaction occurs as well.

During the electrolysis oxidation takes place on the anode and reduction occurs on the cathode. When the anode is not spatially separated from the cathode, there is possibility for no macroscopic change, since the products of the anodic oxidation can be reduced on the cathode and vice versa. Therefore, the anode has to be separated from the cathode in many cases [6].

This was not necessary in our experiments, because of the simultaneous electrochemical and chemical reactions. The following figures represent the results of the EPTC electrolysis in four regions based on HPLC measurements. The initial concentration of EPTC and NaCl was the same in every experiment.

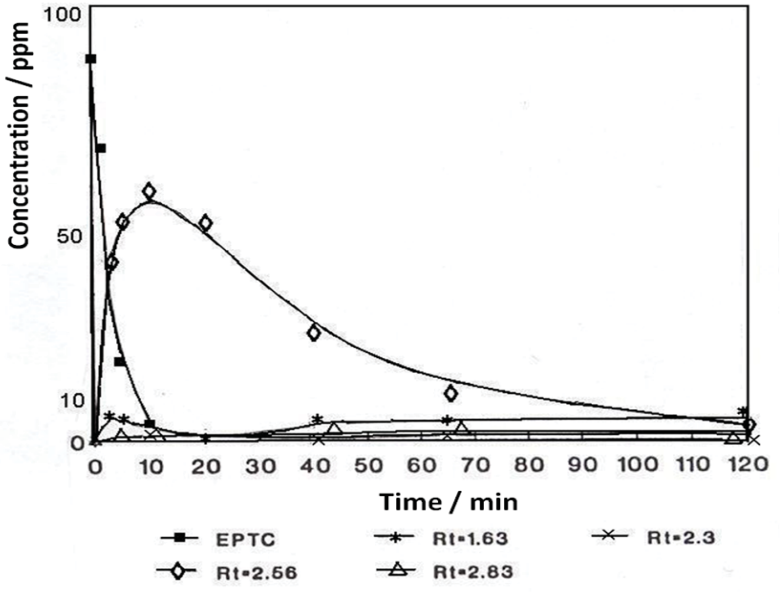

Figure 2 a)
The electrolysis of EPTC in the ClO^- region (pH = 11; Pot = 1.3 V)

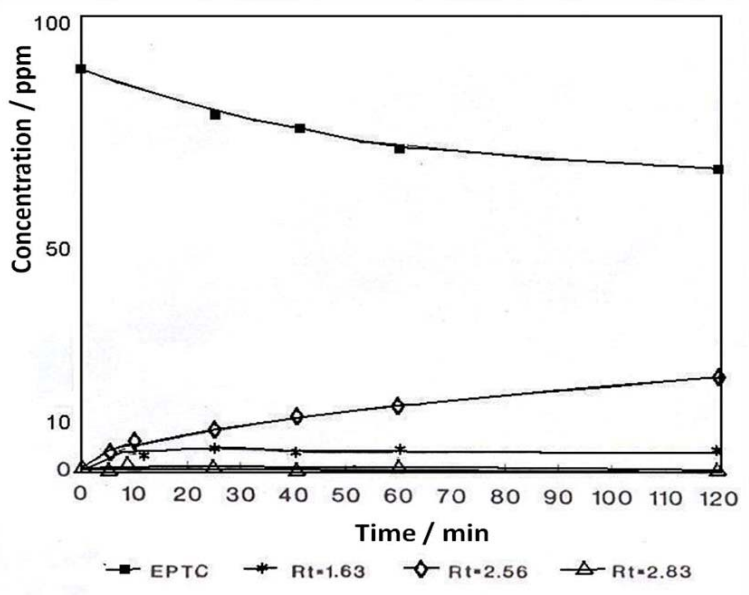

Figure 2 b)
The electrolysis of EPTC in the Cl^- region (pH = 7; Pot = 1.1 V)

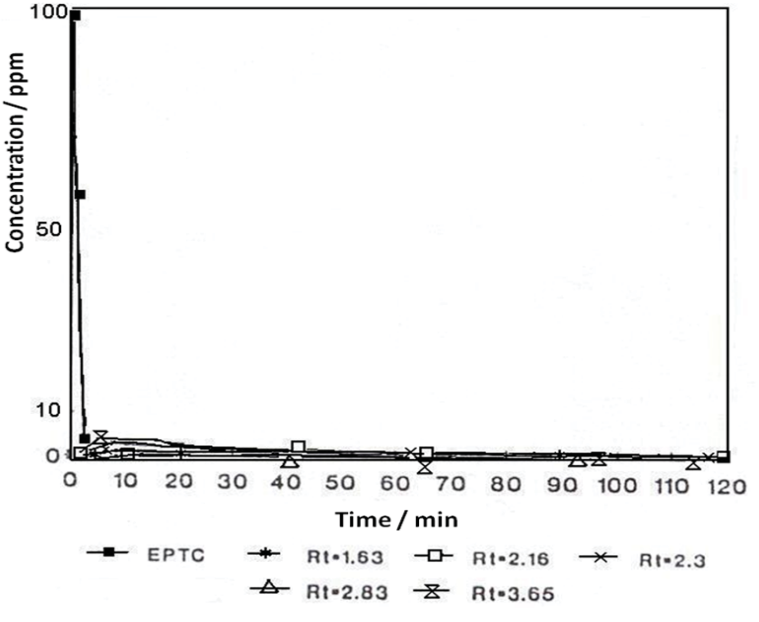

Figure 2 c)
The electrolysis of EPTC in the HClO region (pH = 4; Pot = 1.5 V)

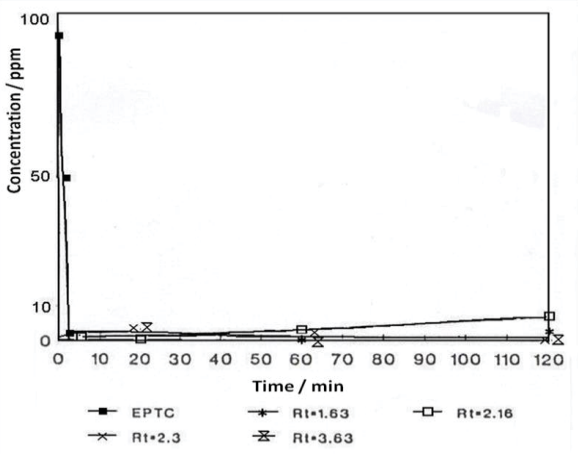

Figure 2 d)
The electrolysis of EPTC in the Cl_2 region (pH = 2; Pot = 1.45 V)

The pH and the applied potential were varied during the electrolysis of EPTC, and as it is shown in Figure 1, the degradation takes place differently depending on these two parameters. All four measurements were carried out up to the same time (2 hrs) and the EPTC was totally degraded in all cases except the Cl^- region. Only the electrochemical oxidation of EPTC occurs in this region, other chemical reaction does not take place. Thus, the EPTC does not degrade totally, and at the same time, the concentrations of the intermediates, from the degraded EPTC, having different retention times (Rt) show an increase based on the HPLC chromatograms. The degradation is the fastest in the Cl_2 containing region, and almost as fast in the HClO region. Remarkable, the dramatic decrease in the concentration of the EPTC, when practically after only three minutes there was no detectable EPTC in the system. Although, intermediates of different retention times are produced as well, but they are also degraded. The degradation of EPTC is not so fast in the ClO^- region, where concentration of the intermediate of retention time of 2.56 increases significantly in the beginning, but by the end of the electrolysis, this species also disappears.

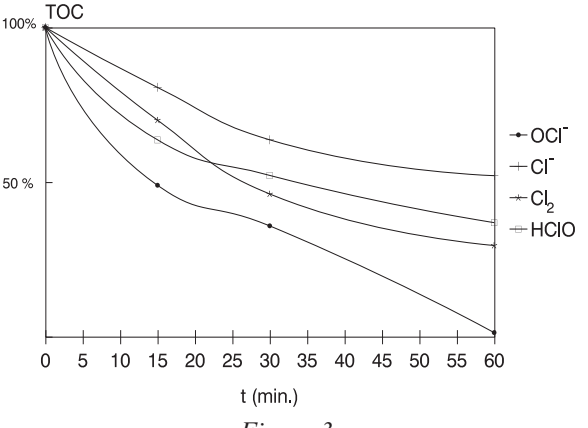

Figure 3
The results of the TOC measurements

Figure 3 represents the results of the measurements of the Total Organic Carbon (TOC) content in the different regions. The TOC decreased with time in all four regions. During the electrolysis the TOC decreased to less than half of its initial value in every case except the Cl^- containing region. In the ClO^- region the final TOC value was almost zero which is interesting, because the real industrial wastewater not only contains NaCl but is also alkaline, so it is easy to reach complete mineralization in it by electro-oxidation.

The results of the SO_4^{2-} measurements are shown in Figure 4. Since initially there was not any SO_4^{2-} in our system, it can only be formed from the S atom of EPTC during the electrolysis. The S-ethyl group can be removed most easily from the EPTC molecule, which after forming diethyl-disulfide (Et-S-S-Et), is finally oxidized to sulfate. Thus, the sulfate-ion can be formed only in the oxidation of the thiocarbamate molecule in this system.

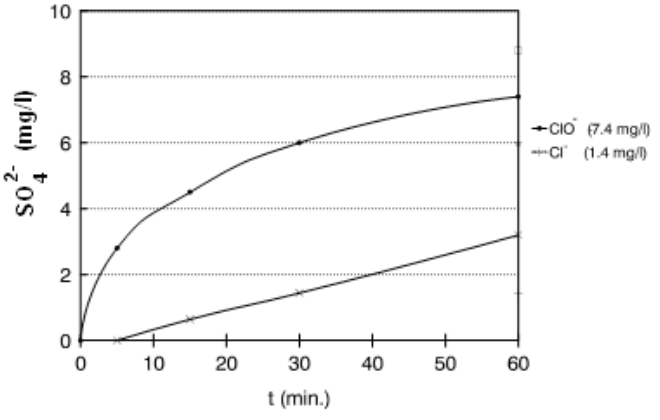

Figure 4
The results of the SO_4^{2-} measurements

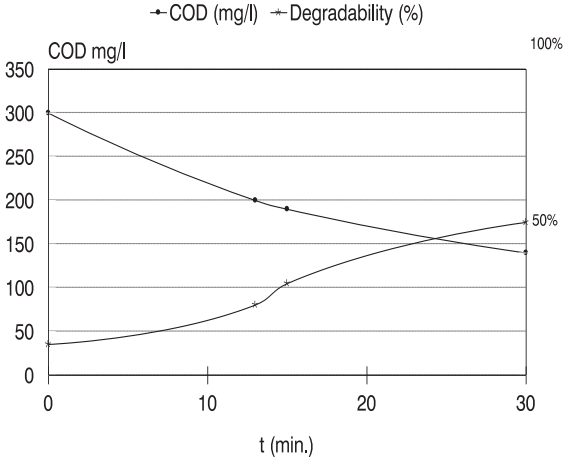

Figure 5
The Chemical Oxygen Demand (COD) and the results of degradability

Figure 5 shows the Chemical Oxygen Demand (COD) and results of the degradability measurements in the ClO^- region. The COD decreases to half of its initial value within 30 minutes as a result of electrolysis. The degradability increases to 50% relative to the low initial value.

Conclusion

Based on our measurements, it can be concluded that the EPTC can be decomposed by electrolysis. Complete mineralization of organic pollutants occurs in lab-scale experiments. This could be a new method for wastewater treatment in environmental protection. A procedure for the electrochemical degradation of thiocarbamate wastewater has been developed.

Acknowledgement

The described work was carried out as part of the TÁMOP-4.2.1.B-10/2/KONV-2010-0001 project in the framework of the New Hungarian Development Plan. The realization of this project is supported by the European Union, co-financed by the European Social Fund.

References

[1] KREYSA, G.–JÜTTNER, K.: *3. ESEE.* Nancy, 1994, 247.
[2] SEIGNEZ, S.–PULGARIN, C.–PERINGER, P.–COMNINELLIS, C.–PLATTNER, E.: Degradation of industrial organic pollutants. Electrochemical and biological treatment and combined treatment. *Swiss Chem,* Vol. 14, No. 1 (1992), 25–30.
[3] VIDAL, A.–DINYA, Z.–MOGYORÓDY, F.: Photocatalytic Degradation of Thiocarbamate Herbicide Active Ingredients in Water. *Applied Catalysis B: Environmental,* Vol. 21, No. 4 (1999), 259–267.
[4] MOGYORÓDY, F.: Influence of chlorine-water equilibria on the electrochemical destruction of thiocarbamate herbicides in NaCl solutions. *J. of Appl. Electrochemistry,* Vol. 36, No. 7 (2006), 765–771.
[5] BOXAL, C.–KELSALL, G. H.: *ICHEME Symposium,* 127, 59.
[6] NEUMANN, H. P.–HERTWIG, K.–WIEGAND, J.: *Wiss. Zeitschrift der TH Köthen,* 3 (1992), 63–72.

Materials Science and Engineering, Volume 41, No. 1 (2016) pp. 96–104.

COMPUTER SIMULATION OF SEMI-SOLID MATERIAL FLOWABILITY

DÁNIEL MOLNÁR[1]–BALÁZS SÁNDOR[2]

High pressure die casting is a near net shape process where turbulent filling and rapid solidification occurs under high pressure conditions. Alternative die casting technologies such as rheocasting have been developed in order to increase the quality of castings. The simulation of flowability and fillability is influenced by several factors such as temperature of the melt and the die, viscosity behaviour in the mushy zone, solid particle ratio and flow properties. Here a control volume model is developed to simulate the rheocasting process based on the commercial software NovaFlow&Solid. Several simulation trials were carried out to examine the flowability of normal AlSi7Mg alloy and its semisolid version.
Keywords: semi-solid rheocasting, flow behaviour, flow-test, computer simulation

1. Semi-solid metal processing

Lightweight metals are used extensively by the automotive and transport industries, both in wrought and cast forms. Recently the European Aluminium Association (EEA) reported that the amount of aluminium used in new European cars had risen between 1990–2010 from 50 kg to 140 kg, so it is not surprising to see there is a growing tendency to employ aluminium and aluminium alloys in the automotive and transport industries. Cast aluminium components are mainly used in chassis and suspension applications, wheels, steering parts, cylinder heads, brake drums, connecting rods etc. Today, based on data from the EEA, some 73% of cast alloys go into the transport sector in Europe and due to high production rate and dimensional stability as well as excellent surface finish and high volume production, a large number of these parts are produced by high pressure die casting method.

In the search for improved alloy properties, a number of casting techniques have been developed and introduced on the market in last four decades, such as semi-solid forming or squeeze casting. Squeeze casting is a casting method of producing near-net-shape parts in which the liquid metal charge is forged to shape inside closed dies. It combines the strength and integrity of forging with the economy and design of flexibility of casting. The process became commercially available in the mid-1970s for custom manufacture of nonferrous components. Compared with conventional casting techniques, squeeze cast products have a very good combination of strength and elongation, which mainly comes from their high density and finer and more homogenous microstructures [1, 2].

[1] University of Miskolc, Institute of Foundry Engineering
Miskolc-Egyetemváros 3515, Hungary
daniel.molnar@uni-miskolc.hu
[2] University of Miskolc, Institute of Foundry Engineering
Miskolc-Egyetemváros 3515, Hungary
sandorb17@gmail.com

1.1. Undercooling requirement

The driving force of any phase transformation, including solidification, is the change in free energy. The free energy per mole (molar free energy) or per unit volume (volumetric free energy) of a substance can be expressed as

$$F = E + P * v - T * S \tag{1}$$

where E is internal energy (i.e. the amount of work required to separate the atoms of the phase to infinity), P is pressure, v is volume, T is temperature and S is entropy. Thermodynamics stipulates that in a system without outside intervention, the free energy can only decrease.

The change in free energy can be described by the sum of the increase resulting from the relaxation of each particular assumption:

$$\Delta F = -\Delta G_v + \Delta G_r + \Delta G_T + \Delta G_c + \Delta F_P \tag{2}$$

The four positive right-hand terms are the increase in free energy because of curvature, temperature, composition, and pressure variation, respectively. Let us now evaluate the terms in this equation.

The driving force in the evaluation of spheroidal grains is the curvature undercooling. As the volume of a solid particle in a liquid decreases, its surface/volume ratio increases and the contribution of the interface energy to the total free enthalpy of the particle increases. Thus, when the particle size decreases in a liquid-solid system, the total free enthalpy of the solid increases.

When the particle increases by dr, where r is the radius, the work resulting from the formation of a new surface, $d(4\pi r2\gamma)dr$, must be equal to that resulting from the decrease in the free volumetric energy,

$$\frac{d}{dr}\left(\frac{4}{3}\pi r^3 \Delta G_v\right) \tag{3}$$

Equating the two, after differentiation, the increase in free energy is

$$\Delta G_v = \frac{2\gamma}{r} = \gamma K \tag{4}$$

where γ is the liquid-solid surface energy, and K is the curvature. Then, from the definition of undercooling:

$$\Delta T = \Delta G_v / \Delta S_f \tag{5}$$

can be obtained,

$$\Delta S_f \Delta T_r = \gamma K \text{ or } \Delta T_r = T_e - T_e^r = \left(\frac{\gamma}{\Delta S_f}\right) K = \Gamma K \tag{6}$$

where ΔT_r is the curvature undercooling, T_e is the equilibrium (melting) temperature for a sphere of radius r, and Γ is the Gibbs–Thomson coefficient [3].

1.2. Spheroidal grain evolution

Coarsening or ripening is an important aspect of the microstructure evolution in semi-solid processes. The relationship between particle size, isothermal shearing and shearing time has been presented which states that the particle size increases with time when spherodisation occurs, but particle size decreases when going from dendritic rosette-like shape. During ripening, the particles become smaller and the average size of α-Al phase increases, as small particles tend to disappear. The reduction in interfacial energy of particles total area is the driving force for the Ostwald ripening, which can be described by the so-called FSW rate equation in the case of diffusive mass transport. A rate equation adapts Ostwald's ripening theory modified to semi-solid systems:

$$D_m^3 - D_0^3 = F_{vf} * K_{LSW} * (t - t_0) \tag{7}$$

where D_m is the mean diameter of the particles after time t, D_0 is the initial average diameter when t equals t_0, F_{vf} is a function of solid volume fraction and K_{LSW} is the growth constant.

In the case of convective coarsening it was shown that coarsening is not only enhanced, as fluid flow leads to a faster mass transport, but also the coarsening kinetics are changed. A new rate equation is derived for solid particles moving with Stokes speed. Then the average particle size increases with time as

$$D^2 - D_0^2 = A * K_{LSW} * \frac{(1-f_s)^{\frac{2}{3}}}{f_s} * \omega^{\frac{1}{3}} * t \tag{8}$$

where the parameter ω refers to the rotation frequency and A is the constant containing the diffusion coefficient [2–4].

2. Simulation of the process

NovaFlow&Solid is a Control Volume simulation software package which is developed by Swedish NovaCast Technologies AB under continual development since 1993. Conservation laws (of matter balance, pulse and energy) form the foundation of physical-mathematical models of the program. These conservation laws take into account the phase transitions taking place in the solidifying casting, the exact geometry of the casting and mould, and heat mass exchange with environment.

Properties of fluids play a primary role for the development of mathematical models for fluid flow simulation. One should make clear assumptions about which property can be assumed to be constant and which depends on temperature, pressure etc. Where properties depend on temperature variable, an additional coupling between various conservation equations arises. Properties enter as coefficients in the conversation equations. The magnitude of these coefficients can change the overall picture of the flow.

Mass density of the fluid is defined as the ratio of the mass of the fluid to the volume occupied by this fluid. Taking the limiting value of this ratio for the infinitesimal volume, we obtain the defining equation of density ρ, [kg/m^3]. In a general case, fluid density depends on temperature and pressure. For liquids, if the incompressibility assumption is adopted, density depends only on temperature.

Specific heat is defined as the amount of heat needed to heat up a unit mass of substance by one unit of temperature. This heat can be measured either under the condition of constant

volume or constant pressure. For liquids they are identical, in SI the unit of the specific heat is [J/(kgK)].
Enthalpy for solids and liquids can be defined as

$$H = H_R + \int_{T_R}^{T} c_p dT \tag{9}$$

where T_R has been chosen as a convenient reference temperature. The enthalpy of solids and liquids is a measure of the heat content per unit mass. Therefore, at any temperature, the heat content of the specimen can be calculated from the enthalpy by taking the product of the enthalpy times the mass of the specimen. Enthalpy, according to the definition, is always a monotonic curve. The SI unit of enthalpy is [J/kg].
Heat can be transmitted by means of diffusive exchange. This mechanism of heat transfer is conduction. Heat flux is defined as the amount of heat that flows per unit time through the unit of area. The flux of heat exchanged by conduction is described by the Fourier law, which is given by the equation

$$q_i = -k \frac{\partial T}{\partial x_i} \tag{10}$$

where q_i denotes the heat flux, which is a vector with three components (in spatial directions). On the left side we have the temperature gradient and the proportionality constant k, which is the heat conductivity. The SI unit is [W/(mK)].
Viscosity describes the ability of fluids to transfer momentum by virtue of diffusion. By analogy to the Fourier law of heat conduction, the flux of momentum of the fluid is given by the equation

$$\tau_{ij} = -\mu \frac{\partial u_i}{\partial x_j} \tag{11}$$

where the proportionality constant μ is the dynamic viscosity.
The product of mass *(m)* and velocity *(v)* gives momentum, and its flux can be obtained in the following way

$$\frac{mv}{tA} = \frac{ma}{A} = \frac{F}{A} = \tau \tag{12}$$

Force *(F)* divided by the surface *(A)* on which this force acts, gives the stress *(τ)* on this surface.
Viscosity of the metal-alloy melt is always temperature dependent. For most metal alloy melts, viscosity above the liquidus temperature can be assumed constant. Between the liquidus and the solidus temperature, viscosity of the semi-solid mixture grows, slowing down and eventually blocking the flow. In SI the unit of dynamic viscosity is the pascal (Pa). Besides the dynamic viscosity, the kinematic viscosity *(v)* is often used. Kinematic and dynamic viscosities are related to one other by the equation

$$\nu = \frac{\mu}{\rho} \text{ [m}^2\text{/s]} \tag{13}$$

Fluidity threshold (CLFu) is the value of the liquid phase fraction above which the Navier–Stokes equations are applicable. The crystals nucleated in the liquid volume freely flow together with the melt.
Percolation threshold (CLFd) is the value of the liquid phase fraction below which the melt flow is absent without plastic deformation [5–6]. An explanation of the fluidity threshold and percolation threshold can be seen in Figure 1.

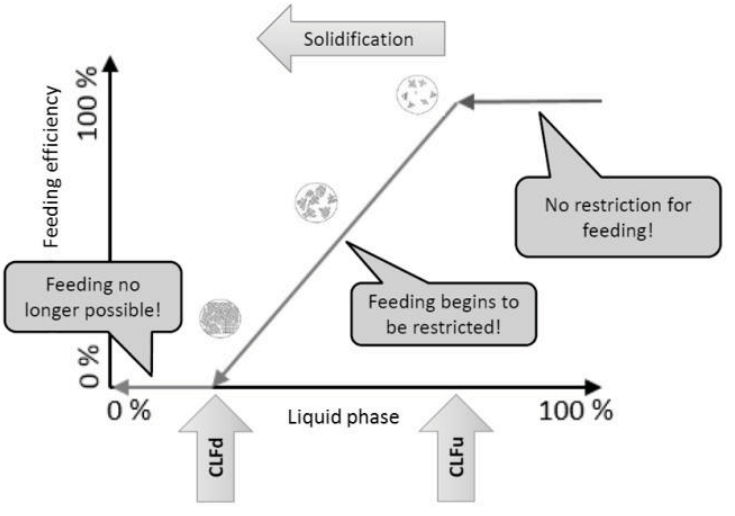

Figure 1
Explanation of the fluidity and percolation thresholds [4]

High pressure die casting (HPDC) is a manufacturing process in which molten metal injected with a die casting machine under force using considerable pressure into a steel mould or die to form products. A production cycle in HPDC consists of metal ladling, plunger movement and rapid die filling. The steel die, typically 200–300 °C, dissipates the latent heat, and during solidification the casting is pressurised hydraulically by the plunger to feed the solidification shrinkage. Locking forces up to 4,000 tons are commercially available to withstand the large pressures. Eventually, the die is opened and the casting is ejected. The hydraulic energy is provided by a computerised system that permits control of metal position, velocity and plunger acceleration to optimise the flow and the pressure during filling and solidification.
During simulation experiments the effect of the following technological parameters are examined: Piston velocity in the first phase (m/s); Piston velocity in the second phase (m/s); Temperature of the die (°C); Temperature of the melt (°C) [5, 6].

3. Specimen geometry

For the analysis of flowability a special specimen geometry is developed which is called a "meander" and can be seen in Figure 2. Total length of the specimen is 1874 mm, and the cross section of it is 50 mm^2. The 3D geometry is described by a structured cubic element mesh with a dimension of 2 mm. The total number of cells is 949,050. Initial and boundary conditions:

- alloy: EN AC-42000 [–]
- die: Steel 1.2343 [–]

- kinematic viscosity: 0.4–416 [*10 e^{-5} m^2/s]
- piston velocity, 1st phase: 0.1–1.8 [m/s]
- piston velocity, 2nd phase: 1–3 [m/s]
- die temperature: 180–240 [°C]
- pouring temperature: 586ľ650 [°C]

The experimental matrix can be seen in Table 1.

Table 1
Experimental matrix

Sign	**Alloy**	**Kinematic viscosity**	**Piston velocity**	**Piston velocity**	**Die temp.**	**Melt temp.**
		$10e^{-5}m^2/s$	1st [m/s]	2nd [m/s]	[°C]	[°C]
A	Standard EN-AC 42000	0.4	0.1	1	180	590
B	Standard EN-AC 42000	0.4	0.1	(1→) 3	(180→) 240	(590→) 650
C	SB-1	(0.4→) 416	0.1	3	240	(650→) 590
D	SB-2	(416→) 41.6	0.1	3	240	590
E	SB-3	(41.6→) 4.16	0.1	3	240	590
Sign	**Alloy**	**Kinematic viscosity**	**Piston velocity**	**Piston velocity**	**Die temp.**	**Melt temp.**
		$10e^{-5}m^2/s$	1st [m/s]	2nd [m/s]	[°C]	[°C]
F	SB-3	4.16	(0.1→)0.5	(3→)2	(240→)200	590
G	Standard EN-AC 42000	0.4(1)	(0.5→)0.1	(2→)3	(200→)150	(590→)650
H	SB-4	8.3	0.2		(15→)200	(650→)586
I	SB-4	8.3	(0.2→)1.8		200	586
J	SB-4	8.3	1.8		200	586
K	EN-AC42100	8.3	1.8		200	586

Figure 2
Meander casting part

4. Results

Filling conditions of standard alloy in mushy zone (experiment A) and in normal overheated conditions (Experiment B) can be seen in Figure 3.

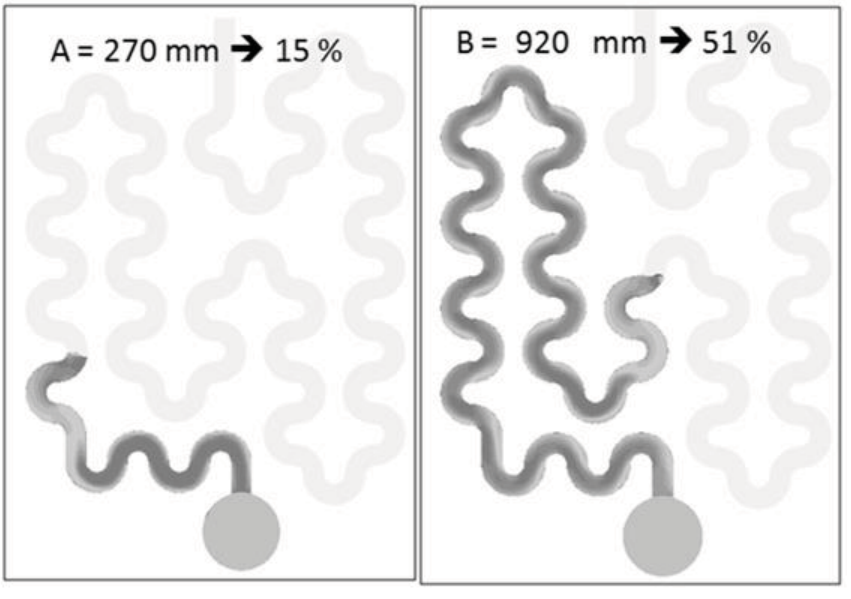

Figure 3
Filling of the specimen

In Experiment A standard EN AC-42000 alloy is calculated at 590 °C pouring temperature (between $T_{liquidus}$ and $T_{solidus}$), with 0.1 m/s and 1 m/s piston velocities for a die with the temperature of 180 °C. The calculated flow length is 270 mm, which is 15% of the total length of the specimen. The result is probably also affected by the improper position of the starting point of the 2nd phase, which is repositioned. In Experiment B a standard overheated EN-AC 42000 alloy was cast (pouring temperature: 650 °C, die temperature: 240 °C, piston velocity in the 2nd phase: 3 m/s). The flow length is 920 mm, which is 51% of the total length of the specimen. If the melt is overheated, the die temperature is increased, and the correct switching point position is achieved, the flow length can be increased by 36%.

In Experiments C, D and E semi-solid alloys were examined. Semi-solid properties were developed based on the software database: the value of kinematic viscosity was modified by the pouring temperature (416→41.6→4.16 *10⁻5 m2/s).

Based on the results of experiment E technological modifications were carried out in experiment F by changing the piston velocities and the initial temperatures are: piston velocity, 1st phase: 0.5 [m/s]; piston velocity, 2nd phase: 2 [m/s]; die temperature: 200 [°C]. With the modification the flow length can be increased by 2.3%.

The effect of the die temperature on flow length was also examined for a standard overheated alloy. By changing the values from 150 °C to 240 °C, a 9.8% increment can be achieved. Based on the results modification of the specimen geometry was implemented. The overall dimensions were kept but the cross section of the channel flow was increased from 50 mm^2 to 84 mm^2. By this geometry modification 6.26% increment can be achieved.

Conclusions

A summary of results can be seen in Table 2.

Table 2
Summary of results

Standard alloy vs. Standard alloy	Cross section	Kinematic viscosity	Piston velocity 1st phase	Piston velocity 2nd phase	Die temp.	Melt temp.	Change of flow length
	mm^2	m^2/s	m/s	m/s	°C	°C	%
A→B	–	–	↑	↑	↑	↑	–36
G→B	–	–	–	–	↑	–	+9.8
Standard alloy vs. Semi-solid alloy	Cross section	Kinematic viscosity	Piston velocity 1st phase	Piston velocity 2nd phase	Die temp.	Melt temp.	Change of flow length
	mm^2	m^2/s	m/s	m/s	°C	°C	%
A→I	–	↑	↑	↑	↑	–	–5
Semi-solid alloy vs. Semi-solid alloy	Cross section	Kinematic viscosity	Piston velocity 1st phase	Piston velocity 2nd phase	Die temp.	Melt temp.	Change of flow length
	mm^2	m^2/s	m/s	m/s	°C	°C	%
C→E	–	↓	–	–	–	–	+10.8
I→J	↑	–	–	–	–	–	+6.2

Based on the simulation results it was found that both material and technological parameters affect the flow-length properties of semi-solid high pressure die castings. Pouring temperature of the slurry and the proper temperature of the die can be determined with the help of simulation, but the exact kinematic viscosity of the poured alloy must be measured during casting. Both geometry variations of the specimen are appropriate for the investigation of the process but in our future experiments the 50 mm^2 cross-sectioned specimen will be used because the wall thickness of it is closer to real high pressure casting parts.

In future experiments casting samples will be poured and compared with the calculated results and the simulation model will be validated by the as-cast results.

References

[1] FRANKLIN, J. R.: *Squeeze casting, a review of the status*. British Foundryman, 1984.
[2] FLEMINGS, M. C.: Behavior of Metal Alloys in the Semisolid State. *Metallurgical Transactions A*, 1991.
[3] STEFANESCU, D. M.: *Science and Engineering of Casting Solidification*. Springer, 2009.
[4] LJUNG, A.: Improving prediction and the possibilities with CV technology. *NovaCast User Meeting Conference*, Gothenburg, Sweden, 2014.

[5] RATKE, L.: Effect of process parameters on properties of Al-Si alloys cast by Rapid Slurry Formation technique. *Materials Science and Engineering,* 27, 2011.
[6] HATTEL, J.: *Fundamentals of numerical modeling of casting processes*. Polyteknisk Forlag, Lyngby, Denmark, 2005.

Materials Science and Engineering, Volume 41, No.1. (2016) pp. 105-115.

THE EXAMINATION OF THE CO-PYROLYSIS OF FOOD AND WOOD I – SOLID RESIDUE

GÁBOR NAGY[1]–ÁGNES WOPERA[2]–TAMÁS KOÓS[3]

Turning solid fuels into gaseous energy sources is getting more and more important nowadays. However, some amount of solid matter always remains after such processes. Based on the pyrolysis of base materials (food waste and oak) mixed in various mass ratios it can be determined that increasing the oak ratio leads to decreased fluid formation and increased gas yield. The high carbon content of the solid residue is also the result of the increased oak ratio of the base material mixture. Hence, its utilisation as fuel and base material for gasification is possible. The same conclusion can be drawn based on the high energy value of the solid residues. These two possible utilisations are enabled by the softening properties of both the base materials and the solid residues as well.
Keywords: co-pyrolysis, char

Introduction

Beside the utilisation of solid energy sources like fossil fuels, biomass or wastes via burning, the significance of gasification is becoming more and more important in energy production. This conversion requires a significant amount of energy but has many advantages: not only the energy utilisation of the gaseous energy sources is easier and applicable on a wider scale, but the gas produced via gasification can be base material for the chemical industry as well as fuel [1].

Torrefaction, pyrolysis and gasification are the main methods of thermochemical conversion. During torrefaction, the base material is heated up to 200–300 °C to remove the moisture and volatile content and to increase the energy density of the base material. Pyrolysis is usually performed between 400–600 °C in anaerobic conditions. As a result, a significant amount of liquid matter is formed and solid matter remains in the end of the process. During gasification, the base material is transformed into gaseous energy source at high temperature, around 1000–1500 °C. Some reactants used could be air, oxygen, steam or H_2 [2].

Depending on the technology used, some amount of liquid, gaseous or solid matter is formed during all three processes. The ratio of these materials depends on the base material and the technology chosen. In many cases, the carbon content of the residual solid matter (char) is rather high. Thus further gasification is possible, it may be used as fuel or as activated carbon in gas- and wastewater cleaning systems [3].

Food wastes are typically treated as municipal wastes and disposed in Hungary, while these are composted or utilised as base material for biogas production in countries with a long history of waste recovery [4, 5]. Such processes might require weeks or months based

[1] University of Miskolc, Department of Combustion Technology and Thermal Energy
3515 Miskolc-Egyetemváros, Hungary
nagy.gabii86@gmail.com
[2] University of Miskolc, Department of Combustion Technology and Thermal Energy
3515 Miskolc-Egyetemváros, Hungary
wopera.sa@gmail.com
[3] University of Miskolc, Department of Combustion Technology and Thermal Energy
3515 Miskolc-Egyetemváros, Hungary

on the applied technology, while thermochemical processes require only hours. Thus, wastes can be converted to valuable resources in significantly less time.

Various food mixtures were pyrolised and the results revealed that these materials are appropriate for the production of good quality gaseous fuel. However, these wastes have high moisture content, typically at least 40 wt%, and are not generated in such high content, so their production is not economic. To solve this issue, supplementary base material was added to the mixtures for further experiments [6].

Based on our previous examinations, [7] woody biomasses might be the most appropriate for co-pyrolysis and the most optimal temperature should be 700 °C for pyrolysis. Our various base material mixtures were also pyrolised on 700 °C and the produced gases, fluids and solid residues were analysed. The current article consists of the analysis of only the residual pyrolysis char from the reactor.

1. Base materials and the examination method

The base material for the pyrolysis experiments was food waste and oak mixed in various mass ratios. The composition of food waste was always the same: cooked rice (25 wt%), French fries (25 wt%), fried chicken breast (25 wt%) and breaded pork chop (25 wt%). The names of the samples and their meanings are in Table 1.

Table 1
The names of the samples in the article

Name of the sample	Note
Food	Original food mixture of cooked rice (25 wt%), French fries (25 wt%), fried chicken breast (25 wt%) and breaded pork chop (25 wt%)
2 Food:1 Wood	2:1 mixture of food mixture and oak mixture
1 Food:2 Wood	1:2 mixture of food mixture and oak
Wood	Original oak
Food – 700°C	Pyrolysis char of food mixture (700 °C)
2 Food:1 Wood – 700 °C	Pyrolysis char of 2:1 mixture of food mixture and oak (700 °C)
1 Food:2 Wood – 700 °C	Pyrolysis char of 1:2 mass ratio food mixture and oak (700 °C)
Wood – 700 °C	Pyrolysis char of oak (700 °C)

An experimental reactor has been built (Figure 1) in which the pyrolysis experiments were carried out until the gas production was detectable.

The examination methods for the base materials and pyrolysis chars were the following:

Standard "*EN 14775:2010: Solid Biofuels – Determination of Ash Content*" was used to determine the ash content. The analysis was carried out in a HK-45/12 V type heating furnace with 12 kW nominal power.

The elemental composition of the samples was analysed based on Standard "*EN 15104-2011: Solid Biofuels – Determination of Total Content of Carbon, Hydrogen and Nitrogen – Instrumental Methods*" with a Carlo Erba EA 1108 elemental analyser. Program Eager 200 was used to collect and analyse the data.

Standard "*EN 14918:2009: Solid biofuels – Determination of calorific value*" was the basis of the determination of higher heating value (HHV), using a Parr 6200 type calorimeter, then in the light of certain corrections, i.e. the hydrogen or moisture content of the sample, the lower heating value (LHV) was calculated.

The softening and melting properties of the ash ware analysed with a SYLAB IF2000G type instrument a based on Standard *"CEN/TS 15370-1: 2006: Solid biofuels – Method for the determination of ash melting behaviour. Characteristic temperatures method":*

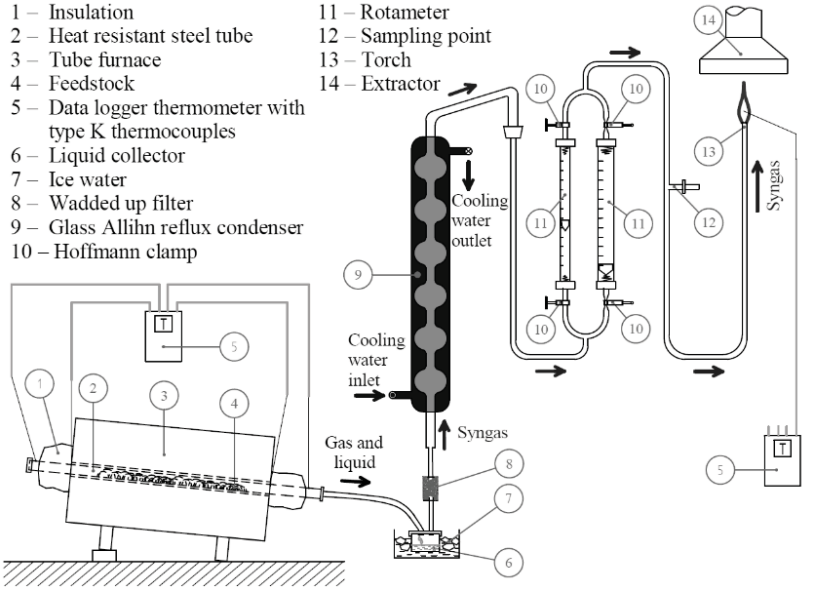

Figure 1
Schematic illustration of the experimental reactor

2. Results

2.1. Conversion of the base material

The different base materials leave the reactor partly in liquid and in gaseous form during the pyrolysis, but the ratio of the mass flows may change. Table 2 contains information on the quantity of the produced gaseous and liquid products and the remaining solid matter, while the conversion of the base material depending on the ratio of food waste and oak is illustrated in Figure 2.

Analysing the ratio of the produced materials in relation to the base materials (Figure 2) it can be determined that the wood added to the food mixture increased the gas yield and the quantity of residue char, and significantly decreased the amount of liquid produced. These values can be estimated via the first- and second-degree equations indicated in Figure 2.

Table 2
The mass ratio of the materials produced during pyrolysis (T = 700 °C)

Materials produced	**Mass ratio of the materials produced from various base materials, wt%**			
	Food	2 Food:1 Wood	1 Food: 2 Wood	Wood
Pyrolysis char	13.20	25.40	30.20	34.10
Liquid	64.01	49.95	41.96	36.42
Gas	22.79	24.65	27.84	29.48

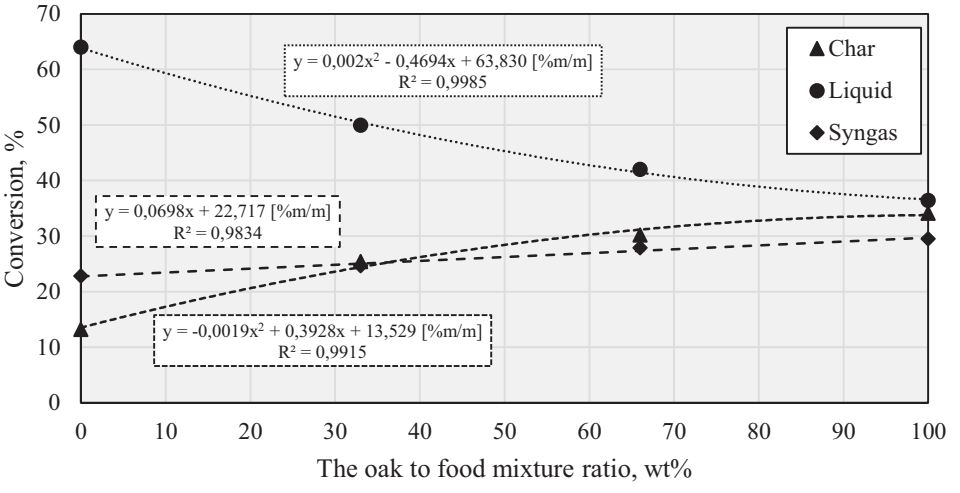

Figure 2
The ratio of the materials produced during pyrolysis (T = 700 °C) depending on the composition of the base material

2.2. The composition of the base materials and the solid residues

The comparison of the base and residue materials indicates that the carbon content of the solid residue is relatively high (Table 3). This property enables the further energetic utilisation of residues, like gasification or combustion. Furthermore, the structure of the solid residue was loose and porous (Figure 3) with high carbon and oxygen and low ash content. Therefore, these residues are suited for activated carbon production [8].

Further information can be obtained by comparing the elemental compositions of the residue char from 1 kg pyrolised base material and 1 kg base material. The carbon and oxygen contents of these are presented in Figure 4 and the nitrogen, sulphur and hydrogen content in Figure 5.

Table 3
The composition of the base materials and the remaining pyrolysis chars

Sample	Average composition of the dry samples, wt%					
	Nitrogen	Carbon	Hydrogen	Sulphur	Oxygen	Ash
Food	5.07	45.84	7.89	2.17	35.90	3.13
2 Food:1 Wood	3.22	45.98	7.33	1.45	36.98	5.04
1 Food:2 Wood	1.72	47.11	6.71	0.80	38.67	4.99
Wood	0.11	47.79	6.19	0.01	39.98	5.92
Food – 700 °C	4.61	62.92	3.51	0.45	16.45	12.06
2 Food:1 Wood – 700 °C	1.53	80.24	1.28	0.39	10.58	5.98
1 Food:2 Wood – 700 °C	0.77	79.85	2.59	0.30	10.23	6.26
Wood – 700 °C	0.17	83.49	2.43	0.32	11.99	1.60

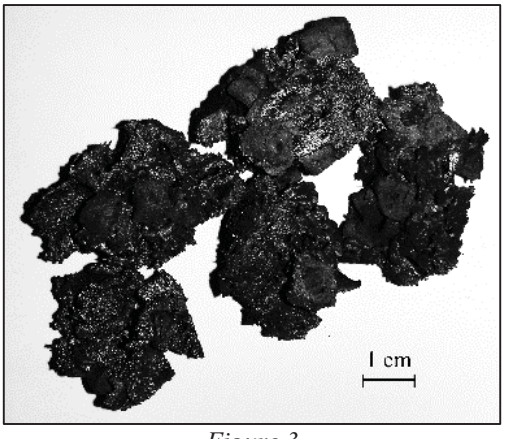

Figure 3
Photo of the char (2 Food:1 Wood – 700 °C)

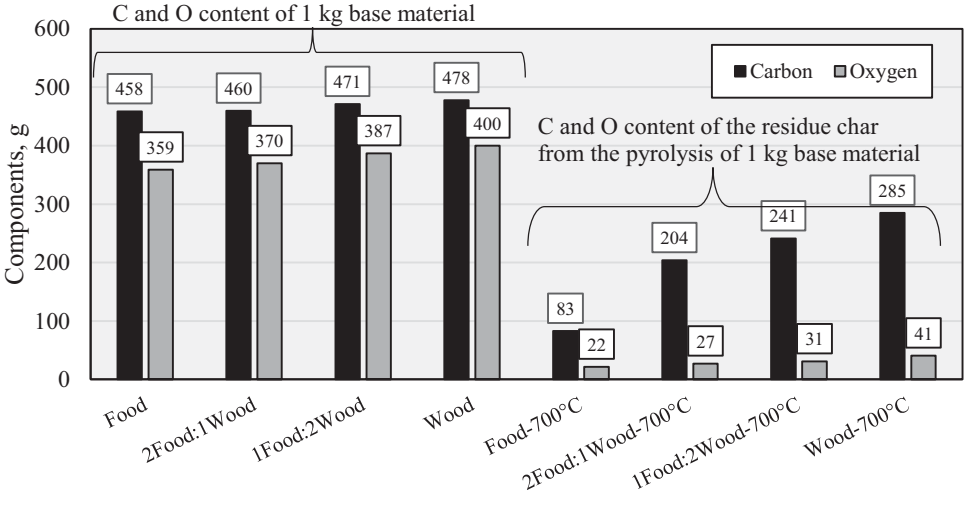

Figure 4
Carbon and oxygen content of 1 kg base material and its residue char (T = 700 °C)

The carbon and oxygen content of all four base materials are approximately the same, but the residue carbon increases in proportion to the amount of oak in the samples. This is in close relation to the facts that the carbon content of the residue char increases in proportion to the amount of oak in the base material. Moreover, the amount of the residue solid matter also increases with the amount of oak in the samples, as seen in Figure 2. The same can be stated in case of the oxygen in the residues, though, the increase ratio is not as high as in case of carbon.

The nitrogen, sulphur and hydrogen content of 1 kg base material decrease in proportion to the oak content of the base material but only a small proportion of these elements can be found in the char after pyrolysis. The low sulphur content of base materials is favourable during energy utilization.

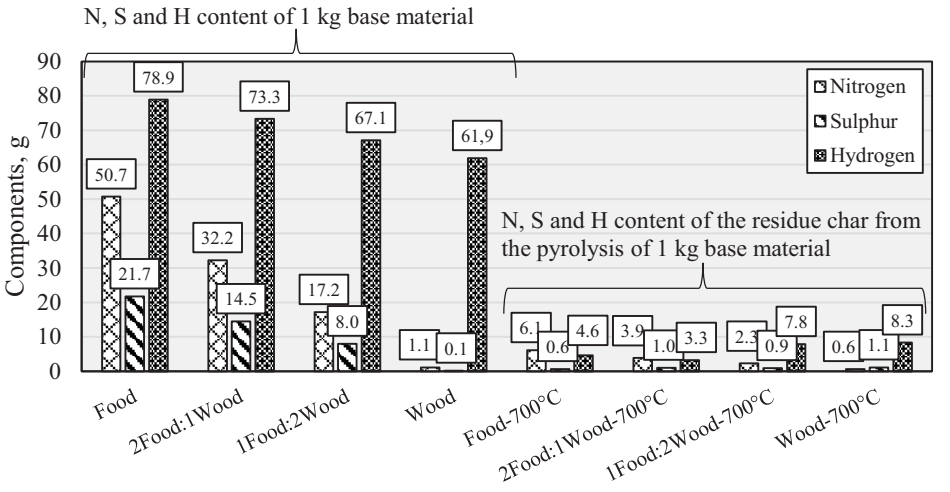

Figure 5
Nitrogen, sulphur and hydrogen content of 1 kg base material and its residue char (T = 700 °C)

2.3. Examination of the LHV

Based on the Figure 6 it can be stated that the LHVs of the char samples where higher than the LHVs of the base materials. The explanation is that the char contains relatively high amount of carbon, while the concentration of other elements is significantly low. Thus, as the carbon content is higher in the char than in the base materials, the LHV increases. Moreover, the increasing oak content of the base materials enhances the LHV as well. As the previous chapter proved, the quantity of the residue char from 1 kg base material also increases in proportion with the amount of wood. Based on these data, the heat value of the char is improved by the addition of oak.

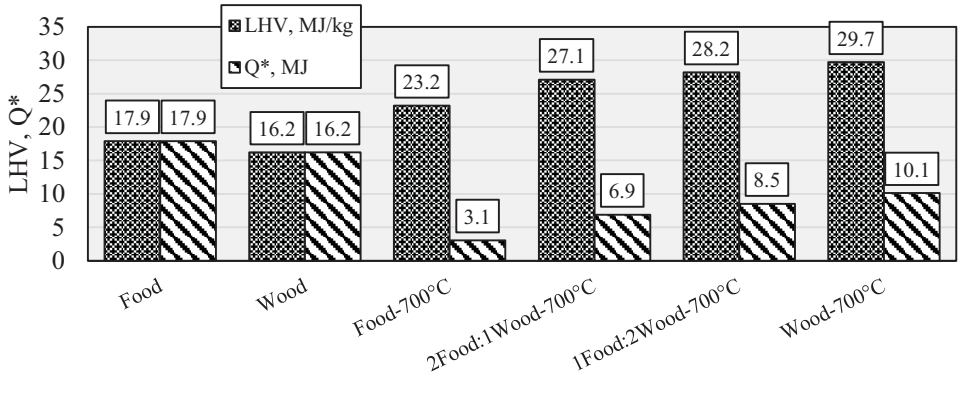

Figure 6
The LHV values and the released heat of the base materials and the residue char samples
(Q – The amount of released heat in case of the burning of 1 kg original base materials, and the amount of released heat in case of the burning of the residue char from 1 kg base material samples)*

The charting of the LHV and the energy value of the chars in relation to the composition of the base materials (Figure 7) shows that the estimation can be approximated with a second-degree equation. Thus, the estimation of the LHV of the residue char from various base materials is possible.

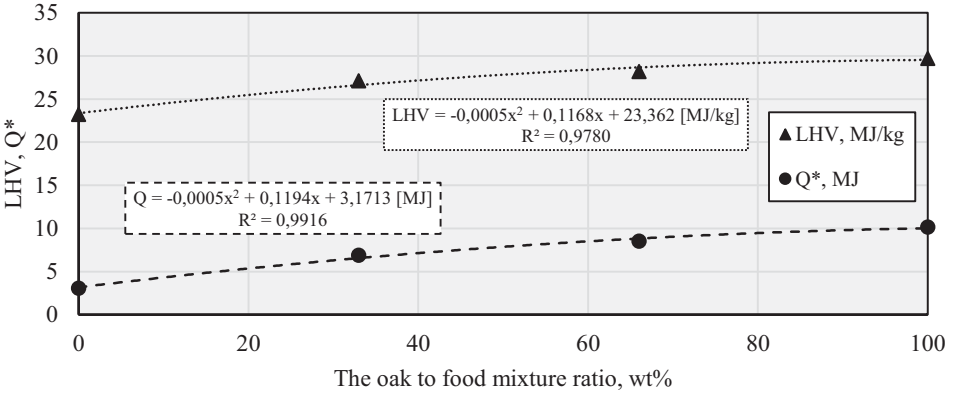

Figure 7
The LHV and the energy of the chars in relation to the composition of the base materials after pyrolysis (T = 700 °C)

Even though the LHV is more relevant in practice, data and literature on the higher heating value is more widespread [9, 10]. The HHV of the samples can be compared to various fuels in Figure 8. As the data in the various literature can be rather different, the average of these values can be found in the diagram without the exact value given. As the diagram clearly shows, the char samples are suitable for burning because the HHVs were higher than some of the already used fuels. Thus indicating the exact values was not necessary.

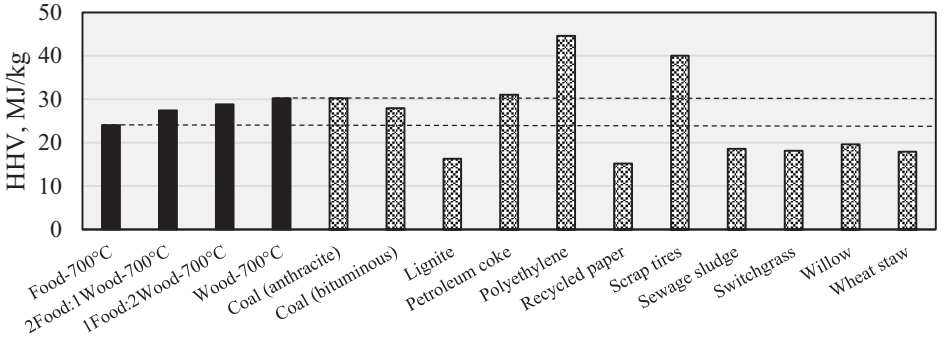

Figure 8
The char samples and some other materials used for energy recovery

2.4. The examination of the softening properties of the base materials and solid residues

The examination of the ash content revealed that the ash of the base materials has a much lighter colour than the ash of the pyrolised char samples (Figure 9) which implies that some kind of transformation takes place in the ash during pyrolysis. If these processes deteriorate

the softening properties of the ash, the utilisation of the char at high temperature might become difficult.

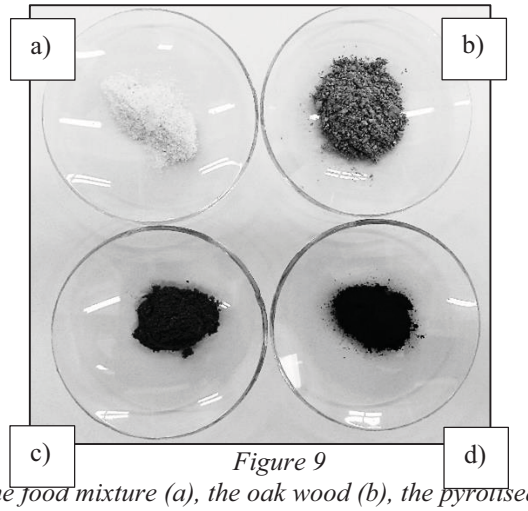

Figure 9
The ashes of the food mixture (a), the oak wood (b), the pyrolised food mixture (c) and the pyrolised oak (d)

In order to find out if any other properties of the ash change beside the colour, the softening parameters were examined. The deformation of the test bars prepared from the ash, based on standard *CEN/TS 15370-1: 2006,* because of temperature increase can be characterised with the following 5 states/temperatures (Figure 10):

1 – Original sample;
2 – Shrinkage starting temperature: the area of the test bar decreases by 5% because of sintering, the departure of CO_2 and/or volatile alkaline metals;
3 – Deformation temperature: the temperature at which the softening of the test bar seems to start, i.e. the surface is changing, the edges are getting rounded, the test bar is starting to swell. The starting temperature of the softening;
4 – Hemisphere temperature: the temperature at which the shape of the test bar resembles a hemisphere. The height of the molten test bar is the half of its diameter;
5 – Flow temperature: the temperature at which the height of the test bar is the half of the height measured at hemisphere temperature.

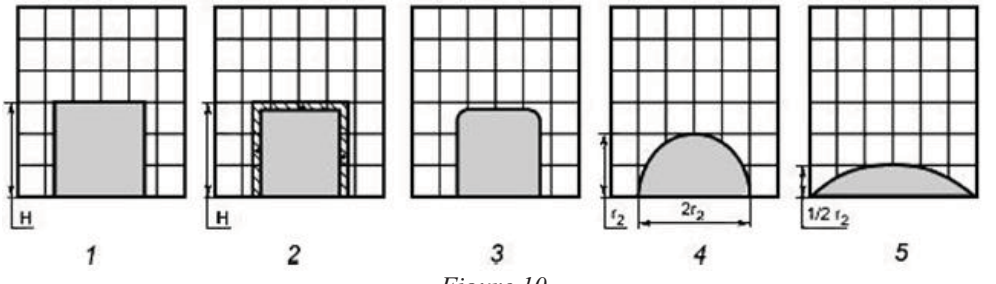

Figure 10
Phases in the ash melting process [11]
1 – Original sample; 2 – Shrinkage; 3 – Deformation; 4 – Hemisphere; 5 – Flow

Figure 11 illustrates the deformations of the test bars made out of the ashes of the original base materials and char samples, while Table 4 and 5 show the characteristic temperatures that can be found in the standard.

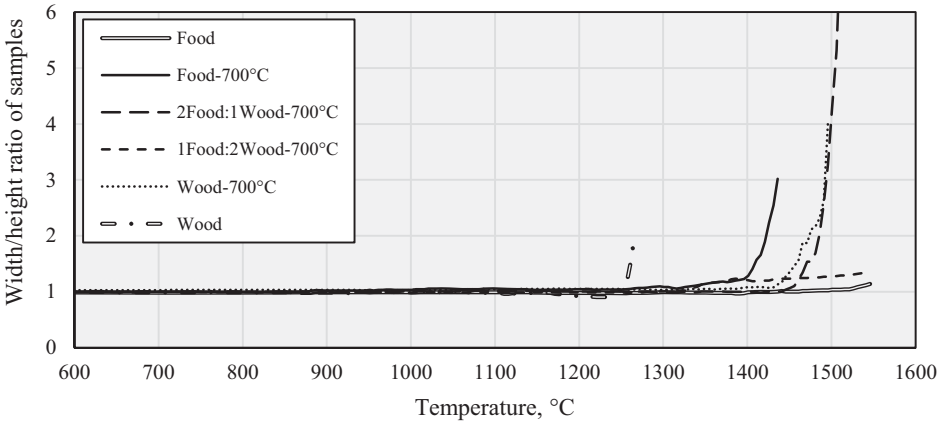

Figure 11
The width/height ratio of the ash test bars in relation to the temperature

The analysis of the width/height ration of the test bars showed (Figure 11) that the softening of the ash of the Wood sample had the lowest and the ash of the Food sample had the highest softening temperature. The softening properties of all the other residue samples were between these two temperatures.

Table 4
The properties of the ash of the original and pyrolised food mixture and oak

Properties	**Food**	**Food – 700 °C**	**Difference from the original**	**Wood**	**Wood –700 °C**	**Difference from the original**
Shrinkage starting temperature, °C	1396	1321	–75	1221	1192	–71
Deformation temperature, °C	1420	1263	–157	1076	1264	+188
Hemisphere temperature, °C	>1546	1423	>–123	1270	1472	+202
Flow temperature, °C	>1546	>1436	–	>1276	>1496	–

The comparison of the data from Table 4 reveals that the starting temperature of the sintering of the ash decreased a bit because of the pyrolysis. The deformation of the ash from the pyrolised food mixture started 157 °C lower than the deformation of the ash of the food mixture. On the other hand, the deformation of the ash of the oak started at a lower temperature in case of the original ash, not the pyrolised sample. This can also be observed at the hemisphere temperature. The flow temperature was too high to determine with our current equipment in all cases.

According to the analysis of the ash of the pyrolised materials (Table 5), sample "*1 Food:2 Wood – 700 °C*" was the first material to sinter, at 1071 °C, and to soften as well, at 1253 °C, latter of which temperature is too high to utilise the char by burning or gasification without causing problems in the system with the ash softening.

Table 5
The softening properties of the ashes of the pyrolised materials

Properties	Food – 700 °C	2 Food: 1Wood – 700 °C	1 Food: 2 Wood – 700 °C	Wood – 700 °C
Shrinkage starting temperature, °C	1321	1341	1071	1192
Deformation temperature, °C	1263	1450	1253	1264
Hemisphere temperature, °C	1423	1485	1526	1472
Flow temperature, °C	>1436	1508	>1546	>1496

The charting of the data from Table 5 can be observed in Figure 12.

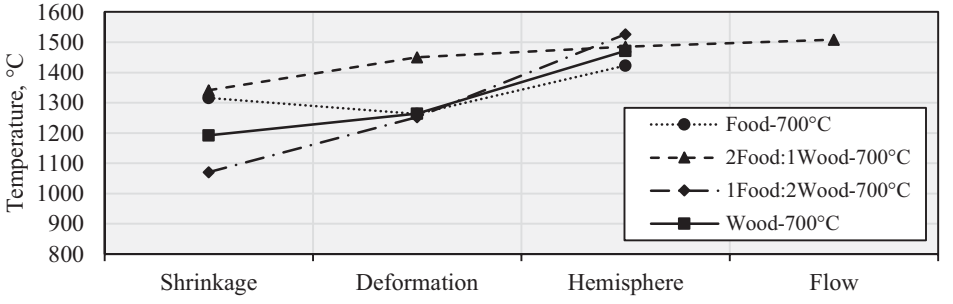

Figure 12
The softening temperature of the ashes of the pyrolised mixtures

Conclusions

The examination of oak and food waste mixtures in various mass ratios before and after pyrolysis at 700 °C shows that the conversion ratio of the base material decreases with the addition of oak, as the amount of solid residue is higher. Decreasing the ratio of oak resulted in less liquid and more gas production. The quantity of solid, liquid and gaseous products can be estimated based on the ratio of the base materials using first- and second degree equations.

The carbon content of the residue solid matter is relatively high after pyrolysis and increases with the higher ratio of the oak added to the base material. Furthermore, the char can be utilised not only as base material for gasification or energy recovery because of the high oxygen, low ash and sulphur content, but for activated carbon production as well.

The possibility of the usage for energy recovery was supported by the results of the LHV tests. A function was developed to estimate the LHV of the residue material of the pyrolysis of the mixture and another to determine the energy of the char from the pyrolysis of 1 kg base material, depending on the food mixture/oak mass ratio.

The examination of the softening properties of the ash of the original materials and pyrolysis chars showed that most of the characteristic temperatures are decreased by pyrolysis. Still, these temperatures are within such temperature range, that the softening of the ash should not cause any problems during neither gasification, nor burning.

Acknowledgement

This research was carried out in the framework of the Center of Excellence of Sustainable Resource Management at the University of Miskolc.

This research was supported by the European Union and the State of Hungary, co-financed by the European Social Fund in the framework of TÁMOP-4.2.4.A/ 2-11/1-2012-0001 'National Excellence Program'.
The authors are grateful to Mária Ambrus for her advice.

References

[1] BASU, P.: *Biomass Gasification, Pyrolysis and Torrefaction: Practical Design and Theory.* Second Edition. Elsevier Inc., Burlington, 2013.
[2] BATHOLY, J.–BREUER, H.–PIECZKA, I.–PONGRÁCZ R.–RADICS K.: *Megújuló energiaforrások.* 2013.
[3] REZAIYAN, J.–CHEREMISINOFF, N. P.: *Gasification Technologies: A Primer for Engineers and Scientists.* CRC Press, 2005.
[4] ROSENWINKEL, K-H.–KROISS, H.–DICHTL, N.–SEYFRIED, C-F.–WEILAND, P: *Anaerobtechnik. Abwasser-, Schlamm- und Reststoffbehandlung, Biogasgewinnung. 3. Auflage*. Springer Verlag, Berlin–Heidelberg, 2015.
[5] MONIER, V.–MUDGAL, S.–ESCALON, V.–O'CONNOR, C.–GIBON, T.–ANDERSON, G.–MONTOUX, H.–REISINGER, H.–DOLLEY, P.–OGILVIE, S.–MORTON, G: *Preparatory study on food waste across EU 27.* Technical Report. European Commission, 2011.
[6] NAGY G.–WOPERÁNÉ SERÉDI Á.: Élelmiszerhulladékok energetikai hasznosítása. *Magyar Energetika,* 2014. 4. szám, 36–39.
[7] NAGY G.–KOÓS T.–WOPERÁNÉ SERÉDI Á.–SZEMMELVEISZ T.: Ételmaradékok kigázosításához kiegészítő alapanyag választása termoanalitikai vizsgálatok alapján. *Anyagvizsgálók Lapja*, 2014, 1–2. szám, 33–40.
[8] LÁSZLÓ, K.–BOTA, A.–NAGY, L. G.: Comparative adsorption study on carbons from polymer precursors. *Carbon*, Vol. 38, No. 14 (2000), 1965–1976.
[9] LACKNER, M.–WINTER, F.–AGARWAL, A. K.: *Handbook of Combustion.* Wiley–VCH, 2010.
[10] DEMIREL, Y.: *Energy – Production, Conversion, Storage, Conservation, and Coupling*. Springer, 2012.
[11] *CEN/TS 15370-1: Solid biofuels. Method for the determination of ash melting behaviour. Characteristic temperatures method.* 2006.

Materials Science and Engineering, Volume 41, No. 1 (2016) pp. 116–126.

THE EXAMINATION OF THE CO-PYROLYSIS OF FOOD AND WOOD II – SYNGAS

GÁBOR NAGY[1]–ÁGNES WOPERA[2]

The thermochemical conversion of solid materials is getting more and more important nowadays, the product or by-product of which is syngas containing carbon monoxide and hydrogen. The procedure for our experiments was pyrolysis, during which the determination of the possible uses of the produced gas from base materials (food waste and oak) mixed in various mass ratios was the aim.
According to the experiment, the increased oak content of the food-wood mixture increases the carbon monoxide content of the syngas and reduces its carbon dioxide content. Based on the H_2/CO ratio, the composition of the produced syngas might be suitable for acetic acid and acetic anhydride production. In case the syngas is not for the chemical industry, the analysis of its heat value is also necessary. According to the analyses, the produced syngas is highly suitable to be used as fuel. The adiabatic flame temperature of the syngas produced during the experiment was often higher in most cases than in case of an ordinary natural gas.
Keywords: pyrolysis, syngas utilisation

Introduction

Syngas is a gas mixture typically produced via gasification or pyrolysis. One of the main parameters of syngas is the H_2/CO ratio.

Table 1
The necessary H_2/CO ratios for the products made out of syngas

Product	Basic chemical reactions	H_2/CO ratio
FT liquid fuels	$2n\ H_2 + n\ CO \rightarrow C_nH_{2n} + n\ H_2O$ $(2n+1)\ H_2 + n\ CO \rightarrow C_nH_{2n+1} + n\ H_2O$	2.0 2.1
Methanol	$2\ H_2 + CO \rightarrow CH_3OH$	2.0
Ethanol	$2\ CO + 4\ H_2 \rightarrow C_2H_5OH + H_2O$	2.0
Higher alcohols	$n\ CO + 2n\ H_2 \rightarrow C_nH_{2n+1}OH + (n–1)\ H_2O$	2.0
Dimethyl ether	$2\ CO + 4\ H_2 \rightarrow CH_3OCH_3 + H_2O$	2.0
Acetic acid	$2\ CO + 2\ H_2 \rightarrow CH_3COOH$	1.0
Ethylene	$2\ CO + 4\ H_2 \rightarrow C_2H_4 + 2\ H_2O$	2.0
Ethylene glycol	$2\ CO + 3\ H_2 \rightarrow C_2H_6O_2$	1.5
Acetic anhydride	$4\ CO + 4\ H_2 \rightarrow (CH_3CO)_2O + H_2O$	1.0
Ethyl acetate	$4\ CO + 6\ H_2 \rightarrow CH_3COOC_2H_5 + 2\ H_2O$	1.5
Vinyl acetate	$4\ CO + 5\ H_2 \rightarrow CH_3COOCHCH_2 + 2\ H_2O$	1.25

Depending on whether syngas production is the aim of the fuel-conversion process [1, 2, 3] or it is only a by-product and what the gasified/pyrolised base material is [4, 5, 6], the composition and the possible utilisation can be rather different. For example, for energy recovery purposes high hydrocarbon content is necessary, while to use it as base material for

[1] University of Miskolc, Department of Combustion Technology and Thermal Energy
3515 Miskolc-Egyetemváros, Hungary
nagy.gabii86@gmail.com
[2] University of Miskolc, Department of Combustion Technology and Thermal Energy
3515 Miskolc-Egyetemváros, Hungary
wopera.sa@gmail.com

the chemical industry high hydrogen and carbon monoxide content is needed. Table 1 demonstrates some of the possible products made out of syngas, based on the H_2/CO ratio [7].

The current article should be considered as the continuation of the article titled "*The Examination of the Co-Pyrolysis of Food and Wood I – Solid Residue*". However, the main focus of this article is the analysis of the syngas produced during the experiments. The base materials, which were chosen based on our previous examinations [8], were pyrolised on 700 °C. The results were used to evaluate the possible utilisations of the syngas.

1. Base materials and the examination method

The detailed description of the base materials and the experimental reactor can be found in the article "*The Examination of the Co-Pyrolysis of Food and Wood I – Solid Residue*" of the current issue. The names of the samples and their meanings can be found in Table 2.

Table 2
The names of the samples in the article

Name of the sample	Explanation
Food	Original food mixture (25wt% cooked rice, 25wt% French fries, 25wt% fried chicken breast and wt25% breaded pork chop)
Wood	Original oak
2 Food:1 Wood	2:1 mixture of Food and Wood
1 Food:2 Wood	1:2 mixture of Food and Wood

The quantity of the gas produced by our system was examined with a Medingen type rotameters (the measurement ranges are 3–30 and 20–260 l/h). As the amount of syngas produced depends on the weight of input material, the l/h unit was converted into l/kg.

The gas composition was determined with a Dani Master GC device, equipped with a TCD detector and an S/SL injector. The following 3 columns connected in series were used for the separation of gas components: Rt-Q-bond (15 m x 0.53 mm x 20 µm), Rt-Q-bond (30 m x 0.32 mm x 10 µm) and Rt-Msieve 5A (30 m x 0,53 mm x 50 µm).

The lower heating value (LHV) of the gas mixtures was calculated using the LHVs of each component found in literature (Table 3 [9, 10]) and the measured concentrations.

Table 3
LHVs of the components

Components	LHV, MJ/m^3	HHV, MJ/m^3
Methane	35.949	39.887
Ethane	64.615	70.558
Ethylene	59.571	63.549
Carbon monoxide	12.680	12.609
Hydrogen	10.826	12.796

The adiabatic flame temperature (T_{max}) of each gas sample was calculated with the LHVs of the components, the specific heat from the literature [11] and the combustion equations [12] taken into consideration.

The determination of the moisture content was based on "*EN 14774:2009: Solid biofuels. Determination of moisture content – Oven dry method*" standard with a Mettler Toledo HB43-S instrument.

2. Results

2.1. The quantity of the produced syngas

The dry syngas production over time can be observed in Figure 1.

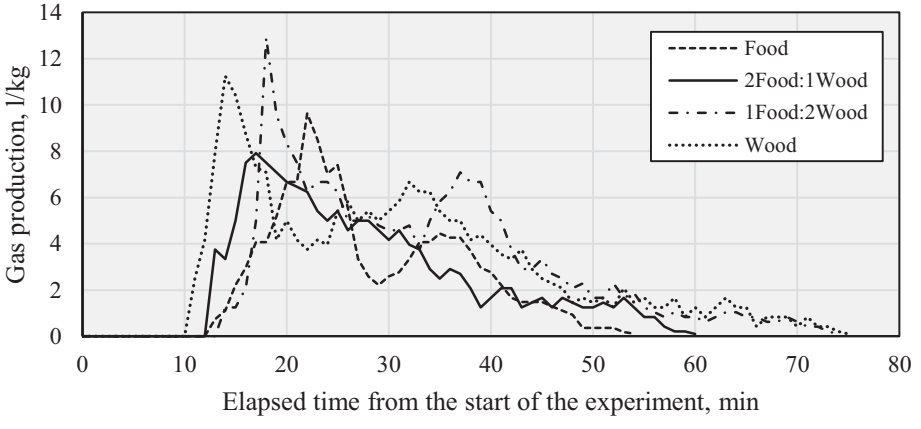

Figure 1
The dry syngas production over time

The comparison of 1 kg of each sample pyrolised under the same conditions revealed that the gas production of the food mixture starts later and ends sooner, and the peak intensity of the gas production can also be expected later than in case of any other samples. The reason for this is the approximately 50 w/w% moisture content (Table 4). The first process of pyrolysis is the drying of the base material. The moisture generated condenses in a liquid collector and a cooler inside the reactor which makes the examination of the dry gas possible. Then the production of syngas starts. The moisture content of the oak sample was the lowest (Table 4) so the gas production started first, and lasted the longest because of the high dry matter content. The specific gas yield (Figure 2) was the highest in case of the oak, and the lowest in case of the food mixture sample. The gas yield of the mixed base materials increased in proportion to the amount of oak in the samples (Figure 3).

Table 4
The moisture and dry matter content of the base materials

Sample	Moisture content, m/m%	Dry matter content, m/m%
Food	49.26	50.74
Wood	5.92	94.08
2 Food:1 Wood	34.47	65.53
1 Food:2 Wood	20.16	79.84

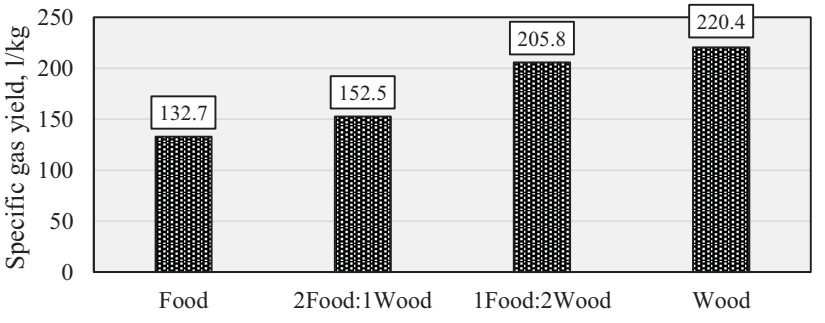

Figure 2
The specific gas yield of the pyrolysis (T = 700 °C)

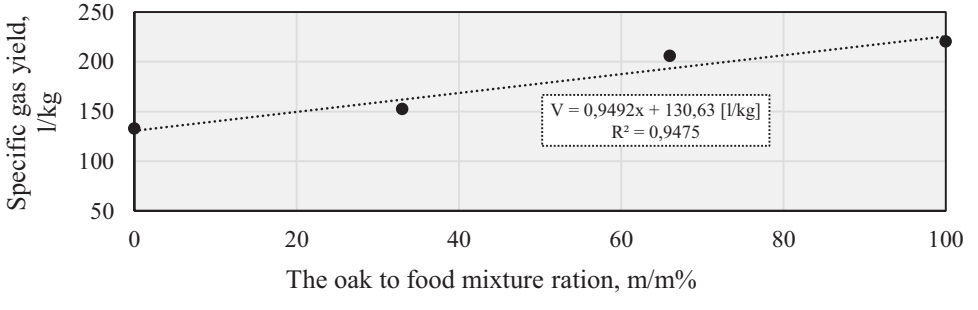

Figure 3
The specific gas yield of the pyrolysis (T = 700 °C) in relation to the composition of the base material

2.2. The composition of the produced syngas

The gas chromatograph used is capable of the analysis of CO, CO_2, O_2, N_2, H_2, H_2O, H_2S, NH_3, CH_4, C_2H_4 and C_2H_6 at the same time. The main focus of our experiment is the main examination of the components of syngas, namely CO, H_2, CO_2 and C_xH_y – in our case this includes CH_4, C_2H_4 and C_2H_6. Figures 4–7 show the changes in the gas composition during pyrolysis.

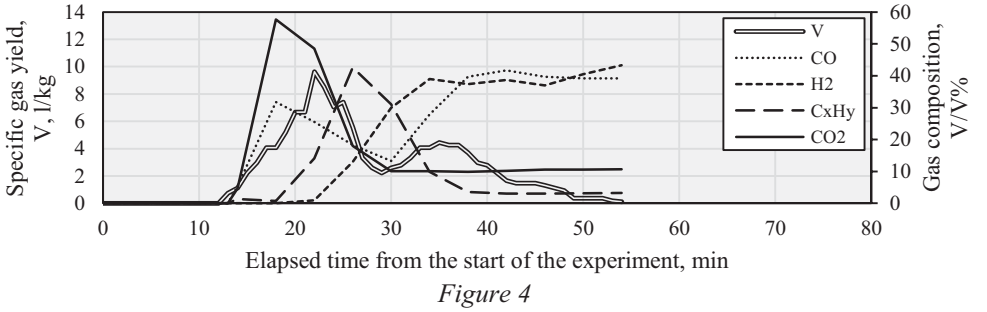

Figure 4
The specific gas yield and the gas composition during pyrolysis (Food – 700 °C)

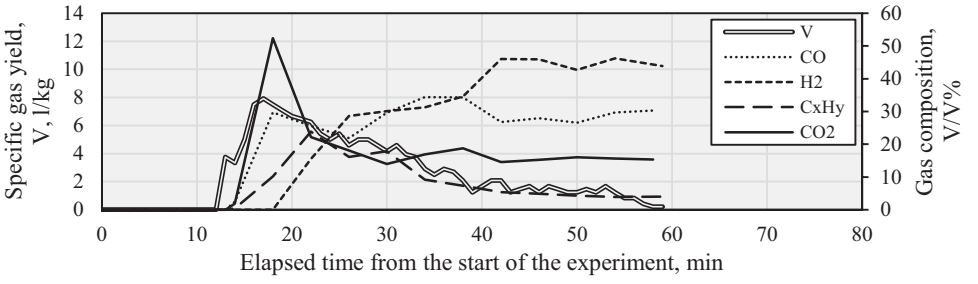

Figure 5

The specific gas yield and the gas composition during pyrolysis (2 Food:1 Wood – 700 °C)

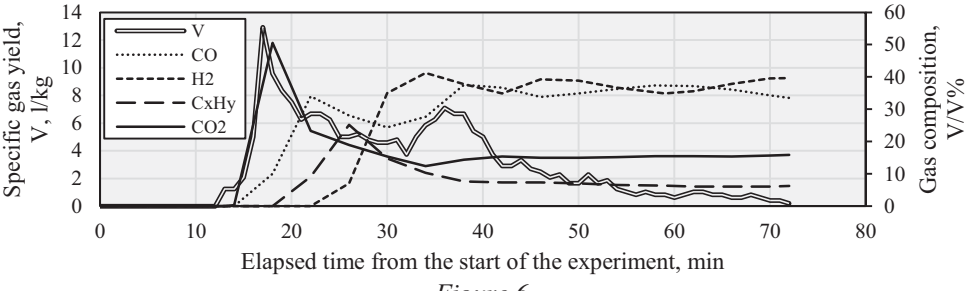

Figure 6

The specific gas yield and the gas composition during pyrolysis(1 Food:2 Wood – 700 °C)

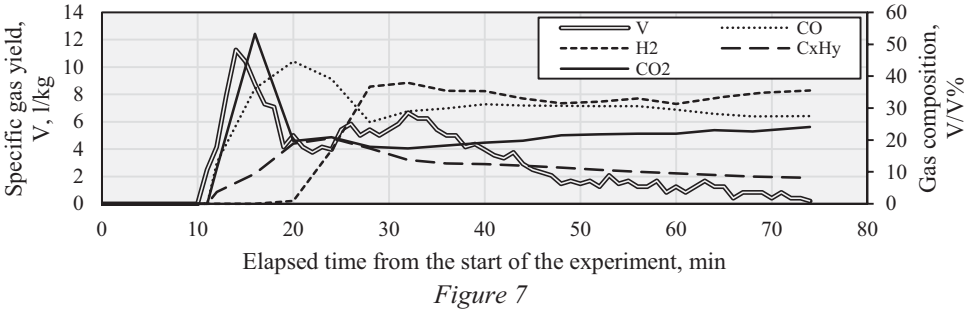

Figure 7

The specific gas yield and the gas composition during pyrolysis (Wood – 700 °C)

The changes of specific gas yield and gas composition had the same tendency during the experiments. As there was some air in the reactor, first, the carbon dioxide concentration started to increase. As the quantity of air decreased in the reactor, the concentration of the hydrocarbons, the carbon monoxide and then the hydrogen. Achieving the highest amount of hydrocarbons results in decreasing carbon monoxide content. As the amount of hydrocarbons starts to decrease, the amount of carbon monoxide starts to increase in the gas mixture with the hydrogen concentration also increasing. Finally, the different components reach a constant value and stay at that value till the end of the gas production.

Analysing the composition of the produced gas in relation to the specific gas production per minute (Figure 8) it can be concluded that the addition of wood to the mixture increases

the carbon monoxide and hydrogen content but decreases the carbon dioxide and hydrocarbon content. Comparing the examined samples (Food, 2 Food:1 Wood, 1 Food:2 Wood, Wood), the syngas with the highest hydrogen and carbon monoxide content (Figure 9) can be achieved if the base material contains more oak than food mixture, in 66,5/33,5 m/m% ratio.

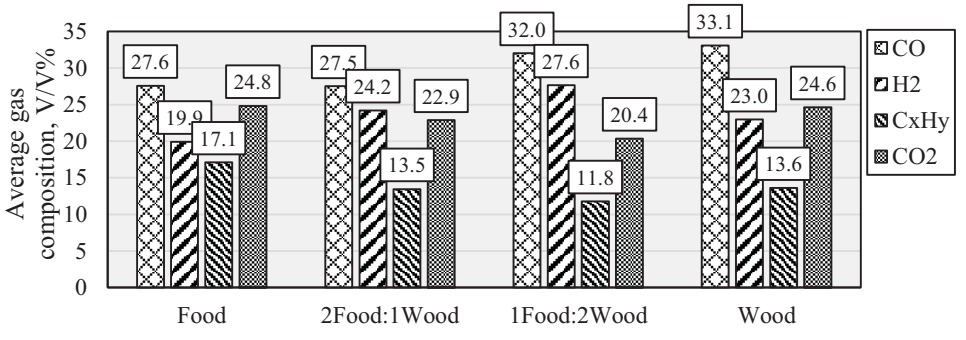

Figure 8
Average composition of the gas produced via pyrolysis (700 °C)

The H_2/CO ratios can be seen in Table 5, based on the average gas composition (Figure 8). The comparison of these with Table 1 reveals that the H_2/CO ratio is too low for the optimal operation of any of the listed chemical processes, so the extra hydrogen should be added which opens up the possibility of more problems, like increasing costs or applying further technologies.

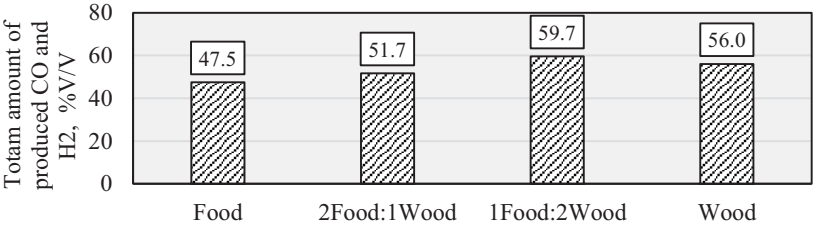

Figure 9
The sum of the hydrogen and carbon monoxide content of the syngas

Table 5
The H_2/CO ratios in case of average gas composition

Base material	H_2	CO	H_2/CO
Food	19.90	27.57	0.72
Wood	22.96	33.08	0.69
2 Food:1 Wood	24.20	27.50	0.88
1 Food:2 Wood	27.63	32.03	0.86

The solution to the presented problem might be the separation of the hydrocarbon-lean and -rich syngas by diverting the gas after the hydrocarbon content is decreasing. The execution of this procedure is only possible if the gas composition is continuously monitored. In our

case, the gas was sampled every 3 minutes. The gas yield after the sample with the highest hydrocarbon concentration is considered hydrocarbon-lean. Based on this concept, which is explained in more detail through an example in Figure 10, the division of the specific gas yield is shown in Figure 11.

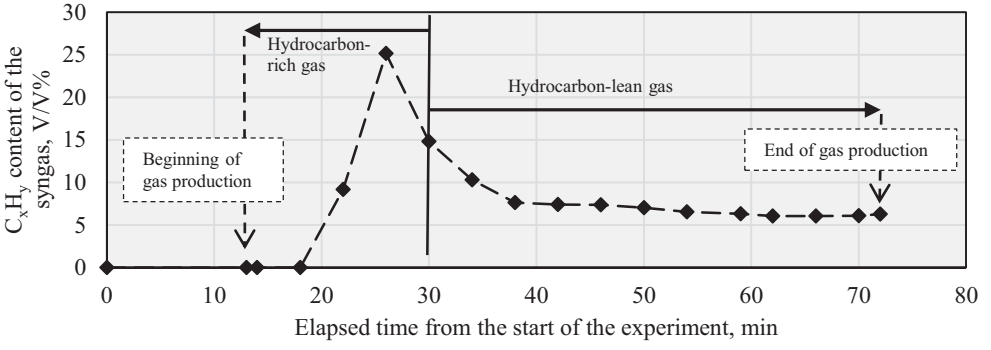

Figure 10
Explanation of the concepts of hydrocarbon-lean and -rich syngas (example: 1 Food:2 Wood – 700 °C)

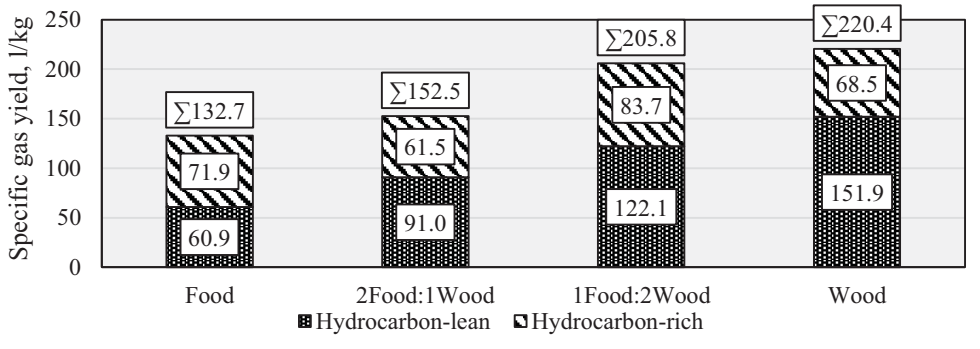

Figure 11
Specific gas yields during pyrolysis (700 °C)

Based on Figure 9, the H_2/CO ratio of the hydrocarbon-lean portion of the syngas (Table 6) was between 1.06 and 1.13 which are near the appropriate ratio for acetic acid and acetic anhydride production The hydrocarbon-rich portion can be used to partly cover the technological heat demand.

Table 6
The H_2/CO ratios in the hydrocarbon-lean portion of the syngas

Base material	H_2	CO	H_2/CO
Food	36.86	32.54	1.13
Wood	33.13	30.27	1.09
2 Food:1 Wood	40.53	38.20	1.06
1 Food:2 Wood	37.81	34.70	1.09

2.3. The LHVs, HHVs and the adiabatic flame temperatures

The LHV and HHV of the syngas can be calculated from the instantaneous gas composition and the LHVs and HHVs of the components. The LHVs of the syngas produced from oak and base materials containing oak and the LHVs of all the gas produced during pyrolysis have similar tendencies (Figure 12 and Figure 14). On the other hand, the pyrolysis of the food sample resulted in gas with higher LHV (Figure 14). The same tendencies can be observed in case of the HHVs (Figure 13 and Figure 14). Due to the more than 40 V/V% hydrocarbon content, the LHVs and HHVs of the gas mixtures produced from *Food* sample had a peak in the first phase of pyrolysis (Figure 12 and Figure 13).

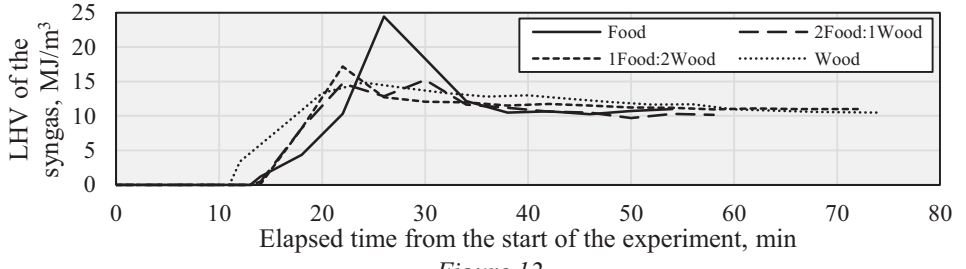

Figure 12
The LHV of the syngas over time

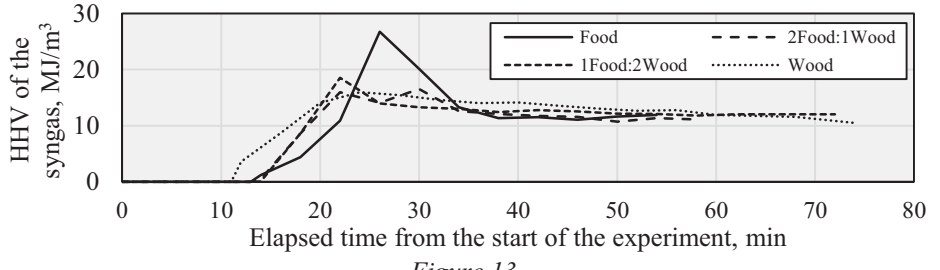

Figure 13
The HHV of the syngas over time

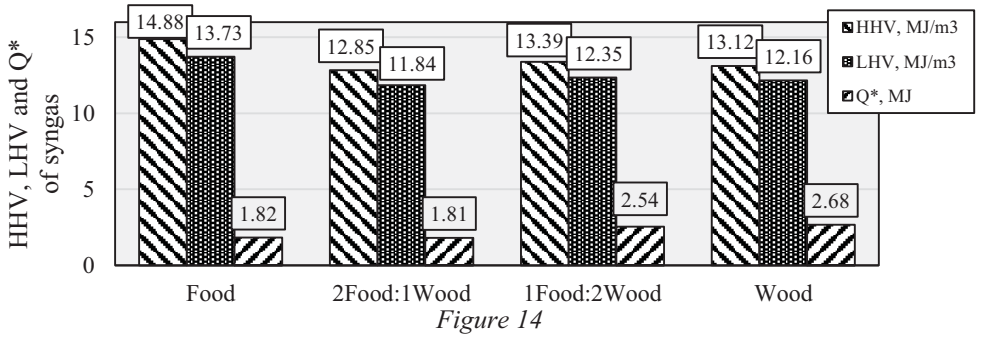

Figure 14
The LHV, HHV of the gas produced from the base materials and the energy yield of 1 kg base material (Q)

The LHV of all gas produced from the food sample (Figure 14) was the highest, but the energy yield of 1 kg base material lacks behind the energy yield of the other three samples. The reason for this is that the amount of gas produced was lower in case of the pyrolysis of the food sample.

Once the hydrocarbon-rich and -lean gases are separated (Figure 15 and 16) it can be seen that the LHVs and HHVs of hydrocarbon-rich mixtures are higher than the LHVs and HHVs of hydrocarbon-lean mixture. This confirms that two types of gases should be separated.

Based on the examination of the energy yield by the pyrolysis of 1 kg base material (Figure 17), the quantity of hydrocarbon-lean gas is increasing with the addition of oak and the amount of hydrocarbon-rich mixture is decreased, except sample 1 Food:2 Wood.

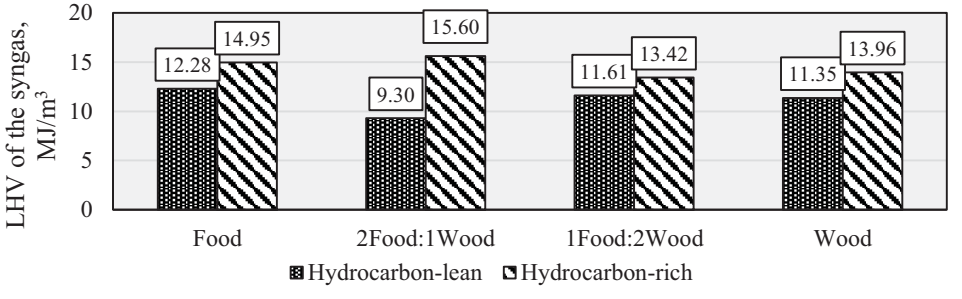

Figure 15
The LHVs of the hydrocarbon-lean and -rich syngas

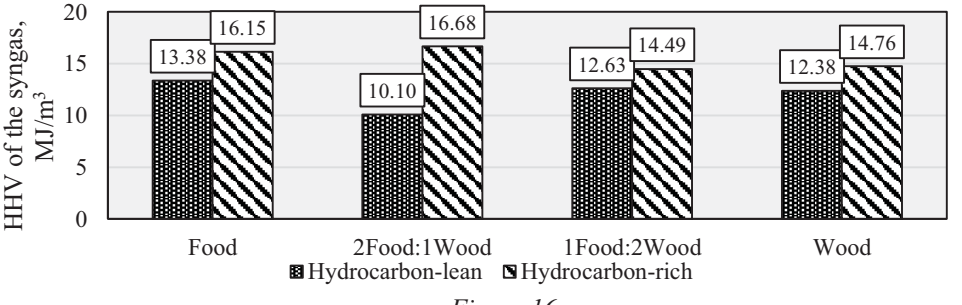

Figure 16
The HHVs of the hydrocarbon-lean and -rich syngas

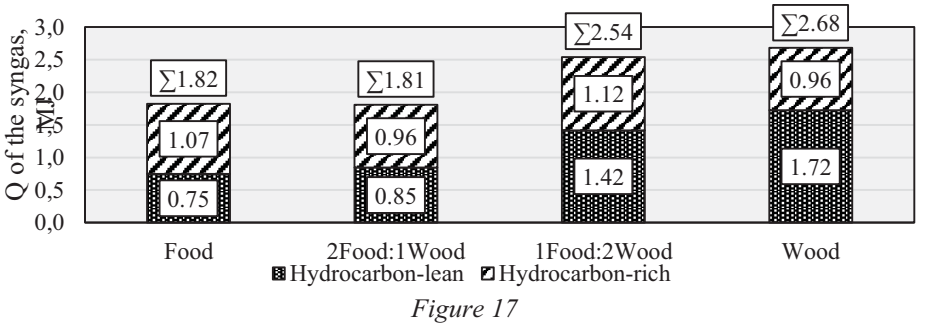

Figure 17
The energy yield of 1 kg base material

After comparing the calculated adiabatic flame temperatures of the samples and the values of an average composition natural gas (CH_4 = 97%V/V, C_xH_y = 1,5%V/V, inert = 1,5%V/V) it can be observed that the flame temperature of our samples were often higher (Figure 18). Thus, they can be used for energy recovery.

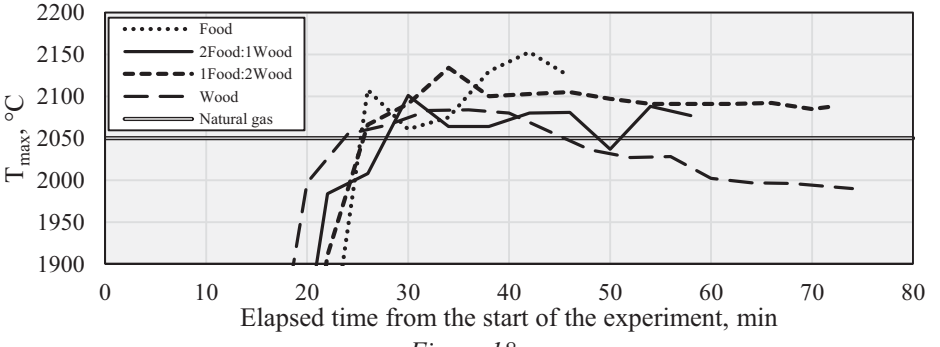

Figure 18

The changes of adiabatic flame temperature of the samples over time compared to a typical natural gas sample

Conclusions

The results of the analysis of the syngas produced via the pyrolysis of the various base materials on 700 °C indicate that the higher the oak to food ratio was, the higher the specific gas yield was. The approximation of this correlation can be described with a first-grade equation.

The composition of the base material has an impact on the composition of the produced gas as well. Increasing the oak to food ratio result in the increase of carbon monoxide and the decrease of the carbon monoxide content. Sample 1 Food:2 Wood had the highest hydrogen and lowest hydrocarbon content. The H_2/CO ratio of the syngas was around 0.8 which is not high enough to utilise the gas as a base material for any kind of chemical process. However, this ratio can be increased if the hydrocarbon-rich gas mixture produced in the beginning of the pyrolysis is utilised by burning and only the hydrocarbon-lean gas mixture, which is rich in carbon monoxide and hydrogen, is used as base material for the chemical industry. Thus, the H_2/CO ratio can be increased to approximately 1:1. This ratio means the syngas is suitable for acetic acid and acetic anhydride production.

The food mixture pyrolised on 700 °C had the highest LHV, but the least energy is released from this in relation to 1 kg base material as the lowest quantity of gas is produced from this base material. The separation of the hydrocarbon-rich and -lean gas mixture might be advantageous in case of the LHVs, as the samples with high hydrocarbon content had higher LHVs than the whole gas mixture.

Based on the calculated adiabatic flame temperature of each gas sample, the temperature of the syngas produced was higher in most cases than the temperature of natural gas.

Acknowledgement

This research was carried out in the framework of the Center of Excellence of Sustainable Resource Management at the University of Miskolc.

This research was supported by the European Union and the State of Hungary, co-financed by the European Social Fund in the framework of TÁMOP-4.2.4.A/ 2-11/1-2012-0001 'National Excellence Program'.
The authors are grateful to Mária Ambrus for her advice.

References

[1] TRIPATHI, M.–SAHU, J. N.–GANESAN, P.: Effect of process parameters on production of biochar from biomass waste through pyrolysis: A review. *Renewable and Sustainable Energy Reviews,* 55 (2016), 467–481.
[2] PAPARI, S.–HAWBOLDT, K.: A review on the pyrolysis of woody biomass to bio-oil: Focus on kinetic models. *Renewable and Sustainable Energy Reviews,* 52 (2015), 1580–1595.
[3] ZHANG, S.–DONG, Q.–ZHANG, L.–XIONG, Y.: High quality syngas production from microwave pyrolysis of rice husk with char-supported metallic catalysts. *Bioresource Technology,* 191 (2015), 17–23.
[4] SHARUDDIN, S. D. A.–ABNISA, F.– DAUD, W. M. A. W.–AROUA, M. K.: A review on pyrolysis of plastic wastes. *Energy Conversion and Management,* 115 (2016), 308–326.
[5] MARTÍNEZ, J. D.–PUY, N.–MURILLO, R.–GARCÍA, T.–NAVARRO, M. V.–MASTRAL, A. M.: Waste tyre pyrolysis – A review. *Renewable and Sustainable Energy Reviews,* 23 (2013), 179–213.
[6] WHITEA, J. E.–CATALLO, W. J.–LEGENDREA, B. L.: Biomass pyrolysis kinetics: A comparative critical review with relevant agricultural residue case studies. *Journal of Analytical and Applied Pyrolysis* 91 (2011), 1–33.
[7] CALABRESE, P. A.–BAI, D.: Engineered fuel feed stock useful for displacement of coal in coal firing plants. *Patent application*. WO2009158539 A1. 2009. 12. 30.
[8] NAGY G.–KOÓS T.–WOPERÁNÉ SERÉDI Á.–SZEMMELVEISZ T.: Ételmaradékok kigázosításához kiegészítő alapanyag választása termoanalitikai vizsgálatok alapján, *Anyagvizsgálók Lapja,* (2014), 33–40.
[9] *Heating value of gases from biomass gasification.* Report prepared for: IEA Bioenergy Agreement, Task 20 – Thermal Gasification of Biomass Lars Waldheim, Torbjörn Nilsson TPS Termiska Processer AB May 2001. Access date: 2015. 10. 19. http://www.ieatask33.org/app/webroot/files/file/publications/HeatingValue.pdf
[10] LACKNER, M.–PALOTÁS, Á. B.–WINTER, F.: *Combustion: From Basics to Applications*. Wiley–VCH Verlag GmbH & Co. KGaA, Wienheim, 2013.
[11] Engineeringtoolbox. Access date: 2015. 10. 19. http://www.engineeringtoolbox.com/
[12] BÍRÓ A.: *Tüzeléstan*. Miskolci Egyetem Sokszorosító Üzeme, Miskolc, 1997.

THE BRIEF STORY OF THE FACULTY ISSUE

The issue presents a segment of the scientific activity of the Faculty of Materials Science and Engineering. Covering nearly 71 years this issue is the direct continuation of the 'Issue series' belonged to the University of Miskolc and its predecessors in title.

The first edition titled 'Issues of the Mining and Metallurgy Department of the Hungarian Royal Mining and Forest Engineering College' came out in 1929.

The first 32 volumes published between 1929 and 1972 gave foreign language summaries of the research results from the mining, metallurgy and later also from the mechanical engineering field.

From 1957 the Issue Series were published in Hungarian language as well.

Up to 1975 **21** mining-metallurgy and mechanical engineering issues had come out **in Hungarian version**.

From 1975 the special fields have published their own issues separately. Our Faculty was given the **Series II METALLURGY** title within the main title 'Issue Series' (Issues 22–27).

After the long break, the new title of the Issues 28–32 (2000–2004) published in Hungarian language was:

MATERIALS AND METALLURGY SCIENCES,

then the Issues 33–40 (2007–2015) including booklets in English and Hungarian language were titled as

MATERIALS SCIENCE AND ENGINEERING

which refers to the name change of our faculty. The articles in present issue (41/1) represent the diversity of the research activities of the Faculty of Materials Science and Engineering and the strong relationships between the different scientific fields.

Secreteriat of the Vice-Rector for Research and International Relations,
University of Miskolc,
Responsible for the Publication: Prof. Dr. Tamás Kékesi
Published by the Miskolc University Press under leadership of Attila Szendi
Responsible for duplication: Works manager: Erzsébet Pásztor
Number of copies printed:
Put the Press in 2016
Number of permission: TNRT–2016–198–ME